

UNIVERSITY OF NAPLES FEDERICO II

DEPARTMENT OF ELECTRICAL ENGINEERING
AND INFORMATION TECHNOLOGY



PHD THESIS

IN

INFORMATION TECHNOLOGY AND ELECTRICAL ENGINEERING

**Induction-coil transducers for measuring
transversal field harmonics in
accelerator magnets**

Supervisor:

Prof. Pasquale Arpaia

Candidate:

Eng. Gianni Caiafa

2017 - 2018

©Gianni Caiafa

Dedico questa tesi a miei favolosi genitori, alla loro nobiltà d'animo e alla loro onestà.

This thesis is dedicated to my fabulous parents, to their nobleness and their honesty.

Sommario

Il presente lavoro di tesi riguarda lo sviluppo matematico, la validazione numerica, la progettazione e la caratterizzazione metrologica di un innovativo sensore per la misura di campo magnetico basato su bobina rotante.

In particolare, il modello matematico che lega le misure magnetiche al calcolo del campo magnetico nell'apertura di magneti per acceleratori è stato validato numericamente utilizzando dati ottenuti da simulazioni FEM.

Sulla base delle simulazioni numeriche è stato sviluppato il design dell'innovativo sensore basato su bobina rotante. In particolare, data l'esigenza di eseguire misure del profilo di campo magnetico su tutta la lunghezza del magnete, il sensore richiede l'assenza di sensibilità alla componente trasversale di campo. Per tale motivo la geometria del sensore prevede un determinato numero di spire che si richiudano percorrendo la periferia di un cilindro. Tale particolare geometria è stata battezzata "Iso-perimetrica".

A valle del design è stata definita la tecnologia costruttiva del sensore, il design del trasduttore e lo sviluppo di nuove metodologie per il calcolo dei coefficienti di sensibilità e per la calibrazione del sensore e del trasduttore.

Infine, sono riportati i risultati sperimentali utilizzando il primo prototipo realizzato, lo sviluppo del secondo prototipo e i risultati ottenuti per una particolare applicazione.

Resume

The following thesis deals with the mathematical development, the numerical validation, the design, and the metrological characterization of an innovative sensor for magnetic measurements based on rotating coils.

The developed mathematical model, linking experimental data and the field description in the aperture of magnets for accelerator, was numerically validated using simulated data. The validation results made it possible to check the correlation between measurements and the mathematical model itself.

Furthermore, the numerical validation allowed to satisfy the constraints for the design and manufacturing tolerances of the sensor.

The sensor that is required to perform local field distribution measurements along the magnet axis, must be not sensitive to the z -field component (namely to the field in the direction of beam travelling in the particle accelerator magnet). For this reason, the coil design is based on a certain number of loops placed on the same radius. This particular geometry has been called "Iso-perimetric".

The sensor production, the transducer design, an innovative methodology for the sensitivity coefficients calculations and for the calibration procedure were carried out.

Finally, the experimental results of the proof of principle of the first prototype, the design of the second prototype, and the measurements results are reported.

List of publications

Journal Papers:

- [1] P. Arpaia, G. Caiafa, S. Russenschuck, *A Rotating-Coil Magnetometer for Scanning Transversal Field Harmonics in Accelerator Magnets*, *Nature Scientific Reports*, 2018, DOI: 10.1038/s41598-018-37371-3.
- [2] P. Arpaia, G. Caiafa, S. Russenschuck, *A flexible printed-circuit board coil for scanning, transversal magnetic-fields errors in accelerator magnets*, submitted to *Sensors & Actuators: A. Physical*, 2018.
- [3] P. Arpaia, G. Caiafa, S. Russenschuck, *A transducer based on a rotating iso-perimetric induction coil sensor*, submitted to *Transactions on Instrumentation and Measurement*, 2018.

Conference Papers:

- [4] P. Arpaia, G. Caiafa, S. Russenschuck, *An induction rotating coil for longitudinal scanning of particle accelerator magnets*, *Journal of Physics Conference Series*, Vol. 1065, No. 17, 2018, doi:10.1088/1742-6596/1065/5/052047.
- [5] P. Arpaia, G. Caiafa, S. Russenschuck, *An Iso-Perimetric Rotating-Coil Magnetometer*, IEEE Sensors 2018, New Delhi, 2018.
- [6] S. Russenschuck, G. Caiafa, L. Fiscarelli, M. Liebsch, C. Petrone, P. Rogacki, *Challenges in extracting pseudo-multipoles from magnetic measurements*, ICAP' 18, Key West, Florida, USA.
- [7] G. Brando, A. Dannier, L. P. Di Noia and G. Caiafa, *Axial flux permanent machine design for low speed high torque application*, 2017 IEEE 6th ICRERA, San Diego, CA, 2017.

Acknowledgements

The thesis presented in the dissertation was carried out at CERN (Conseil Européen pour la Recherche Nucléaire), in collaboration with the Department of Electrical Engineering and Information Technology (DIETI) of the University of Naples Federico II and the Magnetic Measurements section of the Magnets Superconductor and Cryogenics (MSC) group at CERN, Technology Department (TE).

This thesis is the result of three years at CERN where I have been involved in this interesting and challenging project. Thanks to this experience, I had the possibility to grow and improve myself in both personal and professional matters.

First, I would like to thank my University Supervisor Prof. Pasquale Arpaia. Thanks to him I had the possibility to come at CERN. He encouraged me to go beyond my limits.

I want to thank my CERN Supervisor, Prof. Stephan Russenschuck, for his great determination, passion and deep knowledge of the field of magnetic measurements. Thanks to him, I improved a lot my technical and communication skills. He showed me how with love and passion for research is possible to obtain great results.

A grateful thanks to all the TE-MSC-MM section for the support in all the activities carried out during the last three years for my project.

A particular thanks to all the people that I have met at CERN. Every one of them has given something to me. Something that will be with me, as part of me, forever.

Special thanks to Alessandro Parrella for having shared with me the first trip to Geneva and many other experiences, to Eleni Tournaki for having been my support in many difficult moments, to Eszter Badinova for her sweetness, to Cristina León Vallina for having given to me, many times, the motivation to do not give up, to Piotr Tomasz Rogacki for the work suggestions and the pizza parties, to Domenico Caiazza, Annalisa Romano, Vanessa Di Murro and Francesca Ragucci for the amazing dinner, to all Casa Sauvigny for the joyful time spent together, to my flatmates Antonio Cesarano and Gabriele Piscopo for putting up with me, to Rocio Martinez Estebanez, Christian Grech, Maria Amodeo, Vincenzo Di Capua, Mariano Pentella for the constructive talks and for the time spent together.

Thanks to Ernesto De Matteis, Lucio Fiscarelli and Carlo Petrone for the technical advice and their exemplary professionalism.

Acknowledgements

The most important thank must go to my family (my parents, my brother, his wife, my niece and my lovely grandmother), they are without any doubts the sap that allowed me to complete this experience.

Thanks a lot for your support and especially for your LOVE.

Table of contents

Sommario	iii
Resume	v
List of publications	vii
Introduction	xv
I Background	1
1 Magnetic measurements for accelerator magnets	3
1.1 Harmonics analysis	3
1.2 Short magnets	8
1.3 Conclusions	10
2 Pseudo-multipoles	11
2.1 Pseudo-multipoles theory	11
2.2 Conclusions	21
II Proposal	23
3 Analysis of the pseudo-multipole expansion	25
3.1 Numerical model validation at the example of an air-coil magnet	26
3.2 Conclusions	32
4 The conceptual and engineering designs of the sensor	33
4.1 Conceptual design	33
4.2 Sensitivity factors and sensor length	40

Table of contents

4.3	Sensitivity factor calculation for PCB coils	43
4.4	Uncertainty analysis	45
4.5	Design of radial and tangential sensing coils	46
4.6	Conclusions	49
5	Conceptual and engineering design of the rotating-coil transducer	51
5.1	Rotating-coil transducer and bench design for the proof of principle	52
5.1.1	The rotating-coil transducer	52
5.1.2	The measurement station	53
5.2	Transducer and bench concept design; second prototype	55
5.2.1	The transducer	55
5.2.2	Deformation, stress and natural frequencies analysis	58
5.2.3	The measurement station	59
5.3	Conclusions	60
III	Sensor and transducer production and calibration	63
6	The sensor	65
6.1	PCB production	65
6.2	Mechanical metrological characterization	70
6.3	Functional tests and calibration	75
6.4	Conclusions	78
7	The transducer	79
7.1	Production	80
7.2	Calibration	84
7.2.1	Dipole calibration	84
7.2.2	Quadrupole calibration	85
7.3	Conclusions	89
IV	Experimental Results	91
8	Validation and field measurements	93
8.1	Transducer measurement validation in reference dipole	93
8.2	Measurements on a bending corrector dipole	97
8.2.1	Measurement data deconvolution	108

Table of contents

8.2.2	Reverse engineering solution	112
8.3	Magnetic measurements on a Canted-Cosine-Theta magnet	116
8.4	Medical applications	120
8.5	Conclusions	121
Conclusions		123
List of figures		127
List of tables		131
References		133
Appendix A Technical drawings		137

Introduction

For magnetic measurements of accelerator magnets, the induction-coil magnetometer is still the best transducer in terms of linearity, repeatability, reliability, and accuracy. Induction coils are applied to measure the field strength, direction, and field errors expressed as higher-order field harmonics [29, 31]. The magnetic measurements of accelerator magnets are usually performed with shafts, containing a number of induction coils, that are longer than the magnet length and therefore cover also the fringe field regions. In fact, measuring the integrated transversal field components is often sufficient to validate the design and characterize accelerator magnets, in particular for magnet-to-magnet reproducibility in larger series.

In other cases, the local field distribution measurements are required. This is the case for fringe-field dominated magnets and when the measurements are to be used for track reconstruction in mass spectrometers [32, 37]. Fringe field-dominated magnets are short magnets with relatively wide apertures, where the effect of the magnet ends is not negligible [39, 4]. The knowledge of the local field distribution in the magnets is also important for the study of the beam dynamics of insertion regions where the β -function changes rapidly [2].

The field distributions at the magnet extremities cannot be developed into Fourier series (that is the classical field harmonics), because the trigonometric functions do not constitute a complete orthogonal function set of the field solution [30]. This gives rise to Fourier-Bessel series and the so-called pseudo-multipoles [35, 36], which depend on the magnetic field variation along the magnet axis.

In literature, we could find many field measurement systems based on different technologies, like Hall sensors, Nuclear Magnetic Resonance (NMR), rotating-coil and wire technologies. Not all of them are suitable for acquiring the local field distribution [11]. NMR transducers are very accurate for the main field for example, Metrolab PT2025 NMR [PT2025], with ± 5 and ± 0.1 ppm of absolute and relative accuracy, respectively. However, they are not suitable for gradient measurements (for example fringe fields), and have limited lower range of operation (for example Metrolab PT2025 probe, 0.043 T). One possibility is to measure the longitudinal profile by mapping the magnet bore with a 3D Hall sensor, [34, 13], mounted

Introduction

on a displacement stage. Hall probes, in fact, are widely used for local mapping of straight and curved magnets [38, 17, 19]. Main advantages are high spatial resolution due to the size of the sensing element and a wide range of field. Main disadvantages are the relatively low accuracy (0.1%) due to their nonlinear characteristic, the temperature dependence of the metrological performance and secondary effects like the planar effect. Moreover, the mechanical limit of these systems, and accordingly the measurement precision, is the difficulty to align the Hall probe with respect to the mechanical system. Another solution is to use a translating-coil scanner on the magnet mid-plane [5]. In the latter case, however, the transversal resolution (and the highest order of the field harmonics) is limited by the track widths of the single coils. An innovative way to measure the local field distribution was presented in [12], where a rotating coil transducer [3] and a train-like system for longitudinal motion and positioning inside the magnet bore, based on rotating coils, was developed. This innovative transducer was developed with (i) small-size sensing coil elements, for example for space charge computations, (ii) accurate transport, for longitudinal displacements inside the magnet gap, and (iii) adequate magnetic compatibility, for negligible interference with the measurand field. In [30], it was proven that the classical rotating-coil magnetometers, [12], cannot be used in regions where a significant axial field component is present. In fact, the extraction of pseudo-multipoles from transversal field measurements on a reference radius requires a coil that intercepts only the radial field component and thus is free of the voltage induced by the axial field component. The main objective for the coil design is to achieve the same resolution and measurement uncertainty of the standard rotating coils with a signal-to-noise ratio of about 60 dB [21].

In this Thesis, a new concept of a short, rotating-coil magnetometer that does not intercept the axial field component is proposed. The coil is designed as a four-layer, flexible printed circuit, with 40 μm thick tracks and 50 μm electrical insulation between them. The magnetic field mapper is based on the rotating coil method, for localized measurements of magnetic fields and the harmonic multipole content in the magnet ends. The system is composed of a rotating coil transducer and a 3D mapper system for the positioning inside magnet bore.

In the *Background* part, the **Chapters 1 and 2** present the theory of the magnetic measurements for accelerator magnets focusing on the harmonic analysis, the pseudo-multipole theory, and the mathematical model for field reconstruction from measurements.

In the *Proposal* part, **Chapter 3** presents the numerical validation and uncertainty estimation of the mathematical model. The **Chapter 4** focuses on the conceptual sensor design

and on the engineering design, highlighting the main challenges in the project. In **Chapter 5**, the architecture and design of the entire transducer is presented.

In the *Production and Calibration* part, **Chapter 6** illustrates the sensor production and calibration. In **Chapter 7**, the transducer production and calibration is presented for both, the first and second prototype.

Finally, in the part on *Experimental Results*, **Chapter 8** shows and discusses the measurements on the complete bench, focusing on the end-field profile measurements and on the practical application of the developed mathematical model.

Part I

Background

Chapter 1

Magnetic measurements for accelerator magnets

Magnets for particle accelerators require magnetic field measurements in many stages of the project. Measurements are performed on the materials for magnetic permeability characterization, during the prototyping phase to validate the design and to adjust the production process, and for the production to monitor and to guarantee the reproducibility. Usually, measurements are required for beam dynamics studies and to optimize the machine operation cycles. Other measurements can be requested to evaluate secondary effects like eddy currents or hysteresis effects that are particularly difficult to compute with FEM/BEM models. However, in accelerator magnets, if the beam has a large acceptance, the beta function changes rapidly, or, if the measurements shall be used for track reconstruction [33], the local field distribution has to be known with high precision, [26]. Further complication arises from test engineering constraints of last-generation compact accelerators (curvature radii less than 5 m) for biomedical applications and physics research. A well consolidate method for magnetic field measurement in particle accelerators is the rotating search coil method [11].

The first part of the chapter presents the theoretical fundamentals of the rotating coil method, the computation of the coil sensitivity factors and the definition of short magnets.

1.1 Harmonics analysis

In magnet for accelerator, the field description (that is, the field quality) is described by a set of Fourier coefficients. In [29] the description of the method and the measurement of the so-called field harmonics or multipole is described. The classical method used for the calculation of field harmonics is based on finding a general solution that satisfies the

Magnetic measurements for accelerator magnets

Laplace equation in cylindrical coordinates. In the aperture of accelerator magnets, free of currents and magnetized material, both scalar and vector potentials can be employed for the formulation of a boundary value problem. The integration constants in the general solution, obtained with the separation of variables technique, are then determined by comparison with the boundary values. The classical method compares the integration constants with the Fourier series expansion of the field components on the domain boundary. In accelerator magnets, the domain boundary is often chosen as a circle with a radius of two-thirds of the aperture radius. A general solution that satisfies the Laplace equation, $\nabla^2 A_z = 0$, can be found by the separation of the variables method. Considering that the potential must remain finite at the axis, the eigensolutions of the Laplace equation can be written as:

$$A_z(r, \varphi) = \sum_{n=1}^{\infty} r^n (A_n \sin n\varphi + B_n \cos n\varphi) . \quad (1.1)$$

For the eigensolutions we can calculate the field components (radial and azimuthal)

$$B_r(r, \varphi) = \frac{1}{r} \frac{\delta A_z}{\delta \varphi} = \sum_{n=1}^{\infty} nr^{n-1} (A_n \cos n\varphi - B_n \sin n\varphi) , \quad (1.2)$$

$$B_\varphi(r, \varphi) = -\frac{\delta A_z}{\delta r} = -\sum_{n=1}^{\infty} nr^{n-1} (A_n \sin n\varphi + B_n \cos n\varphi) . \quad (1.3)$$

Each value of the integer n in the solution of the Laplace equation corresponds to a specific flux distribution generated by ideal magnet geometries. The three lowest values, $n = 1, 2, 3$, correspond to the dipole, quadrupole, and sextupole flux density distributions. The A_n and B_n , called multipole coefficients, or field harmonics, are the coefficients that must be determined by solving a boundary value problem. Assuming that the radial component of the magnetic flux density is measured or calculated at a reference radius $r = r_0$ as a function of the angular position φ , the Fourier series expansion of the field components (radial B_r and azimuthal B_φ) will be

$$B_r(r_0, \varphi) = \sum_{n=1}^{\infty} (B_n(r_0) \sin n\varphi + A_n(r_0) \cos n\varphi) , \quad (1.4)$$

$$B_\varphi(r_0, \varphi) = \sum_{n=1}^{\infty} (B_n(r_0) \cos n\varphi - A_n(r_0) \sin n\varphi) , \quad (1.5)$$

where

$$A_n(r_0) = \frac{1}{\pi} \int_0^{2\pi} B_r(r_0, \varphi) \cos n\varphi d\varphi \quad n = 1, 2, 3, \dots , \quad (1.6)$$

$$B_n(r_0) = \frac{1}{\pi} \int_0^{2\pi} B_r(r_0, \varphi) \sin n\varphi d\varphi \quad n = 1, 2, 3, \dots, \quad (1.7)$$

Because the magnetic flux density is divergence free, $A_0 = 0$. In computational practice, the B_r field components are numerically calculated at N discrete points in the interval $[0, 2\pi]$

$$\varphi_k = \frac{2\pi k}{N}, \quad k = 0, 1, 2, \dots, N-1. \quad (1.8)$$

This allows the calculation of two times N Fourier coefficients by the discrete Fourier transform (DFT)

$$A_n(r_0) \approx \frac{2}{N} \sum_{k=0}^{N-1} B_r(r_0, \varphi_k) \cos n\varphi_k, \quad (1.9)$$

$$B_n(r_0) \approx \frac{2}{N} \sum_{k=0}^{N-1} B_r(r_0, \varphi_k) \sin n\varphi_k. \quad (1.10)$$

These coefficients are usually noted in units (10^{-4}) of tesla at a given reference radius r_0 . Normally the reference radius, that sometimes corresponds at the measurement radius, is $2/3$ of the magnet aperture. The normal and skew multipoles $b_n(r_0)$ and $a_n(r_0)$ are related to the main field $B_N(r_0)$ (B_1 for the dipole, B_2 for the quadrupole, and so on). The equations (1.4) and (1.5) become

$$B_r(r_0, \varphi) = B_N \sum_{n=1}^{\infty} (b_n(r_0) \sin n\varphi + a_n(r_0) \cos n\varphi), \quad (1.11)$$

$$B_\varphi(r_0, \varphi) = B_N \sum_{n=1}^{\infty} (b_n(r_0) \cos n\varphi - a_n(r_0) \sin n\varphi). \quad (1.12)$$

If is needed to scale the multipole coefficients to any radius r inside the aperture we should apply the following laws

$$A_n(r) = \left(\frac{r}{r_0}\right)^{n-1} A_n(r_0), \quad (1.13)$$

$$B_n(r) = \left(\frac{r}{r_0}\right)^{n-1} B_n(r_0). \quad (1.14)$$

Hence

$$b_n(r) = \frac{B_n(r)}{B_N(r)} = \frac{\left(\frac{r}{r_0}\right)^{n-1} B_n(r_0)}{\left(\frac{r}{r_0}\right)^{N-1} B_N(r_0)} = \left(\frac{r}{r_0}\right)^{n-N} b_n(r_0). \quad (1.15)$$

Magnetic measurements for accelerator magnets

The magnetic field usually is represented in the 2D complex plane (x, y) in terms of the complex variable $z = x + iy$. If the trigonometric transformation $(\cos \varphi + i \sin \varphi)^n = (e^{i\varphi})^n = e^{in\varphi} = \cos n\varphi + i \sin n\varphi$ is applied to Eqs. (1.4) and (1.5) the magnetic field can be represented in cartesian coordinates as

$$B_x(r, \varphi) = \sum_{n=1}^{\infty} (B_n(r_0) \sin(n-1)\varphi + A_n(r_0) \cos(n-1)\varphi), \quad (1.16)$$

$$B_y(r, \varphi) = \sum_{n=1}^{\infty} (B_n(r_0) \cos(n-1)\varphi - A_n(r_0) \sin(n-1)\varphi). \quad (1.17)$$

In literature the multipole coefficients are represented in complex notation as

$$C_n(r_0) = B_n(r_0) + iA_n(r_0). \quad (1.18)$$

In the complex plane (x, y) the field representation becomes

$$B(z) = B_y(z) + iB_x(z) = \sum_{i=0}^{\infty} C_n(z) \left(\frac{z}{r_0} \right)^{(n-1)}. \quad (1.19)$$

As mentioned, the harmonic coefficients are indicated relatively to main field component B_N

$$c_n = 10^4 \frac{C_n}{B_N} = 10^4 \left(\frac{B_n}{B_N} + i \frac{A_n}{B_N} \right) = b_n + ia_n, \quad (1.20)$$

where the normalized c_n are expressed in the form of units.

In order to correlate the measured flux to the multipole coefficient is required to introduce the coil-sensitivity factors. The method of the harmonic coil is based on the Faraday-Lens's law Eq. 1.21.

$$U = -\frac{d\Phi}{dt}, \quad (1.21)$$

which indicates as the change of the magnetic flux in the time generates an induced voltage with opposite sign. The magnetic flux can be evaluated integrating the Eq. 1.21 in time

$$\Phi(t) = -\int_{t_1}^{t_2} U dt. \quad (1.22)$$

If the field is assumed to be uniform in the z -direction and constant in the time, the flux can be written in terms of coil area A , function of the coil turns N ,

$$\Phi = N \int_A \mathbf{B} \cdot d\mathbf{a}, \quad (1.23)$$

where Φ is evaluated in $\text{Vs} = \text{Tm}^2 = \text{Wb}$. The coil is perfectly centered in the magnet and rotates rigidly with an angular velocity ω around the magnet axis, (red in Fig. 1.1). Assuming the coil wire infinitely thin, the surface for all the coil turns N around the axis is

$$A = Nl \int_{r_1}^{r_2} dr = Nl(r_2 - r_1), \quad (1.24)$$

where l is the length of the coil.

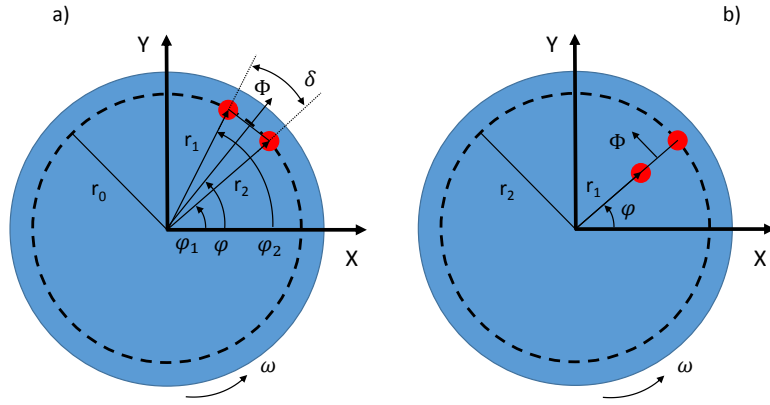


Fig. 1.1 Rotating coil: (a) tangential and (b) radial coil scheme.

The flux linkage through the coil at position φ can be calculated from

$$\Phi(\varphi) = N \int_A \mathbf{B} \cdot d\mathbf{a} = N \int_A \text{curl} \mathbf{A} \cdot d\mathbf{a} = N \int_{\delta A} \mathbf{A} \cdot d\mathbf{r} = Nl [A_z(P_1) - A_z(P_2)], \quad (1.25)$$

where N is the number of turns and l the magnetic length of the induction coil.

Writing the vector potential at points $P_1 = (r_1, \varphi_1)$ and $P_2 = (r_2, \varphi_2)$ by means of the series yields

$$\begin{aligned} \Phi(\varphi) = Nl & \left[\sum_{n=1}^{\infty} \frac{r_0}{n} \left(\frac{r_2}{r_0} \right)^n (B_n(r_0) \cos n\varphi_2 - A_n(r_0) \sin n\varphi_2) + \right. \\ & \left. - \sum_{n=1}^{\infty} \frac{r_0}{n} \left(\frac{r_1}{r_0} \right)^n (B_n(r_0) \cos n\varphi_1 - A_n(r_0) \sin n\varphi_1) \right], \end{aligned} \quad (1.26)$$

which can be rewritten as

$$\Phi(\varphi) = \sum_{n=1}^{\infty} \frac{1}{r_0^{n-1}} [K_n^{rad}(B_n(r_0) \cos n\varphi - A_n(r_0) \sin n\varphi) + K_n^{tan}(B_n(r_0) \cos n\varphi - A_n(r_0) \sin n\varphi)], \quad (1.27)$$

where the K_n^{rad} and K_n^{tan} are the coil-sensitivity factors and are give by:

$$K_n^{rad} = \frac{Nl}{n} [r_2^n \cos n(\varphi_2 - \varphi) - r_1^n \cos n(\varphi_1 - \varphi)], \quad (1.28)$$

$$K_n^{tan} = \frac{Nl}{n} [r_2^n \sin n(\varphi_2 - \varphi) - r_1^n \sin n(\varphi_1 - \varphi)], \quad (1.29)$$

or:

$$K_n = K_n^{rad} + iK_n^{tan} = \frac{Nl}{n} (r_2^n e^{in(\varphi_2 - \varphi)} - r_1^n e^{in(\varphi_1 - \varphi)}), \quad (1.30)$$

For example, considering the tangential coil scheme in Fig. 1.1a, the magnetic flux at time t is

$$\begin{aligned} \Phi(t) &= Nl \int_A B_r(r_0, A) r_0 dA \\ &= \sum_{n=1}^{\infty} K_n^{tan} [B_n(r_0) \sin(n\omega t + n\varphi) + A_n(r_0) \cos(n\omega t + n\varphi)] \end{aligned} \quad (1.31)$$

where φ is the angle of the coil at time $t = 0$ and

$$K_n^{tan} = \frac{2Nlr_0}{n} \sin\left(\frac{n\delta}{2}\right) \quad (1.32)$$

is the coil sensitivity of tangential coil, that depends on the geometrical features of the coil, δ is the opening angle, and r_0 the measurement coil radius. The coil sensitivity factors are evaluated by the calibration procedure, and the field harmonics are obtained by Fourier transform of the flux (1.31).

1.2 Short magnets

Short magnets are fringe-field dominated magnets with relatively wide apertures, where the effect of the magnet ends is not negligible [39], [4]. In case of short magnets, the

measurements of the local field distribution are required. This is also important for the study of the beam dynamics of insertion regions where the β -function changes rapidly [2].

Nowadays, more and more precision is required in beam dynamic simulations and compact solutions are desired for the construction of particle accelerators, especially in medical applications. For example, for biomedical projects with compact dimensions linear or curved magnet, a full characterization of the local and transversal field homogeneity and quality is required. Furthermore, intrinsic non-linearity of the magnetic field can cause nonlinear motion of the beam particles, thus limit the betatron tunability. Reason for why, not only the integrated magnetic flux density is required, but even the local measurements, such as field distribution and fringe fields. All of them help to predict space charge effects on the beam lifetime.

For example, knowing the value of the field on the fringe field area can be used to decide where to locate, or how to combine in a more efficient way, individual magnets. This procedure can reduce dispersion of bending strength or high order imperfection on the beam dynamic, thus increasing the quality of the accelerator system.

The z-field component, present on the fringe field regions, decreases the precision of the measurement as well as vibrations or any other source of uncertainty that may affect the measurement results. For this reasons, the design of the new transducer was performed in order to obtain a search coil device able to measure the longitudinal field profile reducing the errors by means increasing the signal to noise ratio. In the frame of the validation design of the new magnets for Hi-Lumi project [24], the prototype was designed and tested.

There are other techniques to measure local magnetic flux densities, but all of them are not enough precise and accurate or cannot be applied for our purpose. Hall probes, for example, have several factors that set limits on their accuracy. First of all the temperature coefficient of the Hall voltage. The temperature coefficient depends on the level of the magnetic field and it is important during the calibration to monitor the temperature and to perform calibrations at different field levels. Another important aspect to take in consideration during the calibration is the planar Hall effect, it could limit the application of Hall probes in fringe field area where the magnetic field is strongly distorted.

The magnetic resonance techniques is used for precision field mapping and could be the best candidate for our purpose having really high accuracy, linearity and static operation. The limit is that it needs a rather homogeneous field in order to obtain a sufficiently coherent signal. This is, again, not the case of the fringe field areas. Fluxgate magnetometers, that are based on a ferromagnetic core with a detection and excitation coils wounded around, could be a potential candidate having high sensitivity and a linear characteristic, but are restricted to use with low fields, range of 1 mT. Some others technique as magnet-resistivity

Magnetic measurements for accelerator magnets

effect, visual field mapping, magneto-resistors, magneto-inductance and superconducting quantum interference device were not taken into consideration for the requirements of our measurements.

1.3 Conclusions

In this first chapter, the harmonics analysis and the definition of short magnets were discussed. In particular, the well-consolidated method for magnetic field measurements in particle accelerator was described, the computation of the sensitivity factor was reported, and the definition of short magnet was given.

Chapter 2

Pseudo-multipoles

For accelerator magnets such as capture solenoids, fragment separator dipoles, and insertion quadrupoles, it is important to measure not only the integrated field errors, but also the local field distributions in the magnet extremities. In three-dimensional field problems, the transversal multipole coefficients do not constitute a complete orthogonal function set. This gives rise to pseudo-multipoles in Fourier-Bessel series. Measuring the transversal field harmonics with a short rotating induction-coil magnetometer is a way to extract the coefficients of a Fourier-Bessel series (pseudo-multipoles), which can be used to compute the full field map of accelerator magnets. Research efforts were required to develop a mathematical model that links magnetic measurements with pseudo-multipoles and to design a short sensor that is insensitive to the longitudinal field components, but sensitive to high-order harmonics with a resolution of 100 ppm.

The scaling laws derived from the integrated (two-dimensional) field harmonics in accelerator magnets, cannot be used in the 3D case because these field harmonics do not constitute a complete, orthogonal function set. Applying the concept of pseudo-multipoles, the field distribution in the end-regions of the magnet can be reconstituted from measurements on the boundary surface, that is, the transversal multipole field errors over a short, isoperimetric coil.

In this chapter is presented the pseudo-multipole theory and the mathematical background.

2.1 Pseudo-multipoles theory

Magnets with large aperture and short length greatly affect the ion-optical calculation. Especially for a high magnetic field, when the iron yoke starts to be saturated, the effective length and the shapes of the field distribution change considerably with the excitation current. Bending magnets and quadrupoles are the most important devices used in beam transport

system and spectrometers. There are two codes that are applied to design and analyze ion-optical system. The transfer matrix, connecting phase space variables at the initial and final states order by order, is the first method based on Taylor expansion [6]. The second method is the ray-trace type, it solves an equation of motion and tracks the path of individual particles using a three-dimensional field distribution measured in advance [8]. Every kind of spectrometer, even with a complicated magnetic field distribution, can be simulated by this methodology and the orbit can be easily calculated. Furthermore, if it is required to have a precise setting of large aperture magnet, short length and high field where ion-optical calculation is necessary. In short magnets, large aperture, the pseudo components originate from the changes of the magnetic field along the beam axis must be taken into consideration. This is what it happens in the STQs [34]. To obtain the full 3D magnetic field map, many theorems are presented for example in [34, 25, 23], but an innovative way is presented in [30].

The magnetic field could be decomposed in multipoles only inside the magnet's bore (sufficiently far from the extremities). This base, could not be used anymore at the extremities due to the fact that the field distribution is highly non-linear and the multipoles are not anymore a complete orthogonal function set for the field decomposition.

The accelerator magnets aperture is characterized by being free of currents and magnetized material and for this reason, the magnetic scalar and vector potentials can be used for the application of a boundary value problem. Both of them, in two dimensions, yield a scalar Laplace equation for the magnetic scalar potential and for the z -component of the vector potential. The field quality in accelerator magnet is described by the Fourier coefficient of the harmonic analysis. A method to calculate the field harmonics is to find general solutions of the Laplace equation in proper coordinate system. In case of accelerator magnets, is chosen a cylindrical coordinate system. As first approximation, it is possible to consider the case of 2D circular coordinates because this is the most common way used to compute and measure, in accordance with the rotating coil method, the field in long magnet.

Considering a domain Ω (i.e. the bore of the magnet) and a scalar field ϕ_m , the Laplace equation $\nabla^2 A_z = 0$ can be solved applying the separation of variables method. If we consider that the vector potential must be a periodic function of ϕ , it can be single-valuated. The general solution in the defined domain were the condition of flux density finite at $r = 0$, can be written as

$$A_z(r, \varphi) = \sum_{n=1}^{\infty} (r^n (A_n \sin n\varphi + B_n \cos n\varphi)) . \quad (2.1)$$

The order n corresponds to a specific magnetic distribution generated by the magnet and the coefficient A_n, B_n are determined by the measured magnetic flux density on the domain

2.1 Pseudo-multipoles theory

boundary. Considering the cylindrical reference system, the radial component of the magnetic flux density is given by

$$B_r(r, \varphi) = \frac{1}{r} \frac{\delta A_z}{\delta \varphi} = \sum_{n=1}^{\infty} n r^{n-1} (A_n \cos n\varphi + B_n \sin n\varphi) , \quad (2.2)$$

in Ω . Considering a measurement at the radius r_0 , we can write, as function of φ , the Fourier series

$$B_r(r_0, \varphi) = \sum_{n=1}^{\infty} (B_n(r_0) \sin n\varphi - A_n(r_0) \cos n\varphi) . \quad (2.3)$$

Comparing now the two coefficients in the two expression of B_r we can write

$$B_r(r, \varphi) = \sum_{n=1}^{\infty} \left(\frac{r}{r_0} \right)^{n-1} (B_n(r_0) \sin n\varphi - A_n(r_0) \cos n\varphi) . \quad (2.4)$$

Usually the normal and skew component $B_n(r_0)$ and $A_n(r_0)$ are given in units of tesla at the reference radius r_0 .

In the case of short magnets, where short means magnets where the fringe field areas are not negligible in comparison with the magnet length, the 2D approximation is not valid anymore. This is the reason why it is needed to study the Laplace equation for the magnetic scalar potential in three-dimensional cylindrical coordinates. If we start from the Maxwell's equation $\nabla \cdot \mathbf{B} = 0$. Using the vector identity

$$\nabla \cdot (\nabla \times \mathbf{F}) = 0 , \quad (2.5)$$

for trivial domains, we have

$$\nabla \cdot \mathbf{B} = \nabla \cdot (\nabla \times \mathbf{A}) = 0 , \quad (2.6)$$

\mathbf{B} could be expressed as

$$\mathbf{B} = \nabla \times \mathbf{A} , \quad (2.7)$$

where \mathbf{A} is called vector potential. If we study a non-pulsed magnet (with stationary winding current) inside the gap (absence of any kind of currents or magnetic material), the right hand side terms in eq. $\nabla \times \mathbf{H} = \mathbf{J} + \frac{\partial}{\partial t} \mathbf{D}$ becomes zero and we obtain

$$\nabla \times \mathbf{H} = 0 , \quad (2.8)$$

using the identity

$$\nabla \times (\nabla f) = 0 , \quad (2.9)$$

Pseudo-multipoles

is it possible to express the magnetic flux density \mathbf{B} as

$$\mathbf{H} = \nabla \phi_m , \quad (2.10)$$

where $\nabla \phi_m$ is the scalar potential. Using 2.10 in $\nabla \cdot \mathbf{B} = 0$ and remembering that $\mathbf{B} = \mu_0 \mathbf{H}$ we obtain

$$\mu_0 (\nabla \cdot \nabla \phi_m) = 0 , \quad (2.11)$$

$$\nabla \cdot \nabla \phi_m = \nabla^2 \phi_m = 0 . \quad (2.12)$$

The eq. 2.12 is the well known Laplace equation for the scalar potential. In cylindrical coordinates, the Laplace equation for the 3D scalar potential becomes

$$\nabla^2 \phi_m = \frac{1}{r} \frac{\partial}{\partial r} \left(r \frac{\partial \phi_m}{\partial r} \right) + \frac{1}{r^2} \frac{\partial^2 \phi_m}{\partial \varphi^2} + \frac{\partial^2 \phi_m}{\partial z^2} = 0 . \quad (2.13)$$

Using the variable separation method, we find a solution for the previous differential equation that could be expressed as

$$\phi_m(r, \varphi, z) = R(r) \phi(\varphi) Z(z) , \quad (2.14)$$

then substituting in eq. 2.14 we obtain

$$\frac{1}{R} \frac{d^2 R}{dr^2} + \frac{1}{Rr} \frac{dR}{dr} + \frac{1}{\phi r^2} \frac{d^2 \phi}{d\varphi^2} + \frac{1}{Z} \frac{d^2 Z}{dz^2} = 0 , \quad (2.15)$$

$$\frac{1}{R} \frac{d^2 R}{dr^2} + \frac{1}{Rr} \frac{dR}{dr} + \frac{1}{\phi r^2} \frac{d^2 \phi}{d\varphi^2} = -\frac{1}{Z} \frac{d^2 Z}{dz^2} . \quad (2.16)$$

Using the separation constant p , the right hand site and the left hand site must be equal to p^2 , then we can write the following system of differential equations

$$\begin{cases} \frac{1}{R} \frac{d^2 R}{dr^2} + \frac{1}{Rr} \frac{dR}{dr} + \frac{1}{\phi r^2} \frac{d^2 \phi}{d\varphi^2} = p^2 \\ -\frac{1}{Z} \frac{d^2 Z}{dz^2} = p^2 . \end{cases} \quad (2.17)$$

Solving now the two equation separately we have for the (2.17.b)

$$\frac{1}{Z} \frac{d^2 Z}{dz^2} + p^2 = 0 \quad (2.18)$$

$$\frac{d^2 Z}{dz^2} + Zp^2 = 0, \quad (2.19)$$

which is a second order ordinary differential equation with constant coefficients. A possible solution for this equation could be expressed as,

$$Z(z) = Ae^{ipz}, \quad (2.20)$$

where A is a (complex) coefficient that depends of the boundary conditions (Dirichlet BC or Neumann BC depending on the problem) and i is the imaginary unit. Using Euler's formula, (2.20) could be also written as

$$Z(z) = A \cos(pz) + B \sin(pz), \quad (2.21)$$

or using the notation $\{ \}$ to indicate a linear combination of the terms inside the parenthesis we have

$$Z(z) = \left\{ \begin{array}{l} \cos(pz) \\ \sin(pz) \end{array} \right\}. \quad (2.22)$$

Let us solve eq. 2.17.a.

We start from

$$\frac{1}{R} \frac{d^2 R}{dr^2} + \frac{1}{Rr} \frac{dR}{dr} + \frac{1}{\phi r^2} \frac{d^2 \phi}{d\phi^2} = p^2, \quad (2.23)$$

that could be rearranged as

$$\frac{r^2}{R} \frac{d^2 R}{dr^2} + \frac{r}{R} \frac{dR}{dr} - p^2 r^2 = -\frac{1}{\phi} \frac{d^2 \phi}{d\phi^2}. \quad (2.24)$$

The two side of the equation must equals the same constant (n^2). A new differential equation system could be written as

$$\left\{ \begin{array}{l} \frac{r^2}{R} \frac{d^2 R}{dr^2} + \frac{r}{R} \frac{dR}{dr} - p^2 r^2 = n^2 \\ -\frac{1}{\phi} \frac{d^2 \phi}{d\phi^2} = n^2. \end{array} \right. \quad (2.25)$$

Pseudo-multipoles

It is clear that (2.25.b) can be solved exactly as (2.18).

$$\frac{1}{\phi r^2} \frac{d^2 \phi}{d\varphi^2} + n^2 = 0, \quad (2.26)$$

$$\frac{d^2 \phi}{d\varphi^2} + n^2 \phi = 0, \quad (2.27)$$

where a possible solution can be expressed in the same form of (2.22)

$$\phi(\varphi) = \begin{Bmatrix} \cos(n\varphi) \\ \sin(n\varphi) \end{Bmatrix}. \quad (2.28)$$

The solution for (2.25.a) is less straightforward. First of all let's do the change of variables

$$\xi = pr, \quad (2.29)$$

substituting (2.29) in (2.25.a) we obtain

$$\frac{d^2 R}{d\xi^2} + \frac{1}{\xi} \frac{dR}{d\xi} - \left[1 + \left(\frac{n}{\xi} \right)^2 \right] R = 0. \quad (2.30)$$

That leads to the modified Bessel function of the second kind where the generic solution is expressed as [1] and where the terms r^{-n} must be excluded.

The solution of the (2.30) is given by

$$R(r) = C_1 I_n(pr) + C_2 K_n(pr), \quad (2.31)$$

where C_1 and C_2 are arbitrary constant, $I_n(pr)$ and $K_n(pr)$ are the Bessel modified function of first and second degree, respectively.

$$I_n(pr) = \sum_{k=0}^{\infty} \frac{(pr/2)^{2k+n}}{k! \Gamma(n+k+1)}, \quad (2.32)$$

$$K_n(pr) = \frac{\pi I_{-n}(pr) - I_n(pr)}{2 \sin(\pi n)}, \quad (2.33)$$

using again the notation $\{\}$, we can write

$$R(pr) = \begin{Bmatrix} I_n(pr) \\ K_n(pr) \end{Bmatrix}. \quad (2.34)$$

The generic Laplace equation solution for magneto-static is then

$$\phi_m(r, \varphi, z) = R(r) \Phi(\varphi) Z(z) = \begin{Bmatrix} I_n(pr) \\ K_n(pr) \end{Bmatrix} \begin{Bmatrix} \cos(n\varphi) \\ \sin(n\varphi) \end{Bmatrix} \begin{Bmatrix} \cos(pz) \\ \sin(pz) \end{Bmatrix}. \quad (2.35)$$

At $r = 0$ the field cannot be infinite, for this reason we must exclude all the terms in r^{-n} . This implies that $K_n(pr)$ in (2.35) should be erased. Now we can write

$$\phi_m(r, \varphi, z) = I_n(pr) \begin{Bmatrix} \cos(n\varphi) \\ \sin(n\varphi) \end{Bmatrix} \begin{Bmatrix} \cos(pz) \\ \sin(pz) \end{Bmatrix}. \quad (2.36)$$

A possible solution for the scalar potential can be expressed as

$$\begin{aligned} \phi_m(r, \varphi, z) = \sum_{n=1}^{\infty} \sum_{p=1}^{\infty} I_n(pr) & \left[\left(\varepsilon_{p,n} \cos(pz) + f_{p,n} \sin(pz) \right) \cos(n\varphi) + \right. \\ & \left. + \left(G_{p,n} \cos(pz) + H_{p,n} \sin(pz) \sin(n\varphi) \right) \right]. \end{aligned} \quad (2.37)$$

Using the Modified Bessel equation (2.32) and following [15, 9], we have

$$\phi_m(r, \varphi, z) = \sum_{k=0}^{\infty} \sum_{n=1}^{\infty} r^{n+2k} (C_{n+2k,n}(z) \sin(n\phi) + D_{n+2k,n}(z) \cos(n\phi)). \quad (2.38)$$

We can see that for $k = 0$ the (2.38) is the classical decomposition in multipoles. Substituting (2.38) in the Laplace equation (2.13) we have

$$\begin{aligned} \nabla^2 \phi_m = \frac{1}{r} \frac{\partial}{\partial r} & \left[\sum_{k=0}^{\infty} \sum_{n=1}^{\infty} (n+2k) r^{n+2k} (C_{n+2k,n}(z) \sin(n\phi) + D_{n+2k,n}(z) \cos(n\phi)) \right] \\ & - \frac{1}{r^2} \left[\sum_{k=0}^{\infty} \sum_{n=1}^{\infty} n^2 r^{n+2k} (C_{n+2k,n}(z) \sin(n\phi) + D_{n+2k,n}(z) \cos(n\phi)) \right] \\ & + \sum_{k=1}^{\infty} \sum_{n=1}^{\infty} r^{n+2k} (C_{n+2k,n}^{(2)}(z) \sin(n\phi) + D_{n+2k,n}^{(2)}(z) \cos(n\phi)) \\ = & \left[\sum_{k=0}^{\infty} \sum_{n=1}^{\infty} (n+2k)^2 r^{n+2k-2} (C_{n+2k,n}(z) \sin(n\phi) + D_{n+2k,n}(z) \cos(n\phi)) \right] \\ & - \left[\sum_{k=0}^{\infty} \sum_{n=1}^{\infty} n^2 r^{n+2k-2} r^{n+2k} (C_{n+2k,n}(z) \sin(n\phi) + D_{n+2k,n}(z) \cos(n\phi)) \right] \\ & + \sum_{k=1}^{\infty} \sum_{n=1}^{\infty} r^{n+2k} (C_{n+2k,n}^{(2)}(z) \sin(n\phi) + D_{n+2k,n}^{(2)}(z) \cos(n\phi)) = 0, \end{aligned} \quad (2.39)$$

Pseudo-multipoles

where $C_{n+2k-2,n}^{(m)}(z) = \frac{\partial^m C_{n+2k-2,n}(z)}{\partial z^m}$. If we define the coefficients $C_{n+2k,n}^{(2)}(z)$ and $D_{n+2k,n}^{(2)}(z)$ as zero for $k=0$, the (2.39) can be written as follow

$$\begin{aligned} \nabla^2 \phi_m = & \sum_{k=0}^{\infty} \sum_{n=1}^{\infty} \left[C_{n+2k,n}(z) ((n+2k)^2 - n^2) + C_{n+2k-2,n}^{(2)}(z) \right] r^{n+2k-2} \sin(n\varphi) \\ & + \sum_{k=0}^{\infty} \sum_{n=1}^{\infty} \left[D_{n+2k,n}(z) ((n+2k)^2 - n^2) + D_{n+2k-2,n}^{(2)}(z) \right] r^{n+2k-2} \cos(n\varphi) = 0. \end{aligned} \quad (2.40)$$

Due to the fact that the previous equation must hold for any r and φ , and that the trigonometric functions are orthogonal, the coefficients must obey

$$\begin{aligned} C_{n+2k,n}(z) ((n+2k)^2 - n^2) + C_{n+2k-2,n}^{(2)}(z) &= 0 \\ D_{n+2k,n}(z) ((n+2k)^2 - n^2) + D_{n+2k-2,n}^{(2)}(z) &= 0. \end{aligned} \quad (2.41)$$

Fixing n and varying k from one to three we have

$$\begin{aligned} C_{n+2,n}(z) &= \frac{C_{n,n}^{(2)}(z)}{(n^2 - (n+2)^2)}, \\ C_{n+4,n}(z) &= \frac{C_{n,n}^{(4)}(z)}{(n^2 - (n+4)^2)(n^2 - (n+2)^2)}, \\ C_{n+6,n}(z) &= \frac{C_{n,n}^{(6)}(z)}{(n^2 - (n+6)^2)(n^2 - (n+4)^2)(n^2 - (n+2)^2)}. \end{aligned} \quad (2.42)$$

Therefore, we can write for any coefficients the following recursion

$$C_{n+2k,n}(z) = \frac{C_{n,n}^{(2k)}(z)}{\prod_{m=1}^k (n^2 - (n+2m)^2)}, \quad (2.43)$$

Then same reasoning can be done for the coefficient $D_{n+2k,n}(z)$ obtaining

$$D_{n+2k,n}(z) = \frac{D_{n,n}^{(2k)}(z)}{\prod_{m=1}^k (n^2 - (n+2m)^2)}. \quad (2.44)$$

Then we can write the scalar potential (2.38) ϕ_m as

$$\begin{aligned} \phi_m(r, \varphi, z) = & \sum_{n=1}^{\infty} \left(\sum_{k=0}^{\infty} \frac{C_{n,n}^{(2k)}(z)}{\prod_{m=1}^k (n^2 - (n+2m)^2)} \right) r^n \sin(n\varphi) \\ & + \sum_{n=1}^{\infty} \left(\sum_{k=0}^{\infty} \frac{D_{n,n}^{(2k)}(z)}{\prod_{m=1}^k (n^2 - (n+2m)^2)} \right) r^n \cos(n\varphi), \end{aligned} \quad (2.45)$$

specifying the term up to $k = 3$ we obtain

$$\begin{aligned} \phi(r, \varphi, z) = & \sum_{n=1}^{\infty} \left\{ C_{n,n}(z) - \frac{C_{n,n}^{(2)}(z)}{4(n+1)} r^2 + \frac{C_{n,n}^{(4)}(z)}{32(n+1)(n+2)} r^4 \right. \\ & \left. - \frac{C_{n,n}^{(6)}(z)}{384(n+1)(n+2)(n+3)} r^6 + \dots \right\} r^n \sin(n\varphi) \\ & + \sum_{n=1}^{\infty} \left\{ D_{n,n}(z) - \frac{D_{n,n}^{(2)}(z)}{4(n+1)} r^2 + \frac{D_{n,n}^{(4)}(z)}{32(n+1)(n+2)} r^4 \right. \\ & \left. - \frac{D_{n,n}^{(6)}(z)}{384(n+1)(n+2)(n+3)} r^6 + \dots \right\} r^n \cos(n\varphi). \end{aligned} \quad (2.46)$$

From the previous equation it is possible to see how, in a 3D case, the n^{th} harmonic component depends on the derivative of the associate multipole coefficient (n) along z . We can simply come back to the 2D case putting all the derivative along z equals to 0.

To be clearer in writing the equation, we can define

$$\begin{aligned} \tilde{C}_n(r, z) & := C_{n,n}(z) - \frac{C_{n,n}^{(2)}(z)}{4(n+1)} r^2 + \frac{C_{n,n}^{(4)}(z)}{32(n+1)(n+2)} r^4 + \dots, \\ \tilde{D}_n(r, z) & := D_{n,n}(z) - \frac{D_{n,n}^{(2)}(z)}{4(n+1)} r^2 + \frac{D_{n,n}^{(4)}(z)}{32(n+1)(n+2)} r^4 + \dots. \end{aligned} \quad (2.47)$$

The eq. (2.46) will be then rewritten as

$$\phi_m(r, \varphi, z) = \sum_{n=1}^{\infty} r^n (\tilde{C}_n(r, z) \sin(n\varphi) + \tilde{D}_n(r, z) \cos(n\varphi)), \quad (2.48)$$

which, as said before, it becomes equal to the canonical multipoles decomposition for \tilde{C}_n equal to $C_{n,n}$.

Finally, the field components at any radius within the bore of the magnet are given by

$$B_r = -\mu_0 \frac{\partial \phi_m}{\partial r}, \quad B_\varphi = -\mu_0 \frac{1}{r} \frac{\partial \phi_m}{\partial \varphi}, \quad B_z = -\mu_0 \frac{\partial \phi_m}{\partial z}, \quad (2.49)$$

Pseudo-multipoles

and, performing the derivatives, we have

$$B_r(r, \varphi, z) = -\mu_0 \sum_{n=1}^{\infty} r^{n-1} (\bar{C}_n(r, z) \sin(n\varphi) + \bar{D}_n(r, z) \cos(n\varphi)) , \quad (2.50)$$

$$B_\varphi(r, \varphi, z) = -\mu_0 \sum_{n=1}^{\infty} nr^{n-1} (\tilde{C}_n(r, z) \cos(n\varphi) + \tilde{D}_n(r, z) \sin(n\varphi)) , \quad (2.51)$$

$$B_z(r, \varphi, z) = -\mu_0 \sum_{n=1}^{\infty} r^n \left(\frac{\partial \tilde{C}_n(r, z)}{\partial z} \sin(n\varphi) + \frac{\partial \tilde{D}_n(r, z)}{\partial z} \cos(n\varphi) \right) , \quad (2.52)$$

where

$$\bar{C}_n(r, z) = nC_{n,n}(z) - \frac{(n+2)C_{n,n}^{(2)}(z)}{4(n+1)}r^2 + \frac{(n+4)C_{n,n}^{(4)}(z)}{32(n+1)(n+2)}r^4 + \dots . \quad (2.53)$$

If now, for example, we want to calculate the B_y component, we could assume to calculate the B_φ for $\varphi = 0$.

$$\begin{aligned} -\frac{1}{\mu_0} B_y(r, \varphi = 0, z) &\approx C_{1,1}(z) - \frac{C_{1,1}^{(2)}(z)}{8}r^2 + \frac{C_{1,1}^{(4)}(z)}{192}r^4 - \frac{C_{1,1}^{(6)}(z)}{9216}r^6 + \frac{C_{1,1}^{(8)}(z)}{737280}r^8 - \dots \\ &+ 3C_{3,3}(z)r^2 - \frac{3C_{3,3}^{(2)}(z)}{16}r^4 + \frac{3C_{3,3}^{(4)}(z)}{640}r^6 + \frac{3C_{3,3}^{(6)}(z)}{64512}r^8 + \dots \\ &+ 5C_{5,5}(z)r^4 - \frac{5C_{5,5}^{(2)}(z)}{24}r^6 + \frac{5C_{5,5}^{(4)}(z)}{1344}r^8 + \dots \\ &+ 7C_{7,7}(z)r^6 - \frac{7C_{7,7}^{(2)}(z)}{32}r^8 + \dots \\ &+ 9C_{9,9}(z)r^8 - \dots \\ &\cdot \\ &\cdot \\ &\cdot \end{aligned} \quad (2.54)$$

This series is truncated at $n = 9$ because it already requires the 8th derivative of the leading dipole term $C_{1,1}$ with respect to the longitudinal coordinate z . It can be seen that the second derivative of the leading term, $C_{1,1}^{(2)}$ gives rise to a r^2 dependence of the field as the term with coefficient $C_{3,3}$. In other words, the dipole field roll-off in the magnet extremities yields a radial field dependence that resembles a (pseudo) sextupole.

In eq. 2.53, we can notice that a dipole field ($n=1$) rolling off the magnet's extremity gives rise to a pseudo sextupole and higher order (odd) pseudo multipoles. Pseudo-multipoles terms have the same angular dependence as the leading terms $C_{n,n}$, but a higher-order radial dependence. Since the pseudo terms are higher even derivatives of the leading terms, their z integrals over the entire magnet length will be zero. The coefficients $C_{n,n}$, are still unknown at this stage. Although they are the leading terms of the series expansion, they are not identical to the B_n components in the expansion of the transversal field. Since the pseudo-multipole terms can be calculated from the leading terms, the problem is reduced to extracting the $C_{n,n}$ from measured or calculated data on the domain boundary.

A way to extract the pseudo-multipoles from boundary data is to measure the function $\tilde{B}_n(r_0, z)$. It is a convolution of the transversal field harmonics $B_n(r_0, z)$ with the kernel defined by the sensitivity of the induction coil¹ that is displaced step-by-step along the magnet axis, ($\tilde{B}_n(r_0, z) = B_n(r_0, z) * k_n(r_0, z)$). Then to solve

$$B_n(r_0, z) = -\mu_0 r_0^{n-1} \bar{C}_n(r_0, z) = -\mu_0 r_0^{n-1} \left(n C_{n,n}(z) - \frac{(n+2)C_{n,n}^{(2)}(z)}{4(n+1)} r_0^2 + \frac{(n+4)C_{n,n}^{(4)}(z)}{32(n+1)(n+2)} r_0^4 - \dots \right), \quad (2.55)$$

for the unknown $C_{n,n}$. This can be done by a Fourier transform of the measured $\tilde{B}_n(r_0, z)$, that is,

$$\mathcal{F}\{C_{n,n}(z)\} = \frac{\mathcal{F}\{\tilde{B}_n(r_0, z)\}}{\mathcal{F}\{k_n(r_0, z)\}} \frac{-1}{\mu_0 r_0^{n-1} \left(n - \frac{(n+2)(i\omega)^2}{4(n+1)} r_0^2 + \frac{(n+4)(i\omega)^4}{32(n+1)(n+2)} r_0^4 - \dots \right)}. \quad (2.56)$$

2.2 Conclusions

In this chapter was presented the pseudo-multipole theory and the mathematical background used to develop the measurement principle and the sensor. It was demonstrated that the traditional harmonic analysis is not applicable in short magnets where is important to measure the longitudinal field profile. In particular, the link between measurements and the pseudo-multipole coefficients was described. It was demonstrated that the field distribution can be reconstituted from measurements performed on the boundary surface by using a short iso-perimetric coil.

¹For coil lengths converging to zero, this kernel would converge toward the Dirac delta distribution and a deconvolution of the measured signal would no longer be necessary.

Part II
Proposal

Chapter 3

Analysis of the pseudo-multipole expansion

To obtain the magnetic field profile of accelerator magnets an innovative way to extract pseudo-multipoles from measurements has been presented in Chapter 2.1. In order to check the quality and to validate numerically the developed mathematical model, some simulations were performed.

Moreover, the design of the transducer and of the all measurement system has been based on the results obtained from the numerical validation where the main parameters, sensitivity and coil length, have been optimized in order to achieve the desired accuracy.

The designed rotating coil presents an innovative geometry that allows to measure the magnetic field in regions where others sensors cannot perform any measurements or cannot achieve the same accuracy. The design, the technical characteristics, the metrological characterization and the calibration of the sensor and of the transducer will be presented in the next chapters.

In the next chapter is described the numerical validation of the mathematical model and the computations of the main design parameters of the sensing coil and of the all transducer.

A particular case study is presented where the magnetic field map for a particular magnet has been computed.

3.1 Numerical model validation at the example of an air-coil magnet

The numerical validation of the mathematical model is mostly required to verify the link between measurements and pseudo-multipole coefficients. The described mathematical model of the pseudo-multipoles was written in MatLab in order to perform the required simulation. As described in Chapter 2.1, the model requires as input the distribution, along the magnet length, of the field harmonics. The longitudinal distributions of the normal and skew harmonics were computed by means of the CERN field computation program ROXIE [28] for a short, air-coil corrector dipole magnet, as shown in Fig. 3.1

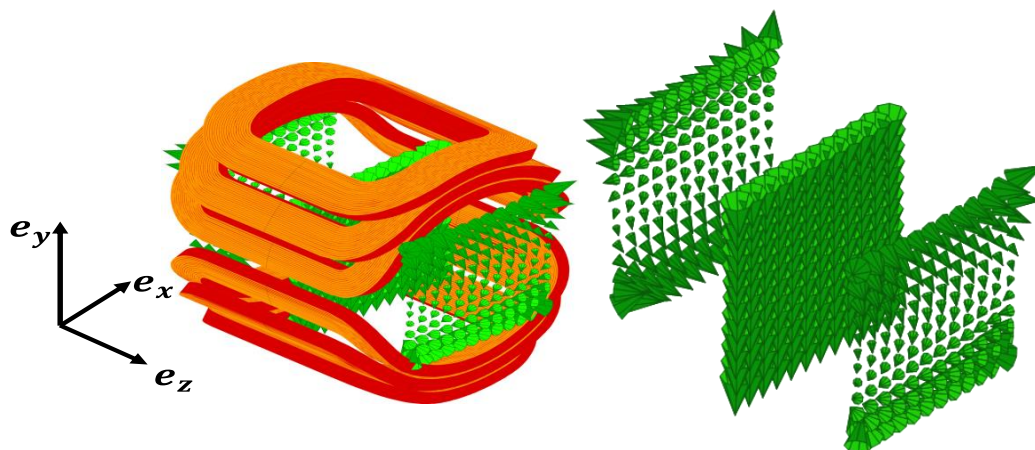


Fig. 3.1 Simulated air-coil magnet.

In Fig. 3.1 we can identify some directions that we will use as a reference in this dissertation. In particular, the axial direction is the z direction considering the reference system located in the center of the magnet aperture. The transversal plane is the plane $x - y$. All the field profile graphs will be plotted considering as zero the center of the aperture magnet where the reference system is located.

The computed harmonic field profiles of the magnet are plotted in Fig. 3.2

3.1 Numerical model validation at the example of an air-coil magnet

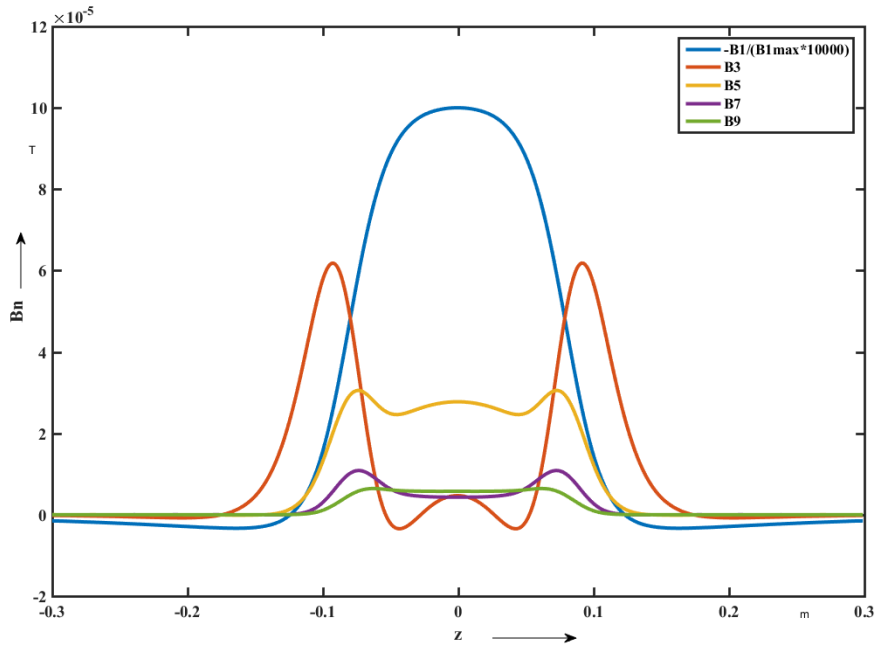


Fig. 3.2 Air-coil field harmonics (B_1, \dots, B_9)

where the B_1 field component is normalized by its maximum value (in the magnet center) and expressed in tenths of mT. The computed harmonics were used in Eq. 2.56 to determine the unknown coefficients $C_{n,n}$ and $D_{n,n}$. The functions test, $K_n(r_0, z)$, that are correlated to the sensitivity function of the probe for each harmonic, are in this case unitary. Knowing the coefficients $C_{n,n}$ and $D_{n,n}$, using the Eq. 2.49 is possible to compute the magnetic field inside the boundary domain.

The computed coefficients are not the harmonic field profile of the magnetic field but only the combination of the coefficients, due to the application of the Eq. 2.47 and Eq. 2.55, give the desired field map. This is shown in Fig. 3.3 where, for the B_1 component along z , at least the derivative of 6th order in Eq. 2.55 is required to obtain, qualitatively, the same shape of the B_1 component.

Analysis of the pseudo-multipole expansion

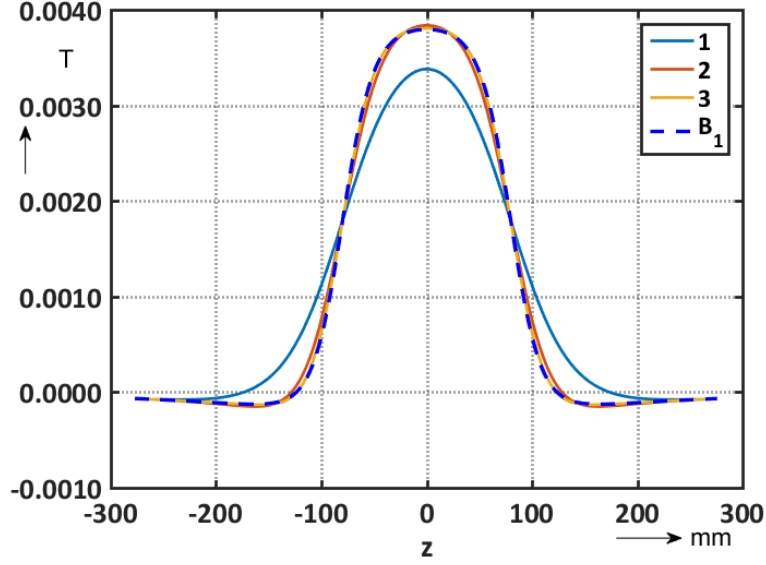


Fig. 3.3 B_1 reconstruction by using 2^{nd} , 4^{th} and 6^{th} derivative order.

The challenge is to find a suitable order n of the pseudo-multipoles $C_{n,n}$ and the highest-order derivatives $C_{n,n}^{(m)}$ in Eq. 2.53 in order to minimize the reconstruction uncertainty of the local magnetic field distribution.

Moreover, the uncertainty of the method will also depend on the step size chosen for the longitudinal displacement of the transducer.

Using computed field distributions and boundary values, a metric for the reconstruction uncertainty can be given by the residual R_B expressed as the normalized root-mean-square error:

$$R_B = \frac{1}{B_y(K/2)} \sqrt{\frac{\sum_{k=1}^K [B_y(k) - B_y^p(k)]^2}{K}}, \quad (3.1)$$

where:

- $B_y(k)$: the y component of the reference field distribution,
- $B_y^p(k)$: the reconstructed y component of the field distribution,
- k : the index of the sampling point,
- K : the maximum number of sampling points,
- $B_y(K/2)$: the reference field component at the magnet center position.

The residual gives the reconstruction uncertainty on the B_y component coming from the pseudo-multipole method. Since the uncertainty is correlated to the order of the pseudo-

3.1 Numerical model validation at the example of an air-coil magnet

multipole and to the derivative order, the procedure shown in Fig. 3.4 was adopted to find the combination of n (order of the pseudo-multipole) and m (derivative order) that gives the smaller residual. The field harmonics were computed at 50 mm reference radius, sampling with a step size of 1.2 mm along the magnet axis. The excitation current of the air-coil was set to 10 A, yielding a central field B_1 of 37 mT. The optimum orders for n and m yield the functional specification for the induction-coil design. In particular, the maximum harmonic order imposes the coil opening angle¹, while the highest order derivative defines the required signal-to-noise ratio and imposes the sampling step along the magnet axis.

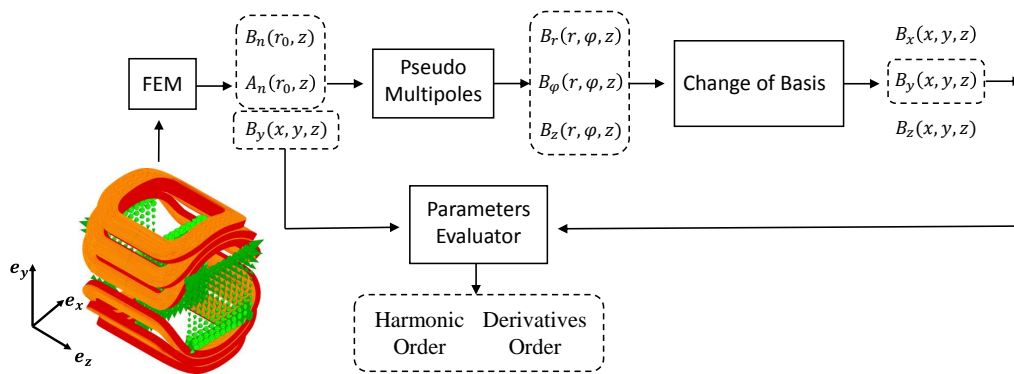


Fig. 3.4 Method for assessing the design parameters: harmonic order n and derivative order m .

Results of this analysis are shown in Fig. 3.5 where the residuals are assessed for different combinations of n and m for the reconstruction of the field along a line on the magnet's vertical plane (at position $y = 50$ mm, $x = 0$ mm, which is at about $2/3$ of the magnet bore radius).

¹In 1.1, the coil sensitivity was proved to be correlated to the opening angle of the tangential coil

Analysis of the pseudo-multipole expansion

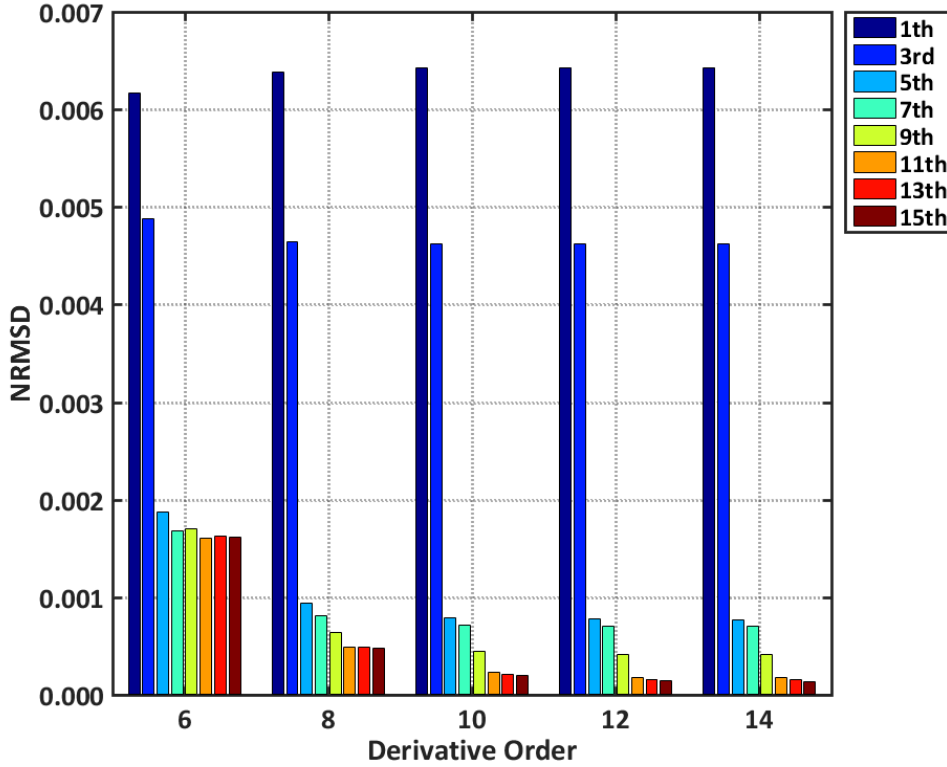


Fig. 3.5 Numerical results of the field reconstruction residual R_B versus derivative m and harmonic order n . $n=[1,\dots,15]$ and $m=[6,\dots,14]$.

The roll-off at the magnet extremity is relatively smooth for the low-order dipole and sextupole components, therefore considering the higher-order pseudo-multipoles for derivatives $m > 10$ yields no improvement. Fig. 3.5 also shows that the multipoles up to B_9 (that is, $n = 9$) must be considered. For simulated field and boundary data, oversampling along z does not improve the result, but can be useful for (noisy) data acquired from the magnetic field transducer. Fig. 3.6 shows the B_y field components and the reconstruction error (in percent) for the pseudo-multipole analysis with $n = 15$ and $m = 14$. The highest error occurs in the fringe field region where the field distribution has the fastest roll off.

3.1 Numerical model validation at the example of an air-coil magnet

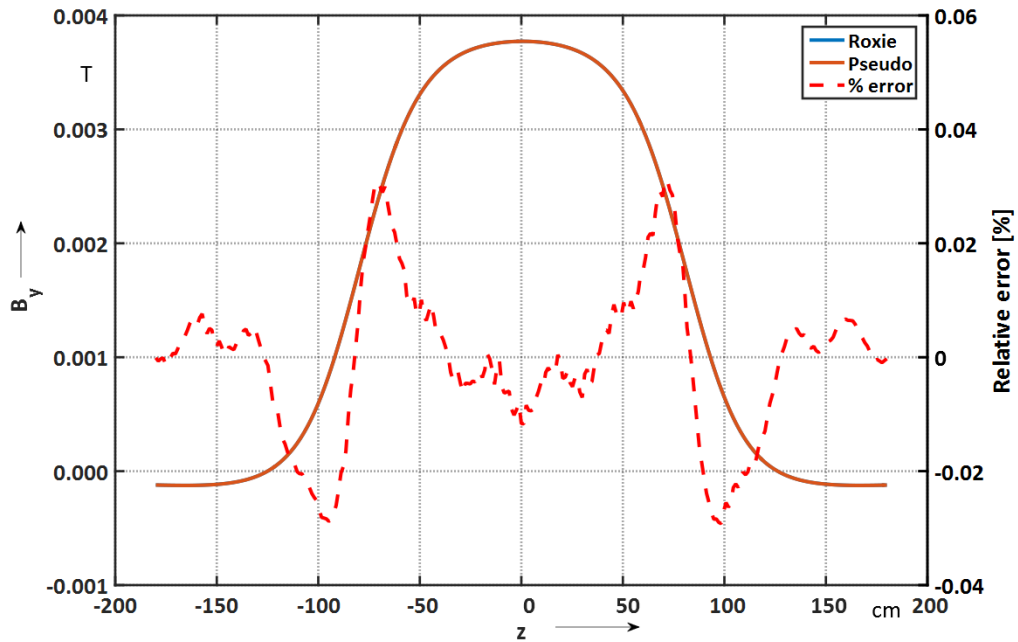


Fig. 3.6 B_y field component and reconstruction error (in percent) along z using $n=15$ and $m=14$.

The numerical test on the mathematical model has shown the validity of the method in field reconstruction. The numerical results give information for the sensor design. It is important to keep in mind that the design of the sensing element cannot take into consideration only the results coming out from this analysis. The roll off of the field harmonics is different for any magnets and a coil optimization could not be performed for each magnet. It is important to remark that in this case the field reconstruction has been performed using simulated data with no noise. In case of noisy data the minimum reconstruction error, Fig. 3.7, is given by using $n=13$ and $m=8$.

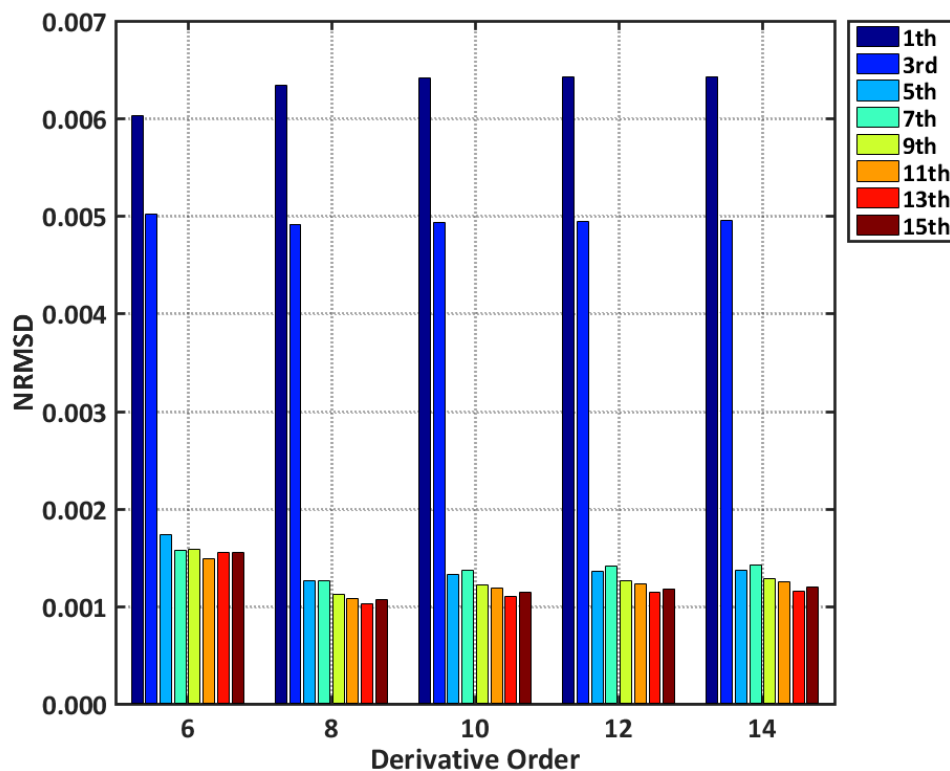


Fig. 3.7 Numerical results of the field reconstruction residual R_B adding random noise on the field harmonics.

Clearly, the noise has the biggest effect on the high derivative order. The random noise on the data had a maximum amplitude of 50 units for the main signal and 10 units for the harmonics. In this case, a maximum reconstruction error on the B_y profile is 0.33% on the fringe field regions and maximum 0.88% in the uniform field region of the magnet $[-50; 50]$ cm.

3.2 Conclusions

In this chapter, the numerical validation of the developed mathematical model was shown. Moreover, the design parameters for the proposed sensing coil have been computed. The numerical validation was performed by using FEM simulations on an air-coil magnet and the sensing coil design parameters were computed by means an optimization in term of the desired accuracy.

Chapter 4

The conceptual and engineering designs of the sensor

In this chapter, we will focus on the conceptual design and the engineering design of the sensing element. As explained in the previous chapters, traditional rotating coils cannot be applied to perform measurements in regions where a strong z -field component is present. A new concept and an innovative geometry of rotating coil sensor has been developed.

4.1 Conceptual design

The proposed rotating-coil magnetometer is a sensor for measuring magnetic field distribution of accelerator magnets. The main characteristic of the sensor is the possibility to perform measurements in regions where a strong z -field component is present. This is definitely the case on fringe field regions of accelerator magnets. An important characteristic is the relatively short length of the sensor that allows to perform local measurements. The sensor must be displaced step-by-step longitudinally along the magnet axis to measure the multipole-field errors as functions of the z -position. Due to the dimension of the coil, the measured harmonics functions will be a convolution between the field profiles and the test functions of the sensing coil. To obtain the correct and desired profile, to use as input of the pseudo-multipole model, the measured harmonics must be deconvoluted by knowing the measurement step size and the sensing coil test functions.

The rotating-coil sensor, besides, must be insensitive to the longitudinal field component present in the magnet extremities. In other words, the integral over the $\mathbf{v} \times \mathbf{B}$ term along the coil end of the induction coil must be zero. When the induction coil is rotated, the integrated voltage is proportional to the flux intercepting the surface traced by this rotation, see Eq.

1.27.

Fig. 4.1 shows the geometry of a classical tangential coil as discussed in [22].

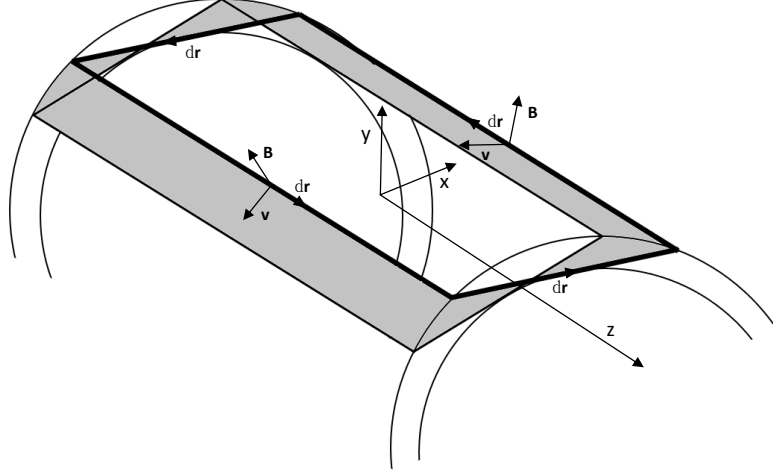


Fig. 4.1 Sensor geometry of tangential coil.

The voltage acquired during the displacement of the magnetometer is integrated by means of a digital integrator at time $t_i(s_i)$. This integrator is triggered by the readout of an angular encoder connected rigidly with the sensor mechanics. In this way the measurement is re-parametrized with respect to the arc length s , and becomes independent of the motion uniformity of the drive system.

$$\begin{aligned}
 \int_{t_1(s_1)}^{t_2(s_2)} U(\partial A) \cdot dt &= \int_{t_1(s_1)}^{t_2(s_2)} \int_{\partial A} (\mathbf{v} \times \mathbf{B}) \cdot d\mathbf{r} dt \\
 &= \int_{t_1(s_1)}^{t_2(s_2)} \int_{\partial A} -\mathbf{B} \cdot (\mathbf{v} \times d\mathbf{r}) dt \\
 &= \int_{t_1(s_1)}^{t_2(s_2)} \int_{\partial A} -\mathbf{B} \cdot (\mathbf{v} dt) \times d\mathbf{r} \\
 &= \int_{\partial A} \int_{s_1}^{s_2} -\mathbf{B} \cdot (ds \times d\mathbf{r}) \\
 &= \int_{A_s} -\mathbf{B} \cdot d\mathbf{a}, \tag{4.1}
 \end{aligned}$$

4.1 Conceptual design

where A_s is not the surface spanned by the induction coil, but the surface traced out by the rim of that surface during the displacement between two angular positions (arc lengths s_1 and s_2); see the gray surface in Fig. 4.1 and Fig. 4.2.

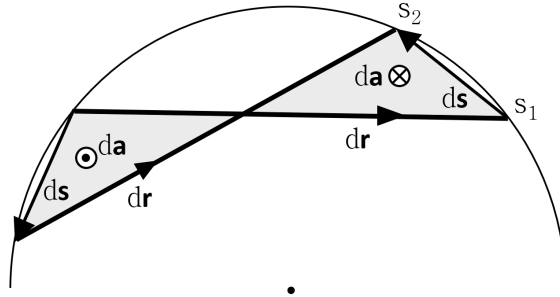


Fig. 4.2 Cross-sectional view of a radial coil turn displaced between two angular positions of arc lengths s_1 and s_2 .

One of the objectives of the research activity is to design a sensor with no sensitivity to the z-field component and with enough sensitivity to the higher-order field harmonics. Notice the surface elements (grey surface) that intercept the longitudinal field component in 4.2. Furthermore, the sensor should have the possibility to compensate the main field component that is by four orders of magnitude higher than the higher-order field harmonics. The proposed solution, shown in Fig. 4.3, does not span any transversal surface when rotated about its axis. This represents the novelty of the proposed solution in comparison with the traditional PCB coils used for magnetic measurements [22, 7].

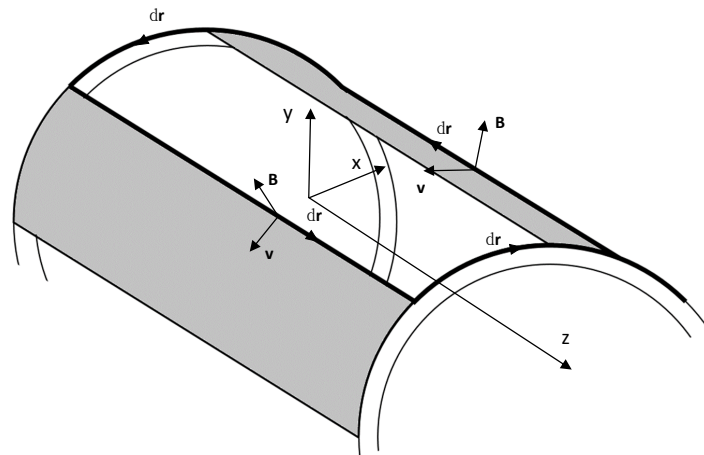
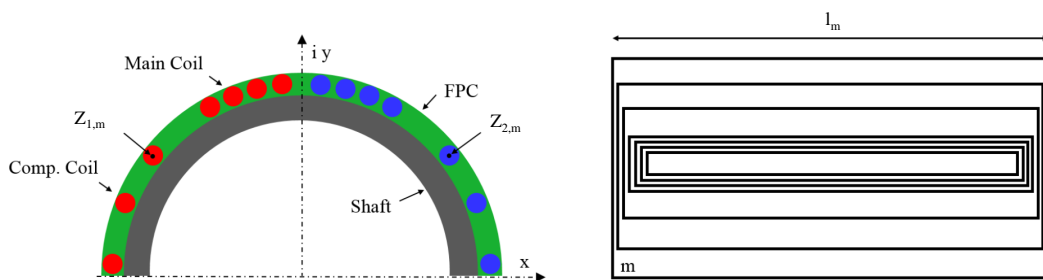


Fig. 4.3 Sensor geometry saddle-shaped, iso-perimetric coil.

An engineering solution to create a sensor with this characteristic is to nest several induction coils on a cylindrical shaft. Fig. 4.4a shows the cross-section of the conceptual design. For an iso-perimetric coil, each turn remains on the same radius and thus is not affected by the longitudinal field component when rotated around its longitudinal axis. Only the perpendicular field components will induce an electric field on the turn.



(a)

(b)

Fig. 4.4 Cross-section of the Flexible Printed Circuit (FPC) induction coil, with main and compensation coils (a) top view (b).

Apart from the particular geometry of the sensor, of extremely importance is the sensitivity to the main and higher-order field harmonics. To optimize the design in term of length, number of layers and sensitivity, the sensor design was based on the equations for the

complex sensitivity factors K_n of a single coil turn [11]

$$K_n := K_n^{rad} + i K_n^{tan} = \frac{Nl}{n} (r_2^n e^{in(\varphi_2 - \varphi)} - r_1^n e^{in(\varphi_1 - \varphi)}), \quad (4.2)$$

with their physical unit $[K_n] = \text{m}^{n+1}$, that is, square meters for the dipole sensitivity. The superscript "rad" indicates the radial component and "tan" the tangential component, r_1 and r_2 are the radii of the go and return tracks, n is the multipole order, and φ_1 and φ_2 are the angular positions of the tracks. Thus, for M loops we obtain

$$K_n = \sum_{m=1}^M \frac{Nl_m}{n} (z_{2,m}^n - z_{1,m}^n), \quad (4.3)$$

where M is the number of loops in the induction coils, N is the number of layers, l_m the length of the single loop of index m , n the harmonic order, and $z_{1,m}$ and $z_{2,m}$ are the complex coordinates of the m^{th} loop (see Fig. 4.4a and Fig. 4.4b).

The design was optimized by means of the CERN field-computation program ROXIE [28]. Two coils are combined on a common shaft. The central coil, with the smaller opening angle, is sensitive to higher-order field harmonics. The lower coil (with larger spacing between the turns) is designed to be sensitive only to the main dipole field component. From the theory of $\cos \Theta$ coils [29], we know that a single shell of $\pi/3$ rad creates the smallest amount of higher-order field components outside the shell and therefore minimizes the mutual inductance coefficient to the magnet. The two induction coils are then connected in series with opposite polarity so that the main field component is canceled out, and thus the signal-to-noise ratio is increased. This is the principle of the bucking coil, that is, increase the signal-to-noise ratio on the higher order harmonics by canceling out the main field component.

Fig. 4.5 shows the result of the mathematical optimization. In red the position of the main induction coil and in blue the compensation coil.

The conceptual and engineering designs of the sensor

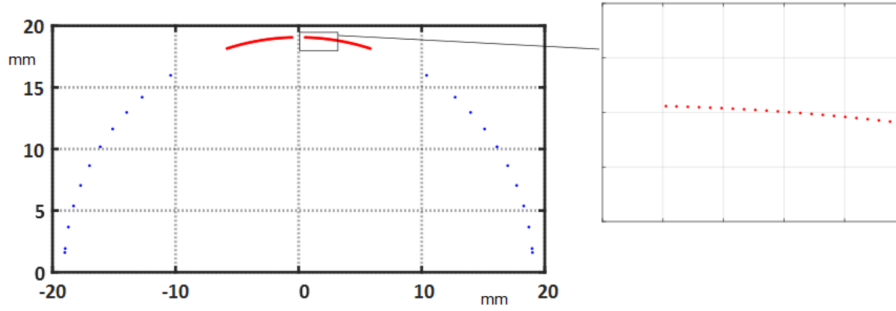


Fig. 4.5 Optimized design of the dipole compensated coil with a magnified view of the inner coil (insert).

The computed (design) sensitivity factors for the main and compensation coils are shown in Fig. 4.6a. The results of the compensation scheme are shown in Fig. 4.6b. As the higher-order sensitivity factors scale with $1/r^{n-1}$ it is appropriate to introduce a scaling factor, that is, the measurement reference radius R_{ref} and define

$$S_n := \frac{K_n}{R_{\text{ref}}^{n-1}} \quad (4.4)$$

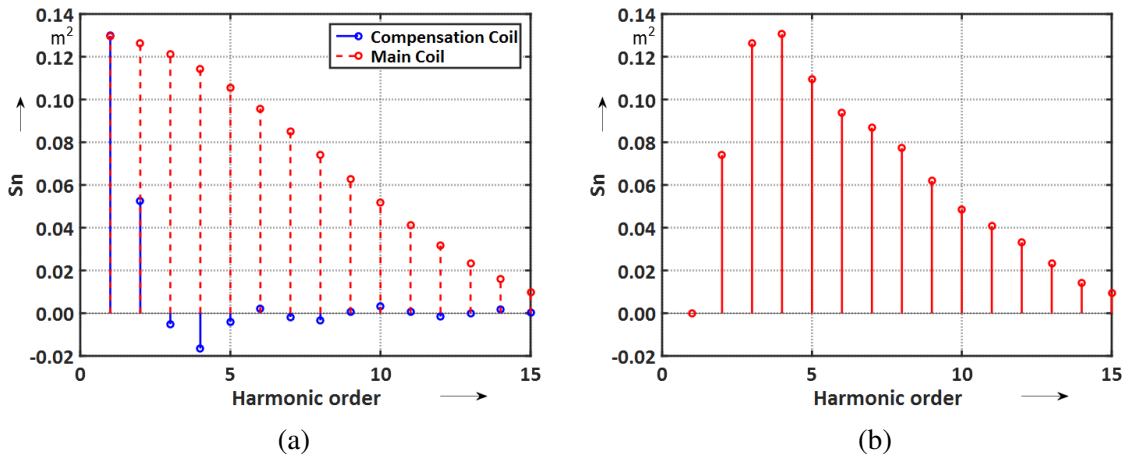


Fig. 4.6 Sensitivity factors S_n at $R_{\text{ref}} = 19.065$ mm for the main and compensation coils (a) and for the compensated scheme (b)

An important feature, that distinguishes substantially the designed coil from the flexible coil presented in [20], is the absence of a "blind eye" for field harmonics up to the 15th order. The blind eye is the multipole order n at which the opening angle is an integer fraction of 2π . In other words, the coil is completely insensitive to a multipole of order n when $n\delta = 2\pi$.

4.1 Conceptual design

The ideal compensation of the main field component is a mathematical abstraction, however. Manufacturing tolerances make it impossible to produce nested coils spanning identical surfaces. As a quality factor, the compensation ratio (also known as bucking ratio) is defined as:

$$Q_c = \frac{S_1^m}{S_1^m - S_1^c} \quad (4.5)$$

where S_1^m and S_1^c are the dipole sensitivities of the main and compensation coils. Compensation ratios approximately 100 are usually considered as an achievement. Fig. 4.7 and Fig. 4.8 show a 3D rendering of the coil design produced by using the Flexible Printed Circuit (FPC) technology. From now we will consider the iso-perimetric sensing coil produced by using the FPC technology. In 6.1 will be described, in detail, the iso-perimetric coil production.

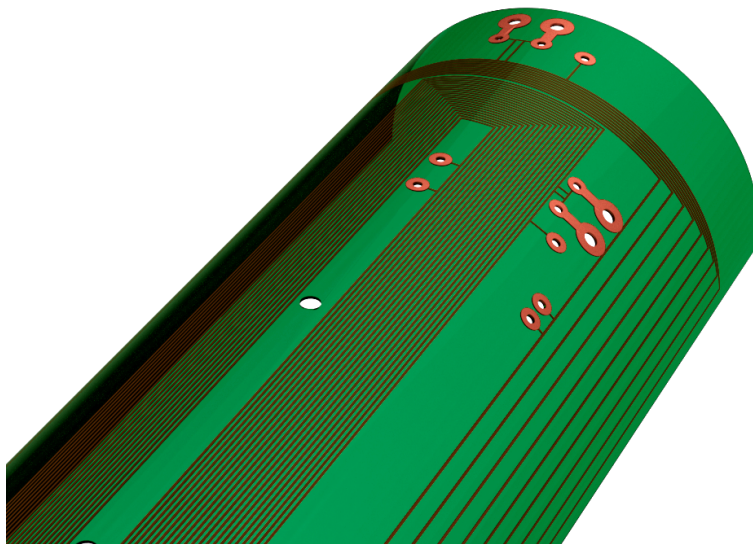


Fig. 4.7 3D rendering of the coil design (connection view).

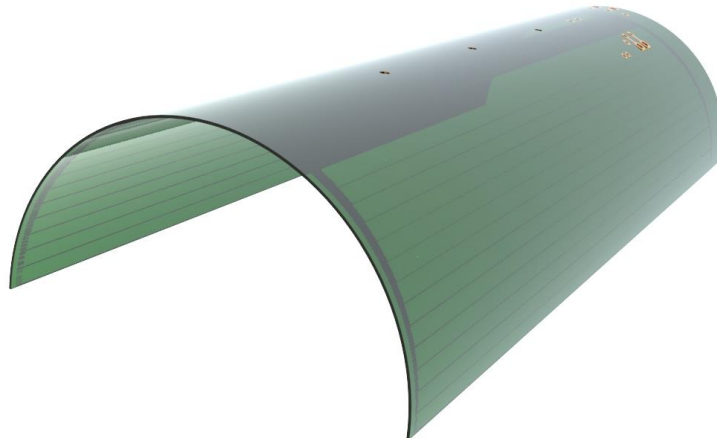


Fig. 4.8 3D rendering of the coil design.

4.2 Sensitivity factors and sensor length

Rotating-coil magnetometers are usually designed to be longer than the magnetic length of the magnet under test, or at least long enough to cover the entire fringe field area. The sensitivity factors of these coils are given considering the geometric mean dimension of the magnetometer for the geometrical measuring radius.

For short coils, however, the coil-track thickness cannot be neglected with respect to their overall length. In particular, for coils produced in PCB technology, a certain gap size is required between the single turns, which increases the track thickness and limits the maximum number of turns. Therefore, the sensitivity factors must be expressed locally as a function of the longitudinal position within the coil. This yields the kernel for deconvoluting the measured multipole distribution.

To clarify how to compute the sensitivity functions, let us consider a one-layer, PCB of three induction coil loops with external length L of 10 cm and a spacing of 1 cm between them, as illustrated in Fig. 4.9.

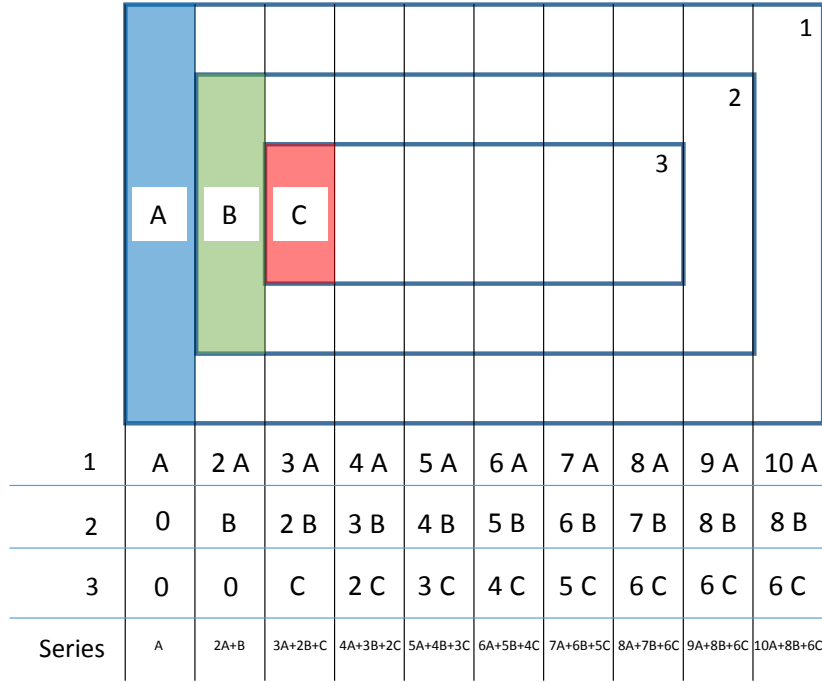


Fig. 4.9 Schematic of the sensitivity factor analysis.

The spanned surface (that is the K_1 value) for a series connection of the three turns is given by the cumulative sum over the contributions from the three turns, that is, the last row in Fig. 4.9. The finite difference of this sum yields the sensitivity function (convolution kernel) $k_1(z)$.

Considering a flexible printed circuit with M turns, a total length L , and a step size t given by the distance between each turn in the coil end, we get for the n^{th} harmonic,

$$V_n(m, i) = \frac{t(i-m+1)}{n} \left(z_{2,m}^n - z_{1,m}^n \right), \text{ for } i > m, \quad (4.6)$$

where $m \in 1, 2, \dots, M$ and $i \in 1, 2, \dots, I, I = L/t$. The sums of the contributions at I (last column in Fig. 4.9) are the sensitivity factors corresponding to the ones shown in Fig. 4.6a.

$$K_n = \sum_{m=1}^M V_n(m, I). \quad (4.7)$$

The conceptual and engineering designs of the sensor

In order to calculate the sensitivity function $k_n(z_i)$, the finite difference of the sums over $V_n(m, i)$ is required:

$$k_n(z_i) = \frac{\sum_{m=1}^M V_n(m, i) - \sum_{m=1}^M V_n(m, i-1)}{t}, \quad (4.8)$$

for $i \in 2, 3, \dots, I$. The functions $s_n(z_i) = k_n(z_i)/R_{ref}^{n-1}$ for the induction coil are given in Fig. 4.10.

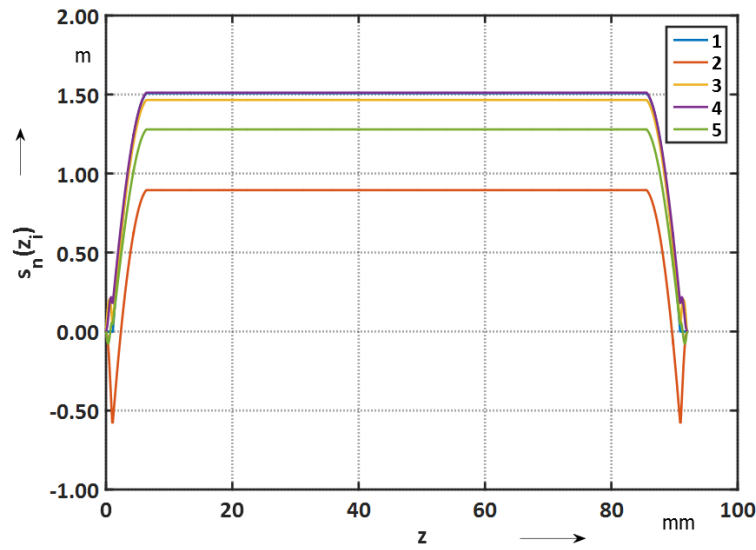


Fig. 4.10 Compensated coil sensitivity along the induction coil ($R_{ref} = 19.065$ mm).

The main difference between the classical approach (coils that have a track thickness that is negligible with respect to the coil length), and the printed circuit technology, is that its sensitivity is a function that varies with the multipole order; see Fig. 4.11. Therefore, the geometric mean length does not correspond to the magnetic length. The deviation from the "hard-edge model", which is employed in the case of the classical coils, is shown in Fig. 4.11.

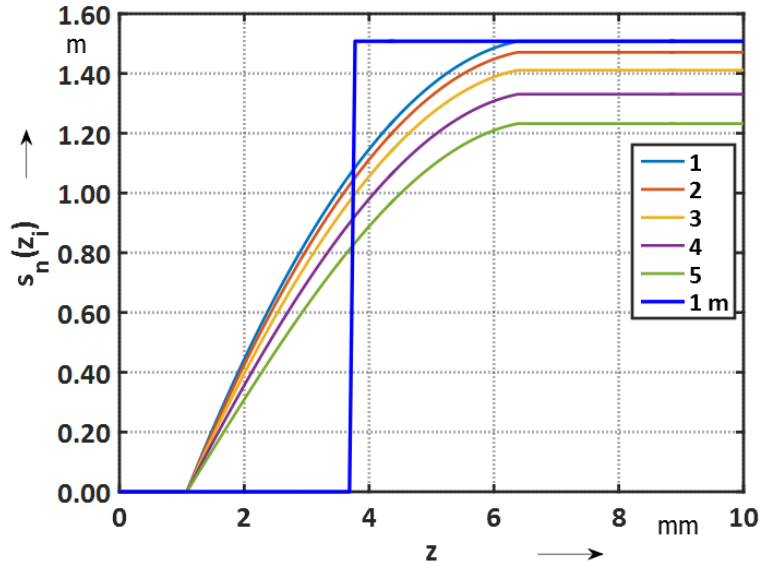


Fig. 4.11 Sensitivity functions $s_n(z_i)$ along the extremities of the main induction coil and hard-edge model (geometric mean length).

The differences between the geometric mean and magnetic lengths (L_G and L_M) are given in Fig. 4.12 for the multipole order n .

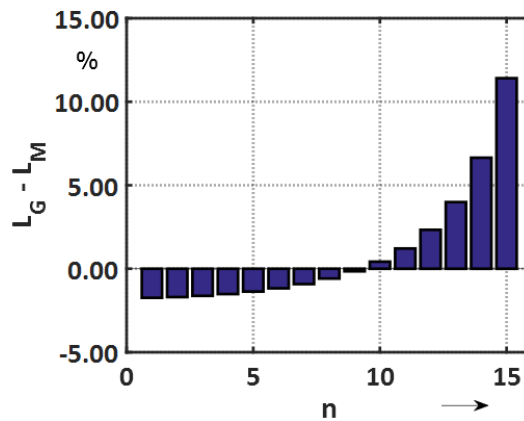


Fig. 4.12 Differences between the geometric mean and magnetic lengths as a function of the multipole order n .

4.3 Sensitivity factor calculation for PCB coils

In the previous section, it has been highlighted that the standard procedure for the sensitivity factor computation cannot be applied for iso-perimetric induction coils. In fact, the particular

The conceptual and engineering designs of the sensor

shape of the sensor and the position, on the 2D section view, of every single track do not allow to consider any average position or radius. This is the reason why the classical mathematical equation of the K_n computation has been modified and adapted to the new coil geometry. Furthermore, analysis have been performed on the sensitivity computation of a standard flat PCBs. Flat PCBs must be characterized by having a really high number of turns to have enough sensitivity. This can be done using many layers or many turns on each layer. Usually, a trade-off between the two parameters is required. The ends of the PCB coil are considerably large in comparison with traditional winding. For example, a PCB with ten tracks has an end width of 2.5 mm. Clearly, it is not always possible to approximate the coil as one filament concentrate in an average position. Considering a PCB composed of 10 layers, 10 tracks each layer with external dimension 95 x 11 mm, the sensitivity factor (S_1) calculated by considering the mean position of the coil is 0.08810 m², by calibration is 0.08808 m² and by using a computation that takes into account the position and the length of each single tracks it is 0.08811 m². Fig. 4.13a shows the sensitivity factors (S_n), at radius 11.4 mm, calculated by the standard procedure in black and by using the proposed solution in red. In Fig. 4.13b is shown the difference in percentage between the sensitivity factors computed by using the standard procedure (considering the mean position) and the introduced methodology (considering radius, opening angle and length of each single loop).

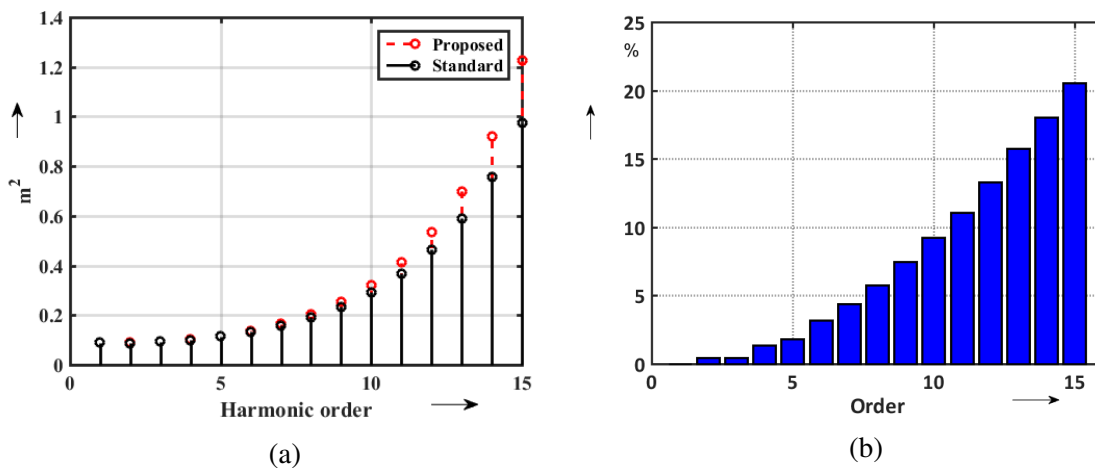


Fig. 4.13 (a) Sensitivity factor at 11.4 mm from standard k_n formula (red) and proposed procedure (blue), (b) difference in percentage

As expected for the surface computation (S_1) there is no difference. Instead, considering the highest order sensitivity factors that have a dependence on the power of the radius according to r^{n-1} , an exponential error is computed. For the sextupole sensitivity S_3 a difference of 0.43% is calculated.

4.4 Uncertainty analysis

The sensor performance, in terms of compensation ratio and sensitivity, is affected by manufacturing tolerances during the FPC production. The uncertainty on the sensitivity factors is analyzed in order to derive the required production tolerances. Both random and systematic errors on the track positioning are considered.

Uniformly distributed, pseudo-random errors in the range of $\pm 30 \mu\text{m}$ are considered for the track positions. The complex coordinates of each track can be written as

$$z_m = r \cos\left(\frac{a+x}{r}\right) + ir \sin\left(\frac{a+x}{r}\right), \quad (4.9)$$

where a is the nominal arc length calculated by ROXIE, r is the nominal radius of the shaft, and x the random error. The assumption of a random error not exceeding $\pm 30 \mu\text{m}$ is reasonable because larger errors would lead to short circuits because the insulating thickness between turns is only $50 \mu\text{m}$. The most sensitive parameter for quantifying the track-positioning error is the compensation ratio, see Eq. 4.5. Table 4.1 shows the resulting compensation ratios for different levels of random errors.

Position uncertainty	Dipole compensation ratio
none	130000
$\pm 20 (\mu\text{m})$	17000
$\pm 30 (\mu\text{m})$	16000

Table 4.1 Compensation ratios for different track-positioning errors.

The flexibility of the induction-coil sensor may result in a lengthening or compression of the printed circuit during assembly on the shaft and therefore may result in systematic errors on the track positions. Simulations were carried out considering a maximum error of $\pm 100 \mu\text{m}$ on the total width. Fig. 4.14a shows the results of the compensation ratio for a dipole-compensated coil. The maximum acceptable systematic error that will ensure a compensation ratio higher than 100 is therefore $\pm 80 \mu\text{m}$.

Apart from mounting/gluing the flexible printed circuit on the shaft, further significant errors arise from the radius tolerance on the shaft itself. Simulations were carried out considering a maximum error of $\pm 300 \mu\text{m}$ on the nominal radius of 19.065 mm . For a compensation ratio larger than 100, the shaft tolerance must be better than $\pm 200 \mu\text{m}$; see Fig. 4.14b.

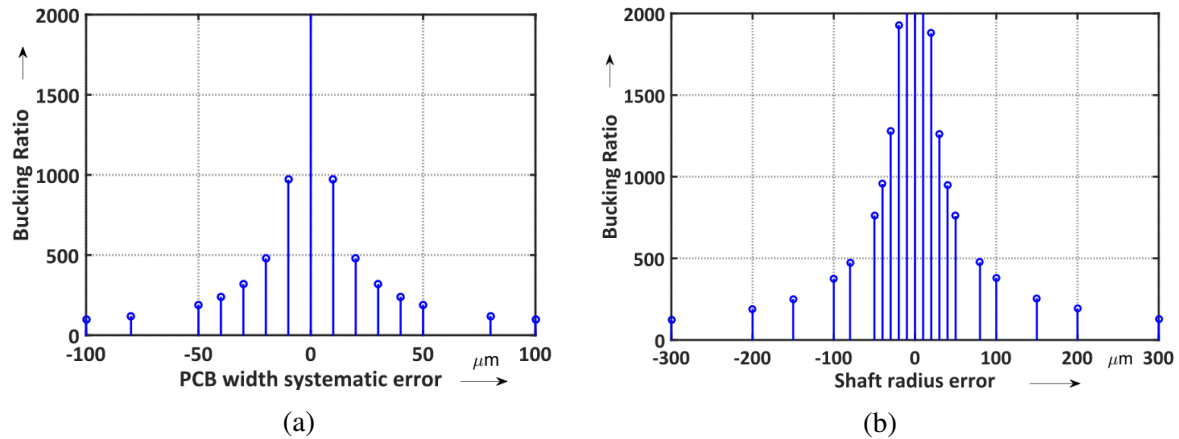


Fig. 4.14 Compensation ratio of a dipole-compensated coil with systematic error in PCB width (a) and compensation ratio of a dipole-compensated coil at varying the tolerance on the shaft radius (b).

4.5 Design of radial and tangential sensing coils

The effect of the axial field component on the short rotating coil measurements cannot be easily identified. A possible way to obtain this information is to perform a longitudinal scan by using short rotating coils and then compare the integrated field harmonics obtained by summing the local harmonics with the integrated field harmonics measured by using a long, traditional, rotating coil.

Another possible solution could be to measure the field distribution by using a field mapper and compare it with the measurements performed by using the short rotating coils (traditional or iso-perimetric). Unfortunately it is not easy to measure, with high accuracy, the magnetic field profile of accelerator magnets.

Even with the most sophisticated field computation tools and the most stringent follow up on magnet production there will be misalignment, material property fluctuations, and mechanical tolerances during the production phase, which in turn requires magnetic measurements for the qualification of the magnet for the operation in the accelerator tunnel. Furthermore, it is not easy to consider hysteresis effects.

For this reason, the first transducer prototype was conceived to have three different typologies of sensors on the same mechanical structure.

The idea behind this concept is to measure at the same time, ensuring compatibility between the measurements, the magnetic field in the same regions and compare the field profile

4.5 Design of radial and tangential sensing coils

measured by the three sensors. In particular, the first transducer prototype was assembled with a Hall probe sensor, an iso-perimetric coil and a radial coil.

The three sensors were assembled in a way that the radial coil was covering the entire inner surface covered, externally, by the iso-perimetric coil and the Hall probe just below the flexible printed circuit, measuring on the same radius. Mechanical tolerances of the first prototype did not guarantee the requirement of having the same measuring radius. For this reason was required the application of the scaling laws on the iso-perimetric coil results (by design and concept, only the results of the iso-perimetric coil can be scaled).

For the second prototype, the transducer has been conceived to have the possibility of performing measurements with the three different typologies of rotating coil (radial, tangential and iso-perimetric coil), having the same theoretic measuring radius, the same average sensor length and approximately the same surface in order to be able in measuring the same entity of the magnetic field.

The same measurement radius is required to avoid the application of the scaling law, not valid anymore in the fringe field regions.

The same length, to guarantee the convolution on the same quantity of magnetic field distribution (performing a scan with a short rotating coil, the measured field is averaged by the sensitivity function of the coil).

The same surface is needed to guarantee the same signal amplitude from the main magnetic field component. It allows to compare the signal-to-noise ratio of the three different coils.

For this purpose, after the design of the iso-perimetric coil sensor, the radial and tangential coil sensor design was required. The design of the radial and tangential coil has been based on standard printed circuit board technology. The layout of the radial coil was conceived to produce the tangential coils from the same PCB.

In particular Fig. 4.15 shows the schematic layout, created on Altium, of the radial PCB coil.

The conceptual and engineering designs of the sensor

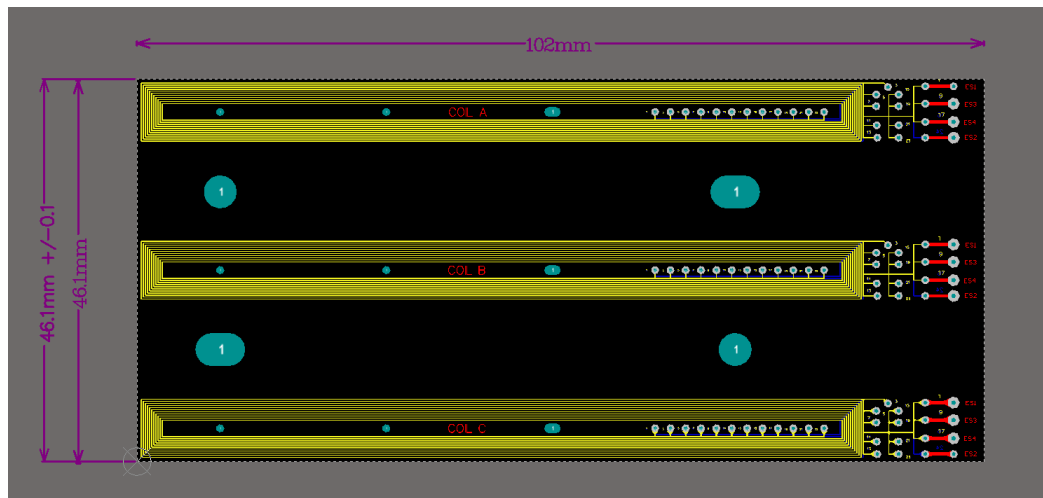


Fig. 4.15 Radial PCB coil layout for the second transducer prototype.

The radial coil sensor is composed of an array of three sensing coils to obtain the dipole compensation. Each coil has 24 layers and each layer is composed of 11 tracks. Tab. 4.2 resumes the main PCB parameters.

Radial Coil	
N° Layers	24
N° Coils	3
N° Turns	11
Coil external length	86.9 mm
Coil internal length	81.7 mm
Coil inner width	2 mm
Coil external with	1 mm
Theoretical radius	19.065 mm

Table 4.2 Main dimensions of the radial PCB coil.

The theoretical surface of each coil is 0.1 m^2 . In yellow the coil tracks of the even layers. By using the same PCB produced for the radial PCB coil, but cutting the three coils (Coil A, Coil B, Coil C), is possible to obtain the coils for the assembling of the tangential coil transducer, see Fig. 4.16.



Fig. 4.16 Tangential PCB coil layout.

These three PCBs will be then positioned on a precise shaft to guarantee the measurements radius and the parallelism between the coils.

The described PCBs (for tangential and radial coil) are built assembling the layers, based on the design of only two layers. Basically, it was required to design only two layers, a design for the even layers and a design for the odd layers. Thanks to this technique, the design and production are much faster. The electrical connections between layers are then made during the assembling process of the PCB where only the connections on the respective (correct) Vertical Interconnect Access (VIAs) are left.

4.6 Conclusions

In this chapter the coil conceptual design, the new approach for the sensitivity factors analysis and the uncertainty analysis of the geometrical tolerances for the coil production were shown. Since traditional rotating coils cannot be used to perform measurements in regions where a strong z-field component is present, a new concept and an innovative geometry (isoperimetric) of a rotating coil sensor was developed. Furthermore, since for short coils the coil-track thickness cannot be neglected with respect to their overall length, the sensitivity factors were expressed locally as functions of the longitudinal position within the coil. The uncertainty on the sensitivity factors was analyzed considering manufacturing errors in order to derive the required production tolerances. The uncertainty on the sensitivity factors was analyzed in order to derive the required production tolerances. Both random and systematic errors on the track positioning were considered.

Chapter 5

Conceptual and engineering design of the rotating-coil transducer

The measurement of the local field distribution in accelerator magnets requires the transducer design to provide the possibility to displace the sensing coil along the magnet length. Furthermore, the transducer must be assembled with an iso-perimetric coil to be able in measuring in the fringe field regions. In [16] is described a field mapping realized by eight Hall sensors that can be displaced in z along the curved central particle trajectory of the *HESR* dipole magnets. The Hall probes are then rotated in each z -position in order to measure the local magnetic field. In [3], a rotating coil transducer for local measurements of magnetic field quality in magnets is proposed. The described solutions are based on rotating Hall probe, in the first case and, on a short radial coil, in the second case. Hall probes are not always suitable to get harmonics and the short radial coil has been demonstrated that are affected by the z -field component. Another important limit of the two proposed solutions is the bulky geometry that often could limit the sensitivity to high harmonic orders. In general, to measure harmonics in accelerator magnets is preferable to measure at the biggest radius as possible where the harmonic content is bigger. This is due to their exponential behaviour.

The proposed transducer was conceived to be not sensitive to the z -field component and to cover, as much as possible, the magnet aperture.

The design of the transducer requires the necessity to have a cylindrical surface where to install the induction coil, ensuring the rotation of the sensor on the desired radius. Since the measurand is a static, DC field, turning the coil at constant speed will induce electromotive force in the coil itself that will generate a 2π periodic wave that allows the computation of the field harmonics.

The idea is to develop a cylindrical shaft with opportune diameter where to allocate the flexible circuit board having enough precision in term of mechanical tolerances. Another

important feature of the transducer is to have the possibility of making a direct comparison between the traditional coils and the innovative geometry presented in this thesis.

In the first part of the next chapter, the design of the transducer for proof of principle is described.

In the second part of the chapter, the design of three transducers based on the three designed sensors (iso-perimetric, radial, and tangential coil) is illustrated.

5.1 Rotating-coil transducer and bench design for the proof of principle

The design of the transducer for the proof of principle was based on having a direct comparison between the traditional rotating coil and the iso-perimetric coil.

5.1.1 The rotating-coil transducer

The first prototype for the proof of principle of the transducer was designed to be realized using 3D printing technology. In this configuration, the sensor must be positioned, glued, on a cylindrical shaft in order to preserve the iso-perimetric geometry. Fig. 5.1 shows the assembly of the transducer. The shaft is a cylindrical tube on which the FPC is glued or wounded and on the extremities are installed two ceramic ball bearing.

Since the transducer has to rotate (at constant speed) in a static magnetic field, non-magnetic and non-conductive materials can be used for its production.

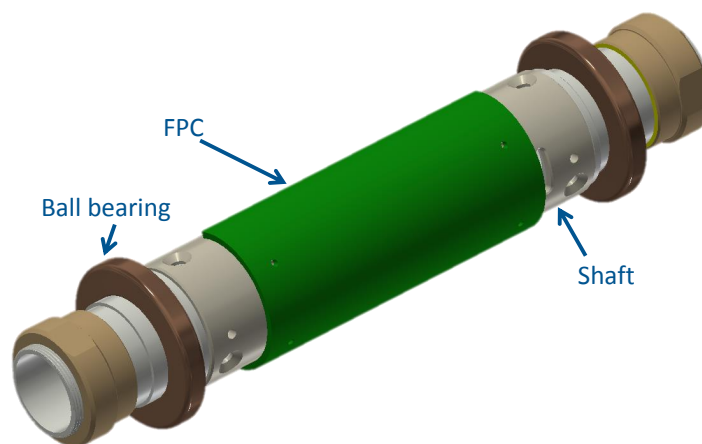


Fig. 5.1 Rotating-coil transducer assembly for proof of principle.

5.1 Rotating-coil transducer and bench design for the proof of principle

Fig. A.1 in Appendix A shows the design of the shaft in detail. The shaft presents an external diameter of 40 mm with a tolerance of ± 0.05 mm and two slots for the positioning of the Hall probe. In fact, the transducer will be assembled with a Hall probe sensor on the external radius and one Hall probe on the center of the shaft (close to the rotational axis). The two slots shown in the section view of the coil are the slot where the radial PCB coil will be inserted.

5.1.2 The measurement station

The bench design was based on the requirement of having a sensor that has to be translated inside the magnet aperture along the z -direction with high precision.

The conceptual idea is presented in Fig. 5.2 where schematically we can see the sliding system, the rotating coil sensor and the roll off of the main magnetic field profile.

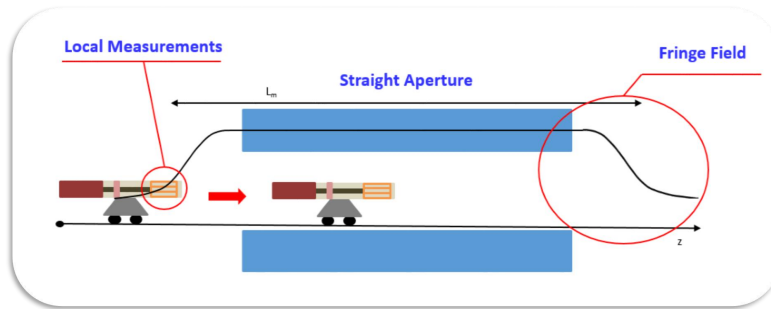


Fig. 5.2 Measurement system for measuring the transversal field harmonics along z .

The bench design for proof of principle was based on an available slide system composed of a bench having two linear stages that can be translated transversely. In Fig. 5.3 is presented the set-up of the measurement for proof of principle. In particular, the shaft containing the three transducers is connected through an extension tube to the Micro Rotating Unit (MRU) and inserted in a stainless steel tube (mechanical support). The MRU is the standard unit used at CERN for rotating coil measurements and is furnished with an angular encoder having 4096 steps per turn, 3 slip rings with a total of 54 signals and a DC motor equipped with a reduction for providing high torque.

The transducer in this set-up is free to rotate inside the stainless steel tube thanks to the ceramic ball bearings. To translate the device inside the magnet aperture, the all structure (MRU and tube) has to be translated using the transversal linear stages. Since the precision in positioning is not accurate enough for our purpose ($\pm 60 \mu\text{m}$) a Leica system was positioned

Conceptual and engineering design of the rotating-coil transducer

on the open side of the tube to measure the displacement. This is possible thanks to a reflector installed at the end of the transducer.

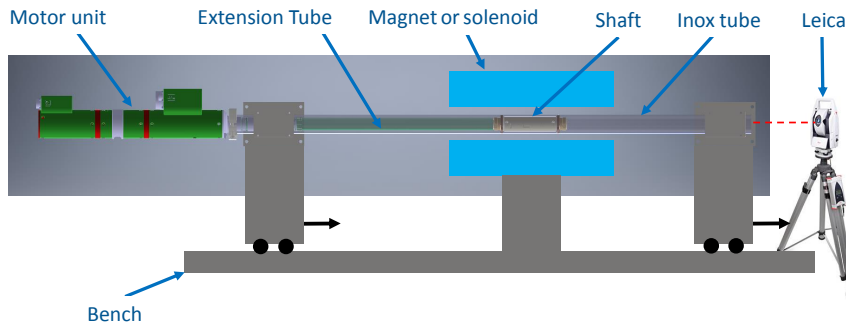


Fig. 5.3 Concept design of a 2D mapper for rotating coil scanner.

In [12] a “train” system solution was proposed. The advantage was to measure the longitudinal position of the sensor in the magnet aperture by using a linear encoder. On the other hand, the bulky structure reduced the measuring radius. The proposed solution guarantees to use the maximum available aperture radius, but the sensor position is measured by using a laser tracker ($\pm 100 \mu\text{m}$).

Fig. 5.4 shows the installation used to perform some functional validation tests of the transducer in the reference dipole magnet. We can identify the motor unit and the support tube. The transducer is located inside the tube and connected mechanically and electrically to the rotor on the motor unit.

5.2 Transducer and bench concept design; second prototype



Fig. 5.4 Bench set-up for validation measurements.

5.2 Transducer and bench concept design; second prototype

5.2.1 The transducer

For the production of the second prototype, some modifications were required on the mechanics of the transducer. In fact, from the experience on the first prototype, we were able to identify the defects and to correct them in order to improve the quality and reduce the uncertainty of the measurements.

The weak point of the first prototype was without any doubts the mechanics. In fact, the cylindrical shaft produced using 3D printed technology, affected the bucking ratio of the transducer reducing the capacity of cancel out the main field component. As result, we obtained a low signal to noise ratio for high harmonics orders.

The new concept design is shown in Fig. 5.5.

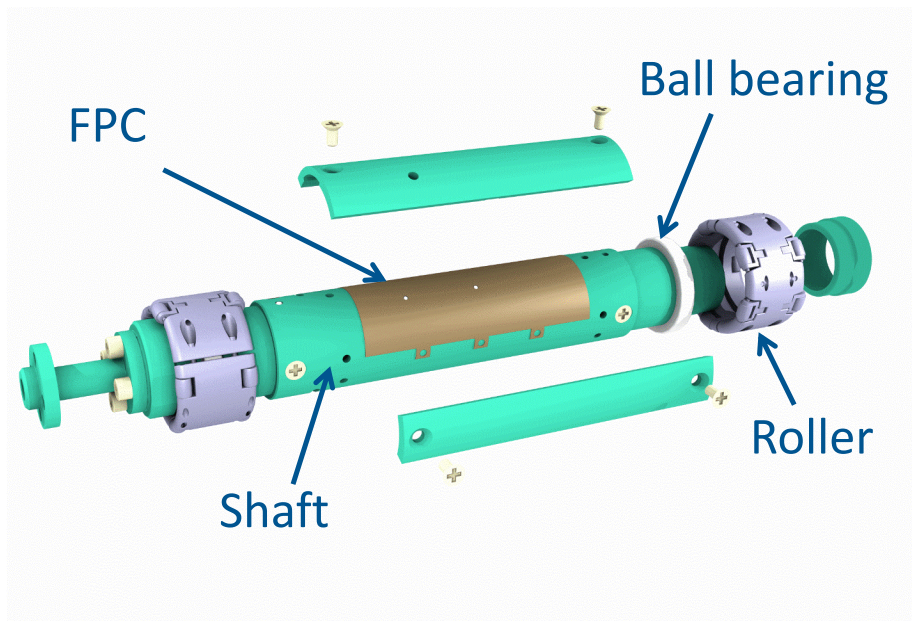


Fig. 5.5 Second prototype transducer's assembly.

The second prototype design has two main important improvements. First, the all transducer is produced in Epoxy G11 Fiberglass with higher mechanical properties and secondly, a clamping system has been designed to keep the flexible circuit board in the position.

The FCP is aligned on the cylindrical shaft using two alignment pins, while it is fixed on the shaft by using three covers that press it in the proper position. Using the three covers is possible to ensure the same pressure along the all FCP and to avoid the glue or double layer tape that introduce uncertainty on the final radius. Fig. A.2 in Appendix A shown the assembly of the transducer for the iso-perimetric coil.

On the first prototype for proof of principle, three different sensors were installed in the same transducer. For the second prototype, was decided to build separately iso-perimetric, radial with Hall probe and tangential coil shaft. To ensure the repeatability of the measurement in term of positioning, the shafts are equipped with a reflector to measure the position by using the Leica system. Fig. 5.6 shows the radial coil transducer configuration and the 5.7 the tangential coil transducer configuration.

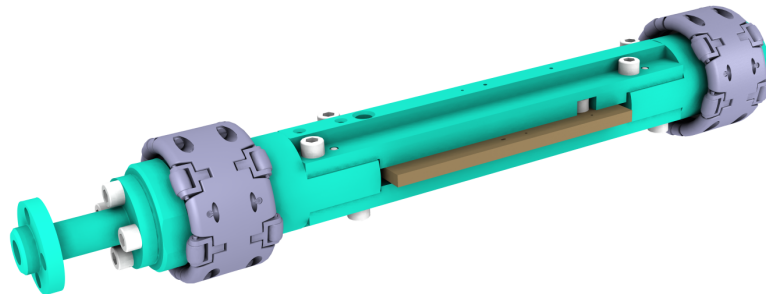


Fig. 5.6 Radial coil transducer assembly.

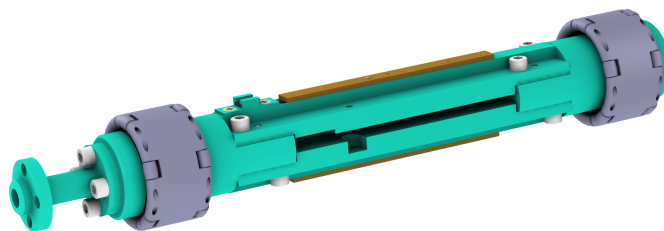


Fig. 5.7 Tangential coil transducer assembly.

The assembly drawings for the radial and for the tangential coil transducers are illustrated in figures A.3 and A.4 (Appendix A).

Conceptual and engineering design of the rotating-coil transducer

Fig. 5.8, instead, shows the assembly of the three transducers connected in series. In fact, one possibility would be to install the three shafts together and acquire the all signals at the same time. In this way, only one scan would be required to have the longitudinal field profile from the four typologies of sensors.



Fig. 5.8 Rendering of the shaft assembly in series configuration (shaft chain).

5.2.2 Deformation, stress and natural frequencies analysis

The G11 for the fabrication of the transducer was chosen after having performed some mechanical deformation and stress analysis on two different materials, DERLIN 100 and G11. Even if it is well known that the DERLIN 100 has less stiffness than the G11, it was considered as possible material to simplify the procurement of the component having the possibility of producing the components in-house. In fact, the epoxy resin G11 requires particular precautions for the production that force the production into specialized companies. The main considerations taken into account for the next simulations are listed:

- The solid mechanics' simulations and eigenfrequencies for the iso-perimetric shaft and the for the assembly with the three shafts in a row was carried out using Comsol Multiphysics 5.3a,
- the gravity acceleration is 9.81 m/s^2 ,
- the materials are: G11 and Delrin 100.

5.2 Transducer and bench concept design; second prototype

First, it is necessary to analyze the effect of gravity in every single shaft and then in the final assembly. On the iso-perimetric shaft, the maximum displacement, due to the weight force, occurs near the central part of the shaft where the center of gravity is located with a maximum displacement value of $0.16 \mu\text{m}$. For the case of Delrin 100, the maximum value is $0.34 \mu\text{m}$, which represents the double of G11.

For the assembly, using only three ball bearings (one for each shaft) instead of the six that would correspond in the case that two ball bearings are used for each shaft, the maximum total displacement is $19.1 \mu\text{m}$. Delrin 100 shaft shows a maximum value of $39.1 \mu\text{m}$, which is more than the double of G11.

The natural frequencies in which a structure would get into resonance state are called eigenfrequencies. The natural frequency that we should keep in mind is, for our case, the lowest since the magnetic measurements are usually performed at an angular speed of 1 Hz. For the single shaft (iso-perimetric transducer) the natural frequency is 1175.4 Hz for G11 and 797.35 Hz for Delrin. Both values are quite far away from the operation frequency of the transducer. Fig. 5.9, shows the effect of the lower eigenfrequency on the iso-perimetric coil shaft produced in G11.

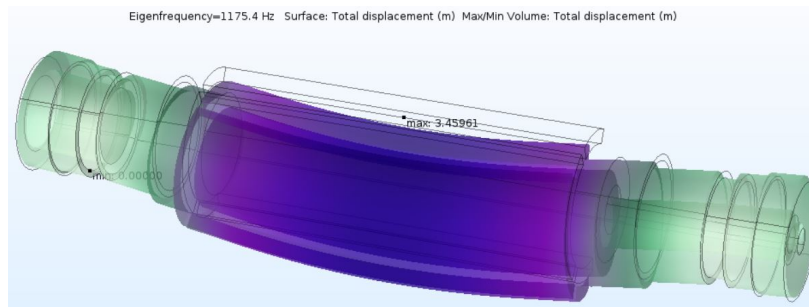


Fig. 5.9 Maximum total displacement of the single shaft in G11 subjected to the lower eigenfrequency.

In the case of complete assembly (see Fig. 5.8), natural frequencies take a more important role because, being a more complex structure with a greater number of elements, these could be much closer to the frequency of operation. In this case, the lower natural frequency is 138.39 Hz for G11 and 96.63 Hz for Delrin 100. It is clear that even in this configuration, the frequencies are higher than the operation one.

5.2.3 The measurement station

For the application of the iso-perimetric rotating coil transducer, a proper bench set-up was considered. To be able in performing a scan in the longitudinal direction of the magnet, the

Conceptual and engineering design of the rotating-coil transducer

proposed bench set-up must guarantee a positioning error less than $50\ \mu\text{m}$. It is important for a mapper to know with high accuracy the relative position between the magnet frame and the sensing element and to guarantee high accuracy in the transversal displacement.

The idea is to have a tubular support structure that has the biggest diameter as possible to cover at most the magnet aperture where the transducer can be installed. To perform the longitudinal scan, the tubular support is positioned by means a 3D mapper as shown in the concept design Fig. 5.10.

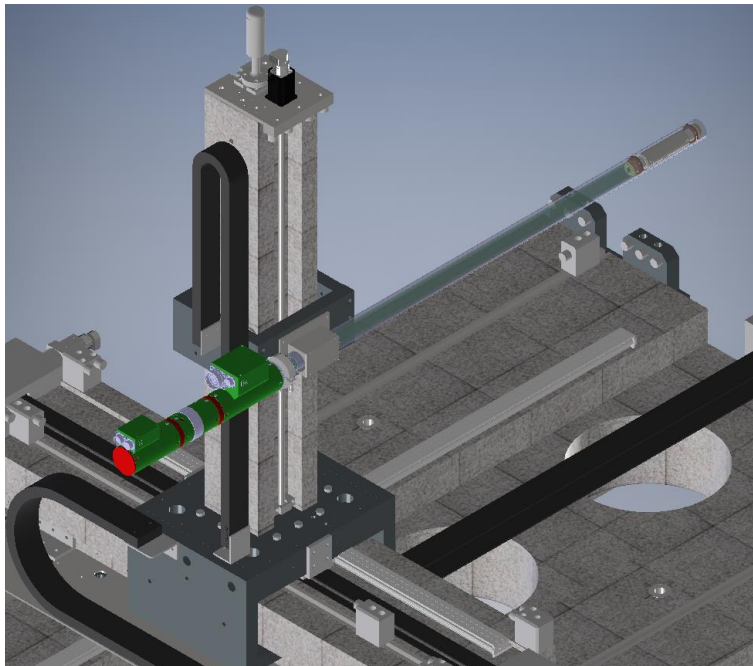


Fig. 5.10 Concept design of a 3D mapper for rotating coil scanner.

In Fig. 5.10 a sketch of a 3D mapper is shown. On the vertical arm of the mapper is installed a tubular structure containing the iso-perimetric transducers. To rotate the sensing rotating coil in the magnet bore, the bench system is equipped with the micro rotating unit connected to the tubular support wherein is installed the transducer.

5.3 Conclusions

In this chapter was presented the conceptual and engineering design of the rotating coil transducer. In particular, two different design were conceived for the first and for the second transducer prototype.

The first prototype was produced using a cylindrical shaft printed by 3D printing technology. The flexible sensor was then wrapped around the support. The measurement bench for proof of principle was designed to have two sliding linear stages where the support for the sensor was fixed. This set-up was conceived to perform the longitudinal scan in the magnet aperture.

The second prototype was produced using epoxy fiberglass G11 in order to increase the mechanical performance of the transducer. Three different transducers were designed for each single sensor (iso-perimetric, radial and tangential) in order to have the same measurement radius and length.

The conceptual design of a 3D mapper was presented at the end of the chapter.

Part III

Sensor and transducer production and calibration

Chapter 6

The sensor

The designed sensor presented in chapter 4.1, has to be produced considering the tolerances imposed by the sensitivity analysis presented in 4.4. In this chapter, we will focus on the production of the sensor, on the functional tests and on the calibration.

6.1 PCB production

Owing to the complexity of the geometry, three different manufacturing technologies were evaluated for the sensor production: 1) winding directly on a cylindrical mandrel, 2) sputtering deposition of conducting material on a cylindrical shaft, and 3) mounting a flexible printed circuit on a cylindrical shaft.

The first technique was excluded because of the required precision on the track positioning of $\pm 30 \mu\text{m}$. The second technique was excluded owing to the needed of having a multilayer circuit. The sputtering solution was considered too expensive and not suitable to build such a sensor. The flexible printed circuit technology guarantees high precision on the track positioning, a high reproducibility, and allows to stack multiple layers. An effort was required to produce the *Gerber* files for the printing process. In fact, the production needed some deviations from the ideal track positions. This is due to the required connections to form closed loops on one layer as well as the connections between the layers. Fig. 6.1 shows the connections in a two-layer PCB, only with two turns per layer for illustration purposes. The thin white line in the middle of the tracks indicates the ideal path according to the coil design. The thick yellow line shows the tracks on the first layer and the blue lines are the tracks in the second layer. On the connection side, the first turn (yellow) does not follow the complete ideal path but has a transition to the second turn that is one pitch shorter. On the inner track, the yellow line is again shorter by one pitch, because it is connected through the layer-jump to the second layer.

via. From Eq. 6.1 it is easy to understand that for short rotating coils, the effect of the via connections is much bigger than for long coils. The first term is the surface of the coil based on the designed geometry and the second term represent the "error" introduced by the needed electrical connections between each turn and between layers. The difference computed on the designed sensor is under 1 unit (10^{-4}). The PCBs for magnetometers must be designed with an even number of layers in order to reduce the differences between the ideal and actual surface due to the electrical connections.

The sensor's specifications are reported in Tab. 6.1.

	Unit	Main Coil	Compensation Coil
Length	mm	84.31	90.98
With	mm	56.68	11.83
N° Turns		236	44
Area	m ²	0.129	0.129

Table 6.1 Main sensor dimension.

As discussed in section 4.1, the sensor is composed of two coils, a main and a compensation coil, nested on the same PCB. The main coil is sensitive to the higher order field harmonics, while the compensation coil is sensitive mostly to the main field component, in order to compensate the main signal.

This is a powerful method to increase the signal-to-noise ratio and to compensate for a number of displacement errors arising from shaft vibrations. The 236 turns of the main coil and the 44 turns of the compensation coil are distributed on 4 layers (59 turns for the main coil and 11 for the compensation coil). Every layer is produced using film of *KAPTON AP7458E* with a copper layer on one side. The total thickness is 31 μm , with 6 μm copper and 25 μm *Kapton*.

In order to produce the tracks, a photoresistant film is placed in contact with the laminate and the circuit pattern (coming from the Gerber file) is transferred from the photomask to the laminate by applying UV light. The film is then removed chemically leaving the desired circuit pattern on the board. The next production step consists in generating the pattern on the copper layer. This is done by immersing the laminate in a chemical bath where the solution flows in the created pattern, abrading the copper that is not covered by the laminate. The layers are then stacked using pre-preg of 10 μm . The pre-preg has the function of insulating and bonding the layers. On each layer, it is then required to create the vias for the electrical

The sensor

connections between layers. The pads and vias are created using a CO_2 laser. Finally, the bottom and top sides are covered by *Kapton* layers.

During the production, tests are performed to qualify the production procedure. Some issues were found on the external tracks of the compensation coil because the tracks came out thinner than the main coil tracks owing to the larger gaps between them. A high quantity of corrosive acid was concentrated between the external coils reducing the width of the tracks. To avoid differences in the resistance of each loop and to prevent possible open circuits, the photo-resistant film *FX920* was replaced by *ALPHA930* to increase the precision on the track dimensions. Moreover, extra (open) tracks were added to limit the effect of excessive acid around the loop tracks. The open tracks are interrupted to limit eddy currents that could degrade the quality of the measurements. To guarantee mechanical resistance to the sensor and give more rigidity to the flexible board circuit, each layer was padded by copper points in the free areas, Fig. 6.3.



Fig. 6.3 Additional tracks on the compensation coil in order to avoid a concentration of acid during the edging process. Copper points were left on the substrate in order to increase the rigidity of the board.

This solution has been validated performing experimental tests for the absence of eddy currents. The absence of eddy currents was proved by measuring the harmonic contents of a reference magnet by adding, on the sensor, layers with the surface padded by copper points. The measurement results were all compatible. The Fig. 6.4, shows a picture of the first produced prototype and the main dimension of the sensor. In Fig. 6.5 instead, a magnification

of the sensor that shows the added tracks, the copper points and in particular the electrical connections (vias). Note that the minimum aperture angle on the first loop is limited by the size (diameter) of the vias. The minimum aperture angle limits, by construction, the maximum harmonic sensitivity of the sensor. For the designed coil, this does not represent a limit. In fact, the iso-perimetric coil has been designed reducing as much as possible the vias diameter and it presents a relatively high sensitivity factor until the 15th harmonic.

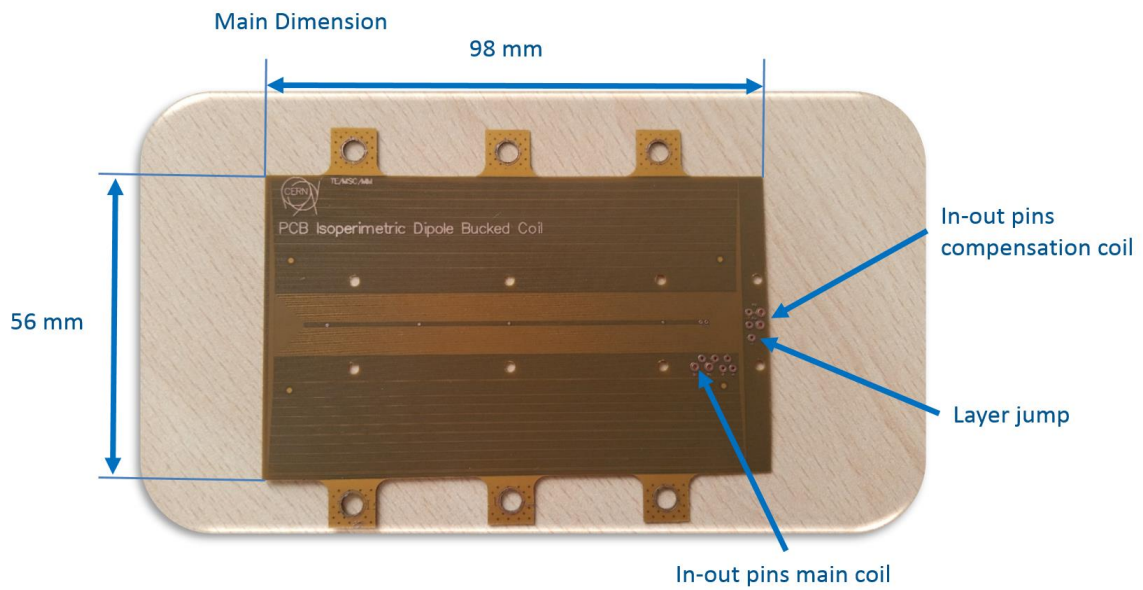


Fig. 6.4 First iso-perimetric sensor produced.

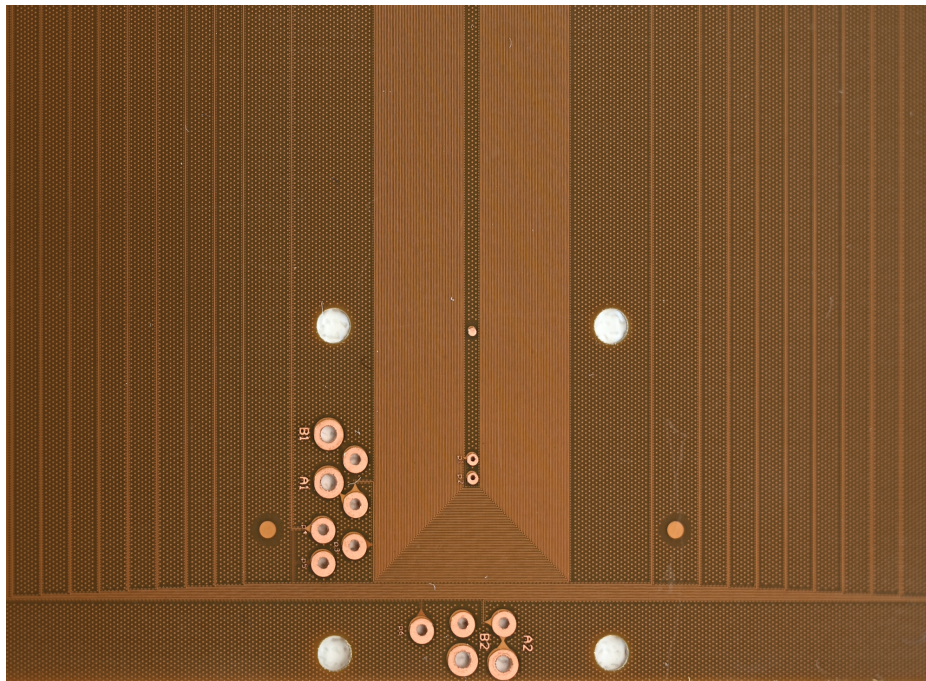


Fig. 6.5 Iso-perimetric coil sensor magnification on the connection side.

6.2 Mechanical metrological characterization

The sensor is to be installed on a cylindrical shaft where it can assume its saddle shape. At this stage, the position of each single track is crucial to guarantee the designed properties of the sensor. The uncertainty on the geometrical production tolerances was analyzed by considering errors in the production. The analysis yielded a maximum error in the track positions of $30 \mu\text{m}$. Considering the final configuration, the error on the radius positioning must not be larger than $\pm 200 \mu\text{m}$, chapter 4.4. This is the reason why particular attention was required during the sensor production controlling thickness and track positions. The track's position and the radius of the shaft are crucial for the sensor quality (sensitivity to the high harmonic orders and compensation of the main field component). Metrological mechanical measurements were performed at CERN in collaboration with the Materials&Metrology (EN/MME) section by using a Coordinate-Measuring Machine (CMM). In the final configuration of the transducer, the sensor mid plane must be at the designed radius with a tolerance of $\pm 200 \mu\text{m}$. Therefore, the final thickness of the *PCB* is a crucial input for the shaft production. Fig. 6.6 shows a picture of one sensor where in red is reported the measured thickness of the sensor no. 1 and in blue of the sensor no. 2.

6.2 Mechanical metrological characterization

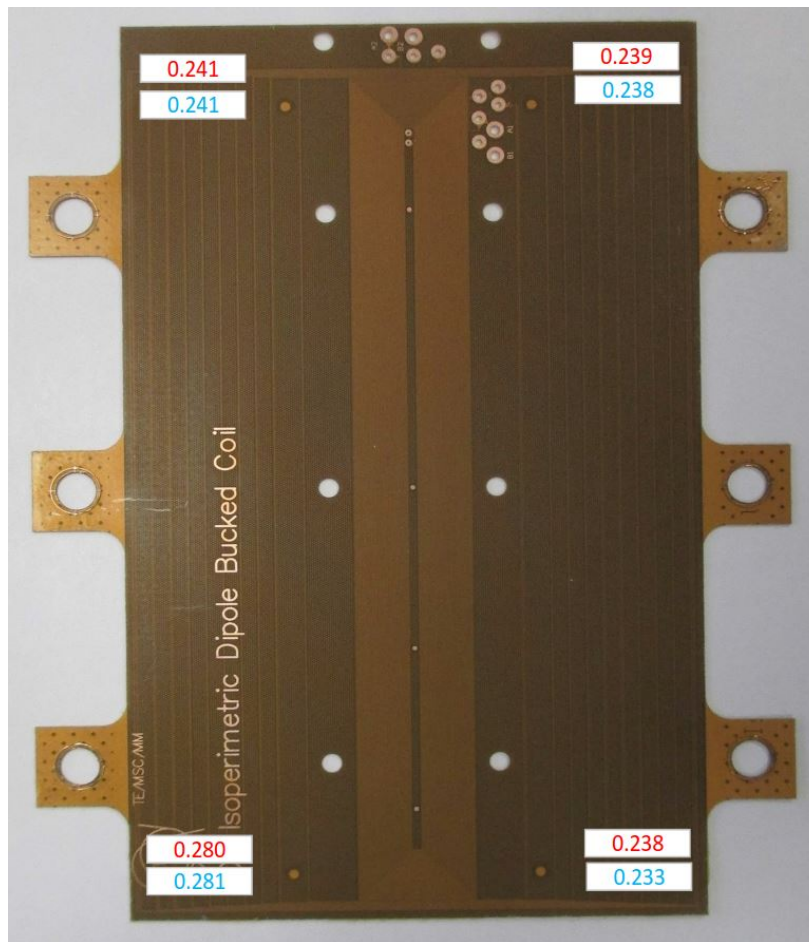


Fig. 6.6 Measured thickness of the sensor no. 1 (red) and sensor no. 2 (blue).

The measurements were performed at temperature of 20 °C and the estimated measurement uncertainty was $\pm 0.005 \mu\text{m}$. The Table 6.2 shows the results of the measurements.

PCB N° 1	PCB N° 2	Unit
0.241	0.241	μm
0.239	0.238	μm
0.280	0.281	μm
0.238	0.233	μm

Table 6.2 Thickness of the two produced sensors.

Another important parameter for the production quality assessment is the position of the tracks and its comparison with its designed value. This test is particularly important for the

The sensor

external tracks. In fact, errors bigger than $\pm 30 \mu\text{m}$ on the position of the inner coil tracks would produce short circuits, owing to the small size of the insulation thickness, yielding impossible to use the sensor. On the other hand, errors on the external tracks, with larger insulation thickness will modify the sensitivity of the coil. Knowing the measured position of the tracks, the sensitivity functions were computed and compared with the ideal geometry. For an iso-perimetric coil, the sensitivity to the transversal field harmonics must be expressed as a function of its axial length and computed for every single loop. This is because this sensor can be considered as the connection in series of many tangential coils with different length and different opening angle for which the sensitivity function must be computed separately. In Figs. 6.7 and 6.8, the nominal tracks positions and the measured relative deviations are plotted for the sensor no. 1 and no. 2, respectively.

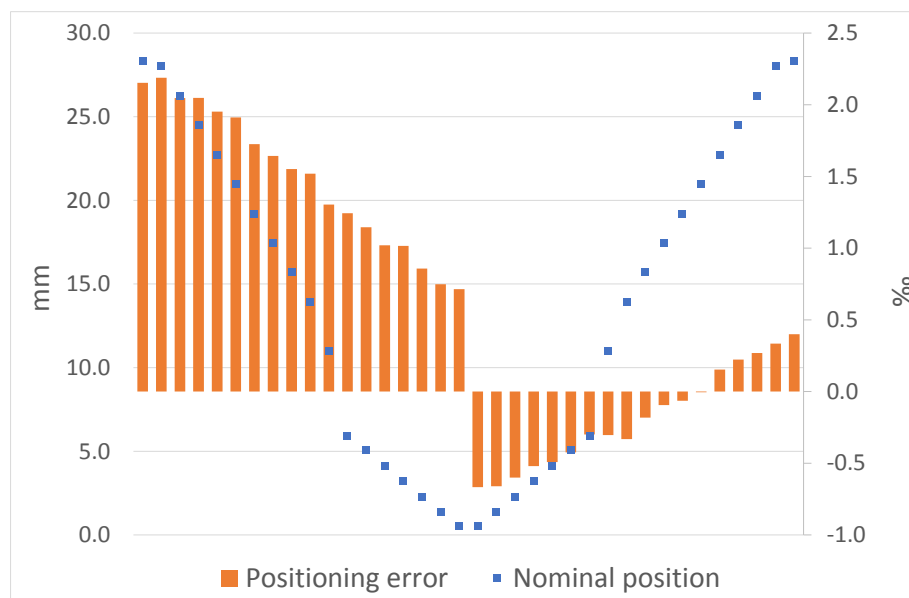


Fig. 6.7 Nominal track position (blue dots) and error (orange bars) for FCB no. 1.

6.2 Mechanical metrological characterization

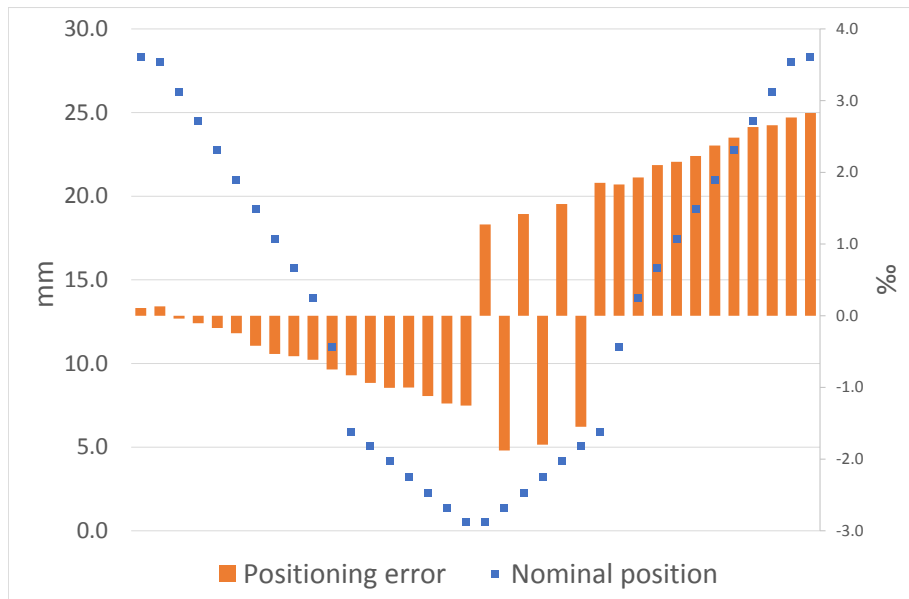


Fig. 6.8 Nominal track position (blue dots) and error (orange bars) for FCB no. 2.

The error bars show a maximum displacement of the track of 3 per-thousand on the serial number no. 2. It means a difference of $80 \mu\text{m}$ from the designed position of the external tracks (compensation coil). For the main coil, all the tracks are in the range of $\pm 10 \mu\text{m}$. The results, furthermore, show a displacement of the all tracks in one direction on both the sensors. It is due to an error on the positioning of the mid-point or a systematic error during the production.

The measured values were then used to compute the sensitivity factor and make a comparison with the theoretical results. In Fig. 6.9 the sensitivity factor analysis is shown. In particular Fig. 6.10 shows the percentage error until the 15th sensitivity factor due to the tracks position errors.

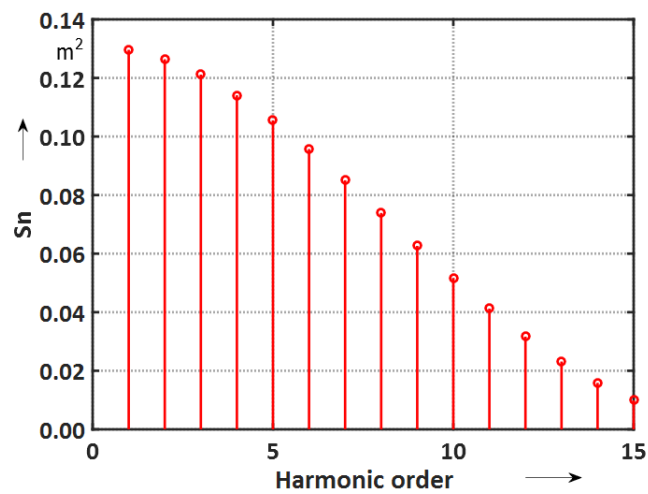


Fig. 6.9 Sensitivity factor main coil from design.

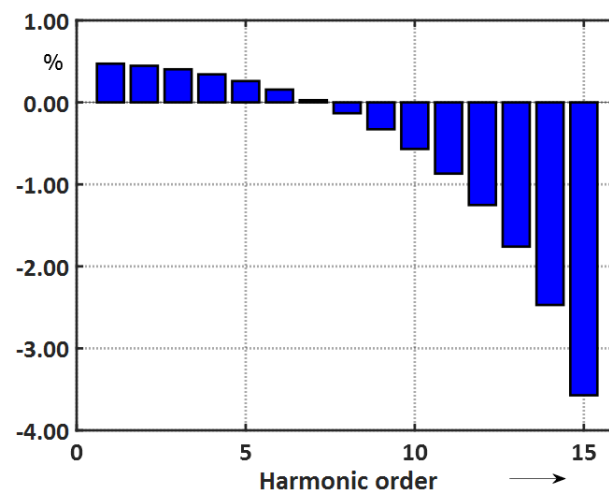


Fig. 6.10 Percentage error on the sensitivity factors due to the positioning errors on the tracks.

The PCB production error has a significant effect on the sensitivity factors of the sensor (almost 50 units for S_1) but, since the sensor must be calibrated, it does not represent a limit for the quality of the measurements. Instead, it could represent a limit for the bucking of the sensor.

6.3 Functional tests and calibration

For the functional tests, the electrical continuity was verified and the resistance of the four layers connected in series was measured. The measured coil resistance was equal to 3727Ω and 969Ω for the main and the compensated coil, respectively. The measured resistance does not allow to identify a short circuit between two or more close tracks. Moreover, a theoretical resistance value cannot be calculated because its value is strongly correlated to the thickness of each track. For this reason, a functional test was performed following the procedure adopted for the calibration of a standard coil. The sensor was inserted in a reference dipole with a spatial uniformity of the magnetic flux density of $10 \mu\text{T}$. The electromotive force induced on it by a rotation of π was measured. The transducer prototype, moreover, must be calibrated in order to verify, from the magnetic point of view, the main important parameters like area and measurement radius.

The transducer was calibrated in the reference dipole in flat and curved configuration. In the flat configuration, the sensor was positioned perpendicularly to the magnetic field lines. Practically, the sensor was sandwiched between two flat plates and the equivalent surface was measured. Thanks to this calibration, possible short circuits were detected by checking the difference between the ideal and actual area taking into account the errors on the tracks positions. The final configuration of the sensor requires to bend the flexible circuit on a cylindrical shaft, therefore a calibration was performed in the curved configuration by placing the sensor on a cylindrical mandrel. The purpose of this calibration was to verify the sensitivity to the main field component and to check possible failures during the bending process.

The following Table 6.3, shows the calibrated area versus the design area, in both configurations and both coils. Furthermore, the compensation ratio, defined as ratio between the compensation and main coil surface, is illustrated.

	Flat			Curved		
	Main Coil (m ²)	Comp. Coil (m ²)	Comp.Ratio	Main Coil (m ²)	Comp. Coil (m ²)	Comp.Ratio
Design	0.13069	0.16295	4.0	0.12960	0.12981	636.3
Calibrated	0.12933	0.16599	3.5	0.12855	0.13323	27.5

Table 6.3 Dipole calibration results for the iso-perimetric coil.

In the curved configuration, the measured compensation ratio results to be much smaller than its theoretical value owing to the huge difference in the compensation coil area. In chapter 4.4, different sources of uncertainty on the compensation ratio of the sensor have

The sensor

been analyzed. The compensation ratio can be affected by the track positioning and by the shaft radius. In the curved configuration (sensor attached on the shaft) the source of error cannot be identified by calibration. To sunder the two contributions, the surface that the sensor should have in the ideal curved configuration can be estimated from the calibration in the flat configuration. This value, compared with the design area will give information about the effect of the turn positioning errors. Then, the comparison of this value with the calibration performed in the curved configuration allows to estimate the effect of the shaft tolerances. Tab. 6.4 shows the ideal design area (D), the curved configuration area estimated from the flat configuration calibration (E), the curved calibrated area (C), and the corresponding percentage differences, for the main and compensation coil.

	(D) Design (m ²)	(E) Estimated (m ²)	(C) Calibrated (m ²)	Error D-E %	Error D-C %
Main	0.12960	0.12825	0.12855	1.04	0.81
Compensation	0.12981	0.13223	0.13323	-1.86	-2.63

Table 6.4 Ideal design area (D), curved configuration area estimated from the flat configuration calibration (E), curved calibrated area (C), and the corresponding percentage differences, for the main and compensation coil.

In Table 6.4, is possible to notice that the compensation coil has been affected more from the dimensional tolerance of the shaft than the turns positioning error. The compensation coil results to have a bigger surface than the designed value and this is because the shaft radius is bigger than the radius by design. Regarding the main coil, the estimated surface from the flat configuration calibration is smaller than the calibrated surface. In the final configuration, the main coil has a difference in percentage of 0.81% from the designed value and the compensation coil has a difference of 2.63%.

The dimensional errors on the track positions and on the shaft radius give the same percentage of error in the spanned surface after the mounting. As the track positions cannot be modified or shimmed, the mechanical tolerance of the radius shaft became crucial. It was fixed to 20 μm .

The radial, PCB coil in Fig. 6.11, was installed in the first prototype transducers. The calibration results are summarized in Tab. 6.5.

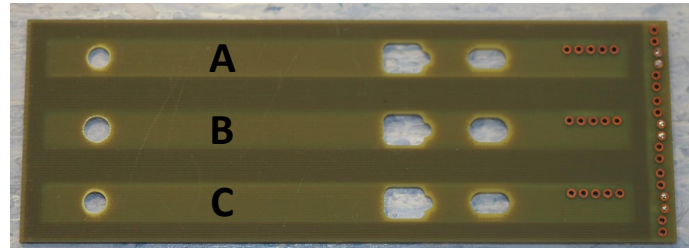


Fig. 6.11 Radial coil installed in the first prototype transducer.

Coil	Unit	A	B	C
Resistance	Ohm	270	269	269
Surface	m ²	0.08809	0.08808	0.08809

Table 6.5 Dipole calibration results for the radial PCB coil installed in the first prototype.

The production of the second transducer prototype, based on the iso-perimetric sensor and on the new designed radial and tangential coils, requires the same validation tests and calibration.

The sensors for the second prototype (radial and tangential coil sensor) have the same measuring radius, length and approximately the same surface of the FPC. Following the same procedure adopted for the previous iso-perimetric coil, the second iso-perimetric coil was calibrated. In Tab. 6.6, the calibration of the second iso-perimetric sensor.

	Flat		Curved	
	Main Coil	Comp. Coil	Main Coil	Comp. Coil
Design (m ²)	0.13069	0.16295	0.12960	0.12981
Calibrated (m ²)	0,12933	0,16601	0.12833	0.12980

Table 6.6 Dipole calibration results for the iso-perimetric sensor (second prototype) in both configuration.

In Tab. 6.7 is shown the calibration of the designed radial coil no. 2. Two PCBs were produced, but since the no. 1 had one coil (coil C) with an open circuit, only the serial number no. 2 was calibrated.

The sensor

Coil	Unit	A	B	C
Resistance	Ohm	388	387	388
Surface	m ²	0,10084	0,10079	0,10080

Table 6.7 Dipole calibration results of the radial PCB coil no. 2 (second prototype).

Finally, in Tab. 6.8, the calibration of the single PCBs for the assembly of the tangential coil transducer.

N° Coil	Unit	1	2	3	4	5	6	7
Resistance	Ohm	389	389	385	386	387	386	388
Surface	m ²	0.10076	0.10088	0.10085	0.10073	0.10082	0.10089	0.10078

Table 6.8 Dipole calibration results of the tangential PCBs coils.

All the calibrations have been performed at the reference magnetic flux density of $0,99914 \pm 0.00002$ T.

6.4 Conclusions

In this chapter, the production, the functional tests and the calibration of the coil sensors was discussed.

In particular, the iso-perimetric coil production was described in detail focusing on the Gerber file design and on the production process.

The mechanical metrological characterization of the produced FPCs was shown focusing on the difference between the design and the actual sensitivity factors.

Furthermore, the functional tests and the calibration of the iso-perimetric, radial and tangential coils were described.

Chapter 7

The transducer

The transducer production and calibration will be presented in the following sections. In particular, in 7.1, the production of the two prototypes of iso-perimetric coil transducer is presented. The materials and the technical specifications of the assembly will be described. In 7.2, the dipolar and the quadrupolar calibration are presented.

The requirements for the developed transducer are the ability to be no-sensitive for the z-field component and to measure the local field distribution along the all magnet length including the fringe field. The sensor must be as short as possible to reduce the convolution along the longitudinal direction, have high sensitivity for high harmonic orders, able to accommodate different sensing coils, easy to displace in the magnet bore and have the possibility to measure the relative position in the magnet bore with a precision of $\pm 50 \mu\text{m}$.

The design of the transducer is driven by many aspects that are: the sensor design, manufacturing precision, the compact size of the all components and the innovative way of the sensitivity factors computation.

Regarding the sensor design and the sensitivity factor calculation, we have already reported in 4 and in 1.1.

The rotating coil is a robust tool for measuring the harmonic field components, nevertheless it is extremely important to have good mechanical precision on all the components. The precision is required to guarantee: a unique and stable rotation axis, a well-positioned coil on the shaft to obtain the desired bucking ratio and a stable positioning in the transversal position while the sensor is rotating. All these requirements need to be taken in to account for the production of a reliable transducer, able to provide information regarding the field quality with relatively low uncertainty.

Regarding the size of the all transducers, in general, would be favourable to have as small as possible transducer in order to be less invasive and to not modify the measurand. In case of rotating coil transducer for magnetic measurements, compact size of the measuring system

The transducer

are required to be able in measuring the harmonics content at the biggest radius as possible, where the high order harmonics have the highest value (remember the exponential behaviour of the harmonics).

Regarding the calibration, the sensitivity of rotating search coils depends on the shaft design (radial coil intercepting the azimuthal flux, tangential coil intercepting the radial flux), the coil radius, numbers of turns, and spanned surface. The main source of error in fluxmeters is the uncertainty on the sensitivity of the coil to the measured field. It is obvious that production tolerances or errors during the production can introduce deviation from the ideal design. A solution to this problem is the calibration in a reference field given by a reference magnet that is for example mapped by NMR. In this way the surface of the coil can be calibrated. Often is necessary to measure the orientation of the midplane of the coil respect to the mechanical midplane. Furthermore, coils are used to measure gradient field and they must be calibrated in a well-known gradient field. Fluxmeter coils can be calibrated with typical accuracy from 10 to 100 ppm.

For a dipole magnet, the main calibration parameter to measure the integral of the field over the magnet length is the magnetic equivalent area. For a quadrupole magnet, the magnetic equivalent average rotation radius of the coil must be calibrated for measuring the gradient field.

Usually for designing, the average position of the coil is considered. In the case of the isoperimetric coil, it is not possible to consider the average position. To compute the equivalent area would need mechanical measurements, such as x ray or optical scans, to know the 3D coordinates of every single turn. Far better results are achieved by calibration in a reference dipole field (stable and uniform). Apart from the equivalent surface of the coil is important to know the rotational radius. In fact, errors on the rotational axis can affect the measurements giving errors on the harmonics that are exponential with their order. The rotational radius can be calibrated in a well known gradient field, such as a quadrupole. For a full calibration, two calibration magnets are needed (reference dipole and reference quadrupole).

7.1 Production

The first prototype for the proof of principle was realized by using the 3D printer for rapid prototyping. The cylindrical shaft was made in ACCURA 25. The material, pure resin, is characterized by tensile E modulus 2200 ± 100 MPa, tensile strength 45 ± 2 MPa and glass transition temperature 60 °C. The material was chosen for obtain the first prototype as quickly as possible. Typical tolerances for ACCURA 25 on dimensions of 30 mm are 0.15 -

0.2 mm.

The shaft was then supported by two ceramic ball bearings assembled with rollers produced in ACCURA 4 *HTR* (the rollers are used to translate the transducer inside the support tube). The purpose of the transducer built for the proof of principle was to demonstrate the difference between two different typologies of sensors (radial induction coil and an iso-perimetric induction coil). To guarantee the iso-perimetric geometry of the developed sensor, the sensor was installed on a round shape shaft having the "desired" diameter. To guarantee the repeatability of the measurements, the radial coil was installed in the same shaft (that is, on the same transducer) having the measuring radius smaller than the iso-perimetric coil. The transducer was then furnished by two Hall probes, one on the center coil (on the top of the radial coil) and the second one on the outer radius of the cylinder. The Hall probes were used to have point like measurements and to validate the application of rotating Hall probes. In Fig. 7.1, is possible to see the radial induction coil and the Hall probe installed in the middle of the shaft. In Fig. 7.2, the flexible circuit board is wrapped around the external diameter of the shaft.

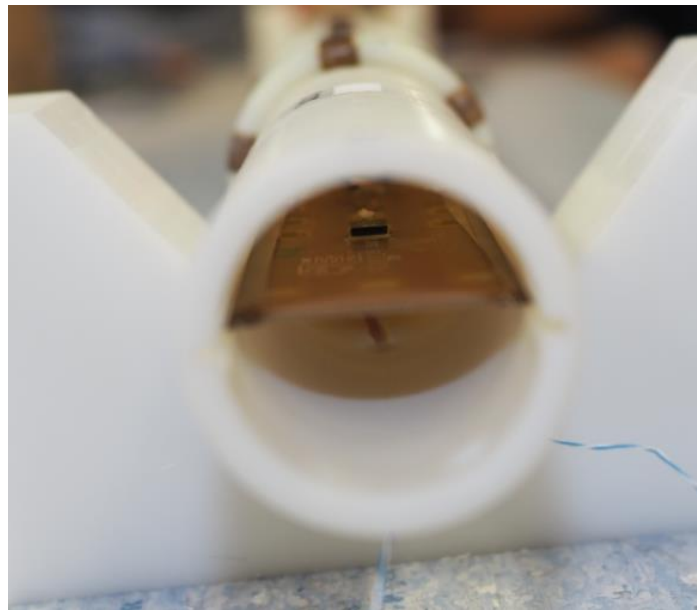


Fig. 7.1 Assembly view, radial coil and Hall probe inside the cylindrical shaft.

The transducer



Fig. 7.2 Assembly of the iso-perimetric coil wrapped around the external diameter of the shaft.

Due to the mechanical tolerances of the prototype, the results in term of shaft diameter (and therefore also in term of bucking ratio) was not satisfactory, in fact the shaft diameter was almost 1 mm bigger than the desired diameter. Nevertheless, the prototype was able to show what we expected from the preliminary tests.

From the experience on the first assembly, a second design was conceived using materials with higher mechanical characteristics.

The second prototype was designed to be produced using the *Glass/Epoxy Resin G11* with proper mechanical characteristics for the production of the assembly shown in A.2. The shaft radius was designed with an external diameter of 37.89 ± 0.02 mm and an eccentricity below 0.05 mm. The material, pure resin, is characterized by tensile E modulus 25000 ± 100 MPa, tensile strength 370 ± 10 MPa temperature index (TI) 155. Fig. 7.3, shows the shaft assembly of the iso-perimetric coil.



Fig. 7.3 Assembly of the iso-perimetric coil on the cylindrical shaft made in *G11*.

Fig. 7.4, shows the assembly of the radial coil shaft produced in *G11*. The small coil in the figure represents the tangential coil that will be used to assemble the tangential coil transducer.

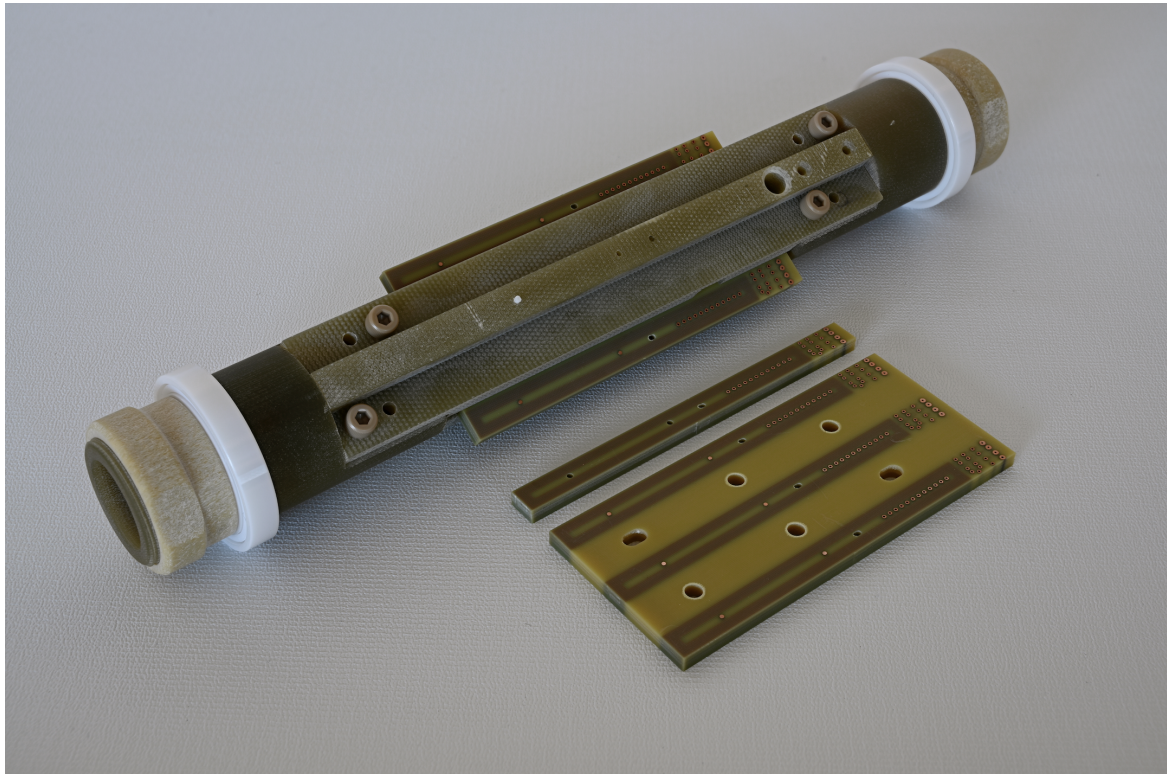


Fig. 7.4 Assembly of the radial coil transducer in G11.

7.2 Calibration

The transducer calibration was required to compute: the effective area of the sensor in its final configuration, the achieved bucking ratio and the measurement radius both radial and iso-perimetric coils, for both prototypes. Moreover, the calibration of the Hall probes was performed comparing the harmonic content measured by the radial coils (after the calibration) with the Hall probes.

7.2.1 Dipole calibration

The dipole calibration was performed in a reference dipole with magnetic flux-density uniformity of $1 \cdot 10^{-5}$ T. From the calibration data of the iso-perimetric coil are presented in 6.3. It is possible to notice that the compensation coil surface is strongly affected by the dimensional tolerance of the shaft. The compensation coil has larger surface than designed. This is due to the fact that the shaft radius is larger than the design value. In the second shaft

prototype an improvement of almost three times is achieved.

In Section 6.3 the results of the calibration are given; Tab. 6.3 give the results for the iso-perimetric coil used in the first prototype and Tab. 6.5 the results for the radial PCB coil. For the second transducer prototype, Tab. 6.6 gives the calibration results of the iso-perimetric coil, Tab. 6.7 the calibration results of the radial coil and Tab. 6.8 the calibration results of the tangential coil.

Performing the transducer calibration in the dipole, the coil surfaces are measured as well as the differences between the surfaces of the coils on the same transducer. Moreover, the parallelism between the coils is calibrated.

For all the transducers, excluding the iso-perimetric, the maximum deviation in the coils surface is 0.01%, while the maximum error for the parallelism is -5.0 mrad on the external coil (A) of the tangential coil transducer.

The calibration results are used to compute the sensitivity factors of the transducers.

7.2.2 Quadrupole calibration

The calibration in a quadrupolar magnetic field was performed using the standard calibration procedure. The described procedure, adopted for the first prototype, is valid in general for any transducers. The section view of the first transducer is composed of three radial coils and two iso-perimetric coils.

For the calibration, the radial coils are aligned in the quadrupole to measure the maximum flux. The alignment is performed by ramping the magnet while measuring the integrated voltage induced in the coils. After having aligned the coils, the gradient is measured by using the central coil (B) of the radial coil on the PCB in Fig. 6.11. It is possible to measure the gradient using only one of the coils because we assume a constant gradient. This is for sure the case in the calibration magnet. The gradient is measured displacing the coil on the plane for a precise amount, measured by two LVDTs, while the magnetic flux is measured by an integrator. Knowing the calibrated surface, measuring the flux and the displacement, is possible to compute the gradient.

To calibrate the measuring radius of the coils, the shaft is positioned in the center of the quadrupole aperture and the coils are turned, for certain angles, in order to measure the flux. For the radial PCB coil installed in the first prototype the results of the calibration are:

The transducer

	Surface (m ²)	Radius (mm)
A	0.08809	11.36
B	0.08808	0.01
C	0.08809	11.37

Table 7.1 Quadrupole calibration for the radial PCB coil of the first prototype.

The measured gradient by using the central PCB is 8.8535 T/m.

To calibrate the iso-perimetric coil was used the gradient measured by the radial coil in the magnet center. The calibration procedure adopted for those coils was exactly the same of the described procedure for the radial coil. The calibrated radius is given in Tab. 7.2.

For tangential and radial coils, the measuring radius is given by the geometrical mean position of the coils. This is true because is possible to assume that all the turns have the same surface and that they are concentrated in the average position of the coil. This is not valid for the iso-perimetric coil, where the section view is characterized by coils spread along the shaft circumference. This yield to find a valid metric to compute the theoretical measuring radius and compare it with the calibration results.

The measuring radius of a tangential coil is defined as the imaginary part of the vector position in the complex plane of the coil mean width. The iso-perimetric coil can be approximated as an array of many tangential coils connected in series and located at different radii. To define the best way to compute the measuring radius of the iso-perimetric coil, three procedure have been evaluated.

The first is an average radius weighed with the turn surface,

$$r = \frac{Im(Z_m) \cdot S_m^1 + Im(Z_{m+1}) \cdot S_{m+1}^1 + \dots}{K_1}. \quad (7.1)$$

The second way is tho weigh the radius on the second sensitivity order on the coil (k_2),

$$r = \frac{Im(Z_m) \cdot S_m^2 + Im(Z_{m+1}) \cdot S_{m+1}^2 + \dots}{K_2}. \quad (7.2)$$

The third is to calculate a normal average of the different radii,

$$r = \frac{\sum_{m=1}^M Im(Z_m)}{M}, \quad (7.3)$$

where Im represents the imaginary part of the vector position in the complex plane Z_m . In Tab. 7.2, are shown the results of the calibration and the radius computation by applying

the three defined procedures considering the theoretical radius of the sensor (19.065 mm measured from the shaft axis to the average thickness of the flexible board circuit).

	Surface (m ²)	Radius (mm)	Theor dip 1 (mm)	Error (mm)	Theor quad 2 (mm)	Error (mm)	Theor Avr 3 (mm)	Error (mm)
Main	0.12856	19.584	18.590	-0.994	18.594	-0.989	18.728	-0.855
Compensation	0.13322	9.135	7.688	-1.447	10.414	1.279	8.474	-0.661

Table 7.2 Results of the quadrupole calibration for the iso-perimetric coil.

In Tab. 7.2, an error of approximately 1 mm is shown for all the proposed metrics. At this stage, it is not possible to define the right metric for the theoretical computation of the measuring radius. However, the difference of +1 mm is coherent with the real dimension of the shaft. In fact, considering the flexible circuit board thickness (0.240 mm) and the desired mean radius of the sensor (19.065 mm), the theoretical shaft radius must be 18.945 mm. The measured radius of the shaft is, instead, 20.130 mm. It means that the sensor mean radius is 20.250 mm instead of 19.065 mm, being, therefore, 1.185 mm bigger.

To define the right way, to compute the measuring radius of an iso-perimetric coil, a reverse engineering study has been performed. Since the shaft radius is known as well as the calibration radius, is possible to calculate the three defined radii using as theoretical radius 20.250 mm. Analyzing the results in Tab. 7.3 is possible to conclude that the right way to compute the theoretical measuring radius is using the Eq. 7.1. It becomes clear looking at the errors on the compensation coil more than the main coil. This is true because the compensation coil is more affected by radius errors.

	Radius (mm)	Theor dip (mm)	Error (mm)	Theor quad (mm)	Error (mm)	Theor Avg (mm)	Error (mm)
Main	19.584	19.802	-0.218	19.805	-0.221	19.933	-0.349
Compensation	9.135	9.307	-0.172	11.415	-2.28	10.127	-0.992

Table 7.3 Theoretical radii of the iso-perimetric coil from the reverse engineering study.

To verify the quality of reference quadrupole magnetic field, the gradient and consequently the iso-perimetric coils radii were measured/calibrated using as reference the main iso-perimetric coil. The main coil is positioned (by the nature of the transducer) in the aperture of the magnet at the coordinates 0 mm in x and approximately 9.5 mm on y . The measured gradient was 8.8525 T/m, that is 0.11 per-thousand smaller than the gradient measured by the central radial coil. According to the calibration performed using the main iso-perimetric coil as a reference, the theoretical measuring radius of the two iso-perimetric coils are shown in Tab. 7.4, where the error represents the difference between the previous calibration (using

The transducer

the gradient measured by the PCB coil) and the calibration performed using the gradient measured by the iso-perimetric main coil.

	Radius (mm)	Error (%)
Main	19.602	0.09
Compensation	9.145	0.10

Table 7.4 Difference in term of radius measuring the gradient with the iso-perimetric coil.

In conclusion, the assumption of a constant gradient in the magnet aperture is correct since the calibrated radius, using the two different procedure, are compatible.

The second prototype of the iso-perimetric coil was conceived having three different shafts for each sensor typology (iso-perimetric, radial, and tangential coil). The calibration procedure for the iso-perimetric coil transducer is the same adopted for the first prototype where the quadrupole gradient was measured by using the main coil. The results for the iso-perimetric coil transducer, second prototype, are reported in the following Tab. 7.5

	Surface (m ²)	Radius (mm)	Theor rad (mm)	Radius error (mm)	Design surf (m ²)	Surf error (%)
Main	0.12833	18.485	18.590	0.105	0.12960	-0.98
Compensation	0.12980	7.736	7.688	-0.048	0.12981	0.00

Table 7.5 Results of the dipole and quadrupole calibration for the second prototype of the iso-perimetric coil transducer.

The calibration results for the radial coil transducer of Fig. 7.4 are reported in Tab. 7.6

	Surface (m ²)	Radius (mm)	Theor rad (mm)	Radius error (mm)	Design surf (m ²)	Surf error (%)
A	0.10078	18.880	19.065	0.184	0.10000	0.78
B	0.10076	0.130	0	-0.130	0.10000	0.76
C	0.10076	-19.150	-19.065	-0.085	0.10000	0.76

Table 7.6 Results of the dipole and quadrupole calibration for the second prototype of the iso-perimetric coil transducer.

The calibration results for the tangential coil transducer are reported in Tab. 7.7

	Surface (m ²)	Radius (mm)	Theor rad (mm)	Radius error (mm)	Design surf (m ²)	Surf error (%)
A	0.10081	-19.203	-19.065	0.138	0.10000	0.81
B	0.10079	0.026	0	0.026	0.10000	0.79
C	0.10083	19.278	19.065	0.213	0.10000	0.83

Table 7.7 Results of the dipole and quadrupole calibration of the tangential coil transducer.

7.3 Conclusions

The transducers production and calibration were presented in this chapter.

In particular, the production of the two prototypes of an iso-perimetric coil transducer was shown focusing on the mechanical characteristics of the shafts. Moreover, the materials and the technical specifications of the assembly were described.

In the second part of this chapter, the calibration procedure and the calibration results for the iso-perimetric, the radial, and tangential coils were presented.

It was demonstrated that for the quadrupole calibration (i.e., radius calibration) of the iso-perimetric coil transducer it is possible to use the main sensing coil for measuring the quadrupole gradient. This is possible due to the gradient uniformity in a reference quadrupole.

Part IV

Experimental Results

Chapter 8

Validation and field measurements

After the calibration procedure, the first experimental measurements were performed in the reference dipole where the harmonic content of the magnet is well known. This is the best and easiest way to validate the transducer end to ensure that it does not introduce spurious harmonics. Another important information is the computation of the bucking ratio and the standard deviation on the harmonics. The standard deviation is computed performing n -revolutions at the same position. Furthermore, some measurements on the edge of the magnet were performed to check the behaviour of the bucking ratio.

The transducer was, moreover, used to perform two measurements on field.

The first application of the iso-perimetric coil transducer was to measure the magnetic field profile of a bending corrector dipole having a solid iron yoke.

The second application was to measure the behaviour of the fringe field in the superconductor Canted-Cosine-Theta (CCT) dipole for the Hi-Lumi upgrade.

8.1 Transducer measurement validation in reference dipole

The measurements carried out in the reference dipole no. 2, in the center of the aperture, were performed using the layout shown in Fig. 5.4. The transducer is positioned in the magnet center where the harmonic content is well known thanks to different measurements performed with different transducers.

The bucking ratio of the two transducers (first and second prototype of iso-perimetric coil transducer) were computed averaging the measurements result on 20-turns in the same position. For the first prototype, the bucking ratio is 20 and for the second prototype is 50. As expected from the calibration on both transducers, the bucking ratio is not comparable with the bucking ratio of traditional rotating coil (100 - 3000). This is due to the complexity

Validation and field measurements

of the sensor and to the production tolerances of the sensor and of the transducer. A possible solution to increase the bucking ratio is to acquire main and compensation coil separately and then apply the so-called digital bucking. In Fig. 8.1a and 8.1b, is possible to see the harmonic content measured by the iso-perimetric coil.

The result is in accordance with the measurements performed at the same current and at the same radius with different sensors. Fig. 8.2a shows the harmonic content measured by the iso-perimetric coil and Fig. 8.2b by the radial coil. Furthermore, the standard deviation on 20-revolutions computed on the bucked signal is approximately 0.02 units (main field, B_1 , 0.9867 T) against the 0.2 units from the absolute signal. These results confirmed the measurement performances of the sensor in term of repeatability and accuracy. In absolute, this is a good result and it is compatible with the standard deviation obtained by using traditional sensors installed on the same typology of shaft (rotating coil assembled with plastic rollers inserted in the stainless steel tube for mechanical support).

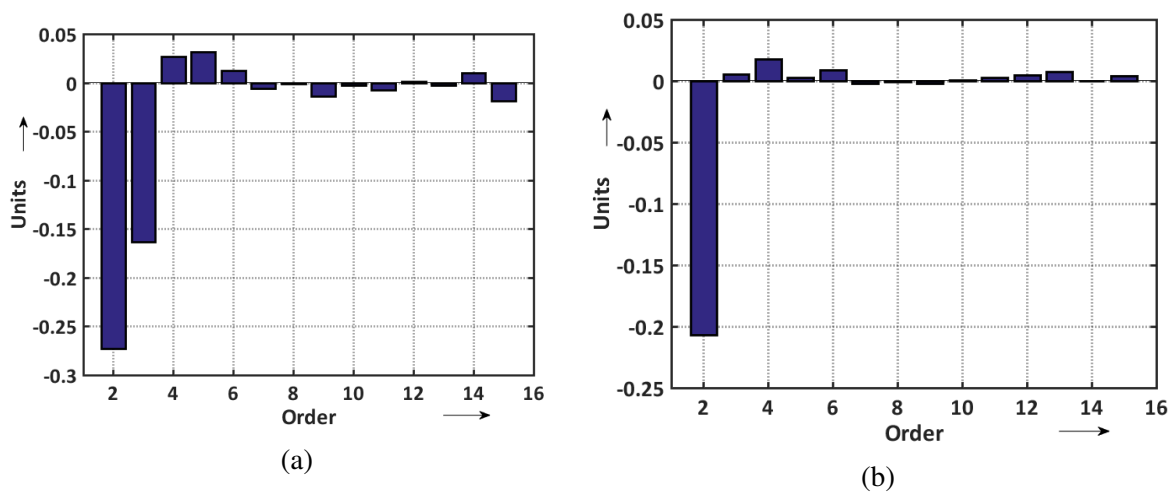


Fig. 8.1 Normal field components (a) and skew field components (b) expressed in units measured in the reference dipole no. 2 at 316 A by the iso-perimetric coil transducer.

8.1 Transducer measurement validation in reference dipole

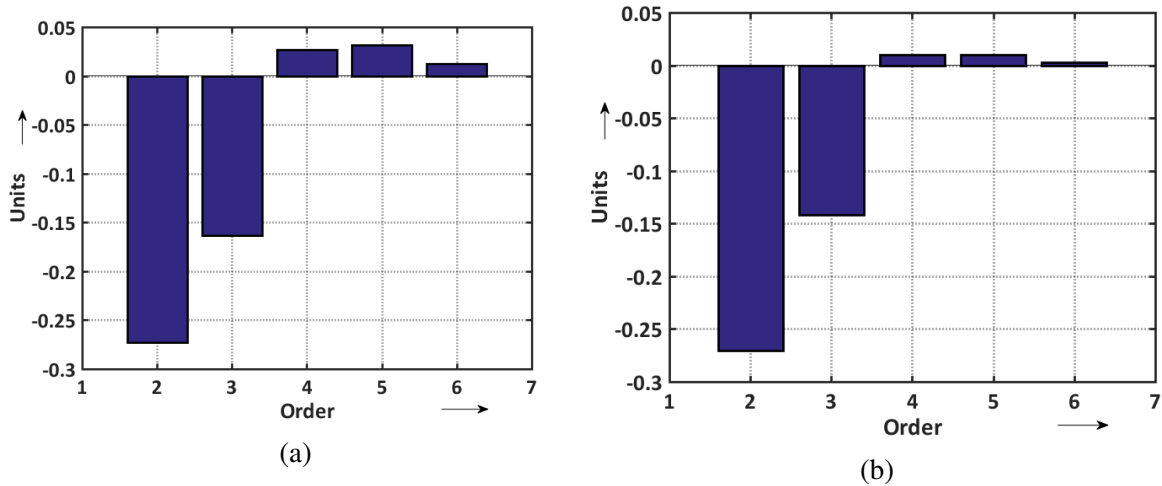


Fig. 8.2 Harmonic content in units ($B_2 - B_6$) measured by iso-perimetric coil (a) and radial coil (b).

The second campaign of measurements was performed using the second prototype of the iso-perimetric coil, the radial, and the tangential coil presented at the end of Section 7.1. In particular, measurements were performed in the magnet center and at the edge of the magnet pole. Afterwards, a metallic bar was installed close to the transducers in order to introduce higher-order field errors and analyze their effects on the three transducers. The measured compensation ratio in the magnet center without the bar is 50, 350, and 150 for the iso-perimetric, radial and tangential coils. At the magnet pole, the compensation ratio worsens substantially for radial and tangential coils (43, 30) but is much less affected for the iso-perimetric coil (35). The compensation ratio has a direct effect on the standard deviation computed from the 80 repetition of the measurement at the same position. The following graphs show the average harmonics and the standard deviation in units. Fig. 8.3 shows the standard deviation at the magnet center, the highest standard deviation is on the iso-perimetric coil for his low compensation ratio. Radial and tangential coils have approximately the same standard deviation. (Must be clarified that generally, the accuracy on the harmonics is about ± 1 unit. For this reason, these graphs are indicating only the tendency).

Validation and field measurements

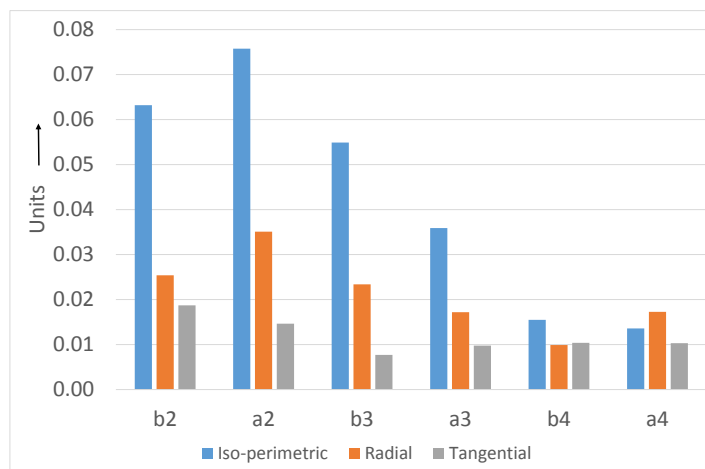
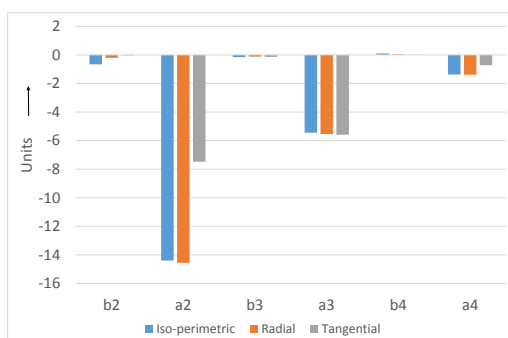
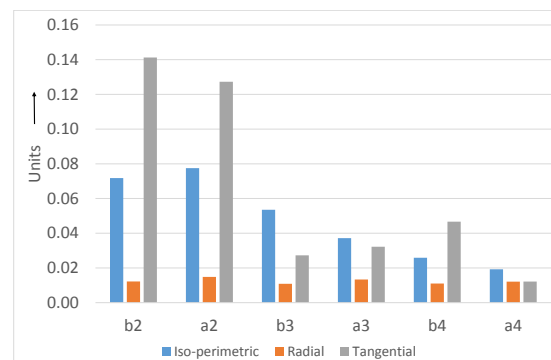


Fig. 8.3 Standard deviation in units for the harmonic content in the reference dipole center measured by the iso-perimetric, radial, and tangential coil.

In Fig. 8.4a and Fig. 8.4b the measurement results in the magnet center with distortion are shown.



(a)



(b)

Fig. 8.4 Harmonic content (a) and standard deviation (b) in units measured by iso-perimetric, radial, and tangential coil in the dipole center inserting additional distortion.

Clearly, the distortion has increased the standard deviation on the tangential coil measurements that results to be the only coil affected by the distortion.

8.2 Measurements on a bending corrector dipole

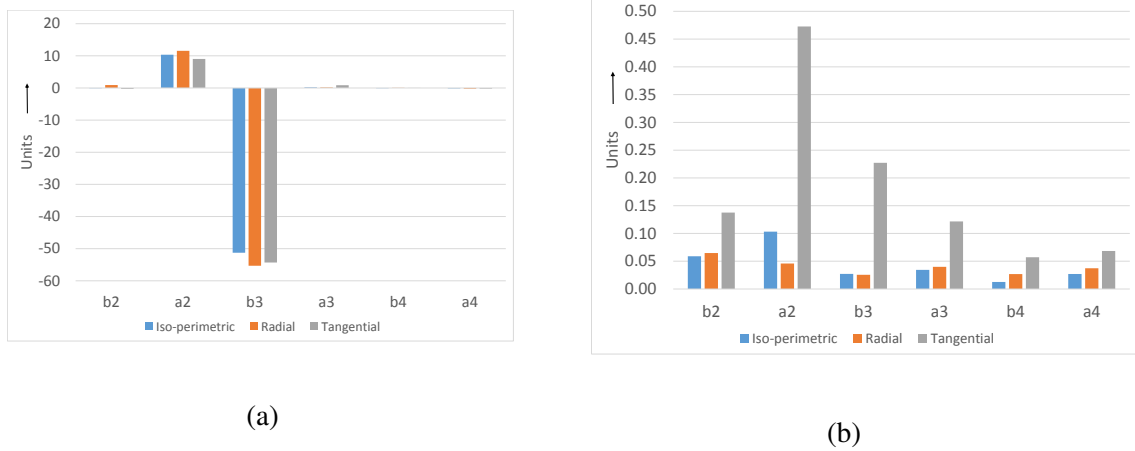


Fig. 8.5 Harmonic content (a) and standard deviation (b) in units measured by iso-perimetric coil, radial coil, and tangential coil in the dipole edge.

Fig. 8.5a and Fig. 8.5b show the results at the magnet edge. The results show a degradation on the tangential and on the radial coil, while the iso-perimetric coil almost keeps the standard deviation.

This result confirms that the iso-perimetric coil is not sensitive to the axial field components and is therefore suitable for field profile measurements.

8.2 Measurements on a bending corrector dipole

The measurements on the bending corrector dipole were performed to compare the integrated field harmonics measured by using a long shaft and the integrated field harmonics obtained by using a short rotating coil. The magnet under test, see Fig. 8.6, was measured performing a longitudinal scan along the magnet length using the three different transducers (Hall probe, radial coil, and iso-perimetric coil).

Validation and field measurements

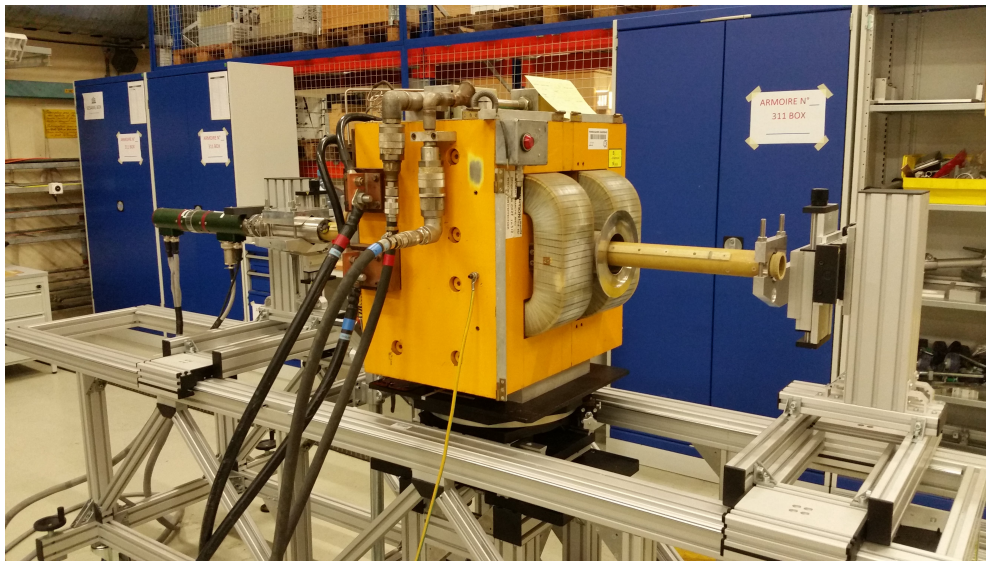


Fig. 8.6 Measurements set-up on dipolar magnet (long tangential coil shaft installed).

A degaussing and a pre-cycle were applied in order to be sure in having the same working point on the BH curve, see Fig. 8.7.

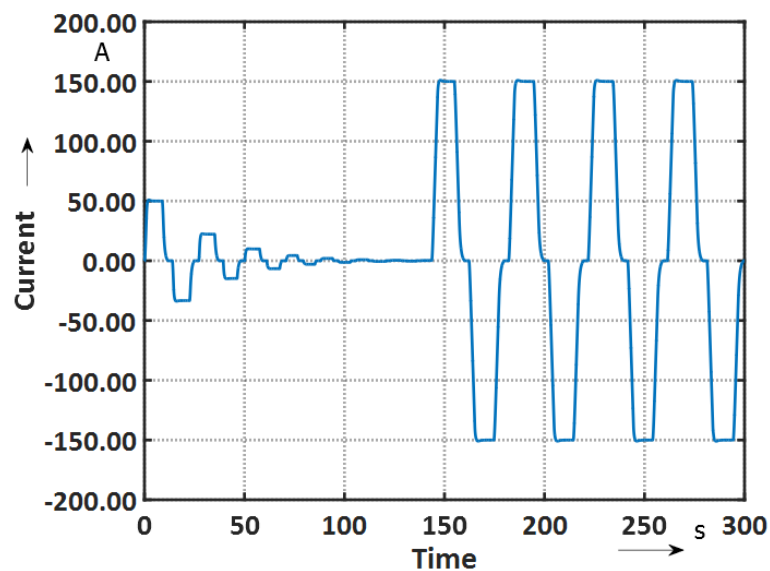


Fig. 8.7 Degaussing and pre-cycle applied on the bending corrector dipole.

To validate the design of the new sensor a particular measurement set-up was settled. The idea was to proof the non-sensitivity to the z -component of the new iso-perimetric induction coil.

8.2 Measurements on a bending corrector dipole

The measurement system was composed of: i) magnetic measurement bench having two linear stage that allowed to slide the sensor along the magnet aperture, ii) acquisition system with four FDIs (Fast Digital Integrator), a motor control, an encoder board and two level-meters, iii) transducer with two coils (radial coil and iso-perimetric) and two Hall probes (first prototype).

As first step a FDI calibration was performed measuring, in the dipole centre, the induced voltage on one radial coil (external one). The coil was connected to each FDI, repeating the measurement four times (one for each integrator). Imposing the equality in term of fluxes, the FDIs were calibrated.

In Tab. 8.1 are given the FDI's calibration factors.

1^{st} FDI	1^{nd} FDI	3^{rd} FDI	4^{th} FDI
1.0068987	1.0117332	1.0000253	1.0000000

Table 8.1 FDIs calibration factors.

Secondly, few measurements were performed on the magnet centre in order to perform an in-situ calibration of the developed sensor and of the Hall probes. To cross calibrate the transducers, some measurements were performed in the magnet center.

By using the calibration results obtained in the reference magnets for both the coils, was possible to check the measuring radius of the coil and prove the possibility of using the scaling law in regions where there is not z -field component. The Hall probe positioned at the same radius of the iso-perimetric coil was then calibrated using the results, in term of harmonics, coming out from the iso-perimetric coil measurements.

Thirdly, the integral field of the magnet under test was measured using a standard long rotating coil. It is a 1200 mm long tangential coil shaft with measuring radius of 30 mm. A scan was then performed by measuring, locally, the magnetic field distribution using the short rotating coil along the same length of the long tangential coil (1200 mm). From the scan was possible to compute the integral field harmonics and then compare the results with the integrated harmonics obtained by using the long coil. The harmonics measured by the long coil were scaled down to the iso-perimetric or radial coil radius and then compared. From theory, the first harmonic (main field) and all the odd harmonics measured by the three different sensors must be comparable. Differences, due to the z -field component, should be only on the even harmonics. This is true because, the effect of the z -field component

Validation and field measurements

correlated to odd harmonics is compensated in a full turn.

Normally, the even harmonics are not present in simulation results and are often negligible in standard magnets. The measured magnet was chosen for its considerable high harmonic content to emphasize the effect of the z -field component and of the non-linearity.

As result for this consideration, the following graph (Fig. 8.8), shows the integrated harmonics of the magnet calculated at the smallest radius, that is radial coil radius 11.36 mm. In particular, in blue the harmonics measured by the radial coil, in orange by the iso-perimetric coil and in grey measured by the long tangential coil.

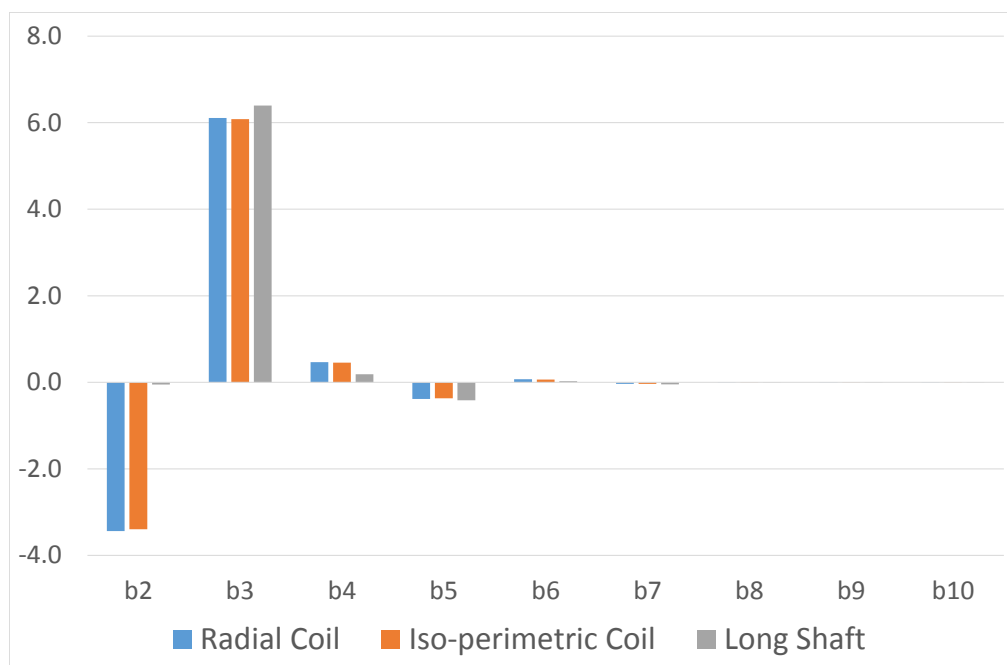


Fig. 8.8 Integrated harmonics at 11.36 mm. In blue the harmonics measured by the radial coil, in orange by the iso-perimetric coil and in grey measured by the long tangential coil.

Fig. 8.8 shows a large difference in the second harmonic that could be correlated to an error on the centering of the coils inside the magnet aperture. Regarding the higher harmonic orders, the differences between the iso-perimetric and radial coils are in the uncertainty range of the measurements. In this case, having performed a scan in the center of the aperture, it is not easy to notice the effect of the z -field component. In this position the z -field component has the lowest entity and consequently less effect on the coil. Furthermore, the odd field

8.2 Measurements on a bending corrector dipole

components, due to the symmetry, cancel out their effect.

To emphasize its effect, some measurements were performed close to the magnet pole (off center), where the z -field component is bigger. The following graph, Fig. 8.9, shows the integrated harmonics, expressed in units, for both the coils and Fig. 8.10, shows the difference between the two transducer.

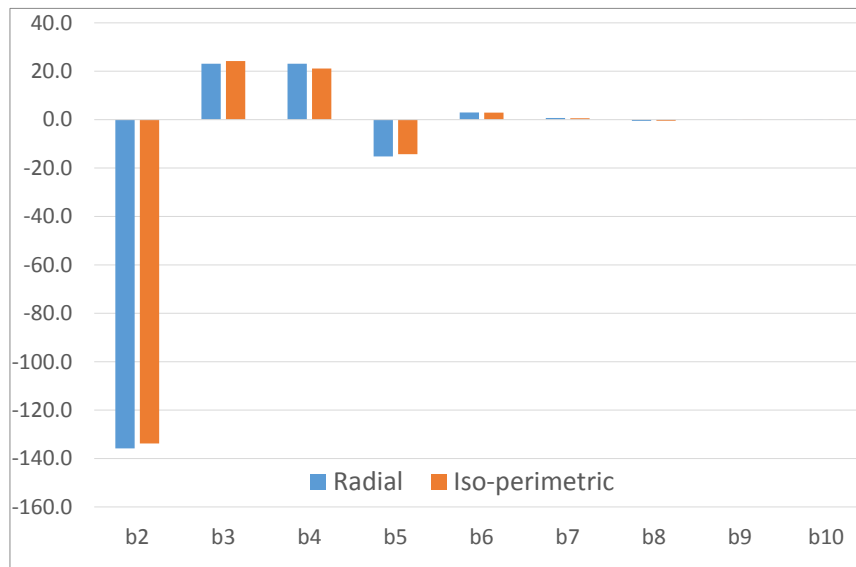


Fig. 8.9 Integrated harmonics off center measured by radial (blue) and iso-perimetric (orange) coil.

Validation and field measurements

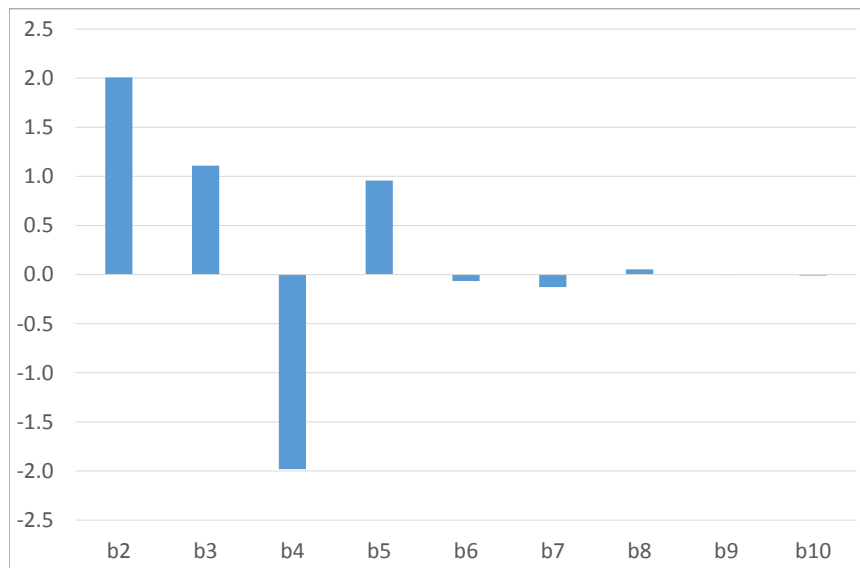


Fig. 8.10 Differences in units between radial and iso-perimetric integrated harmonics.

It is possible to notice, on the first four harmonics (b_2, \dots, b_5), that only the even harmonics have a significant difference. This is due to the symmetry of the z -field component of the odd components.

The following graph shows the harmonics measured in the magnet center by the coils and by the Hall probe. The difference in term of harmonics is given by the non-linearity of the Hall sensor plus the contribution due to a possible difference between the two-measuring radius (mechanical tolerances of the Hall probe and the iso-perimetric coil radius).

8.2 Measurements on a bending corrector dipole

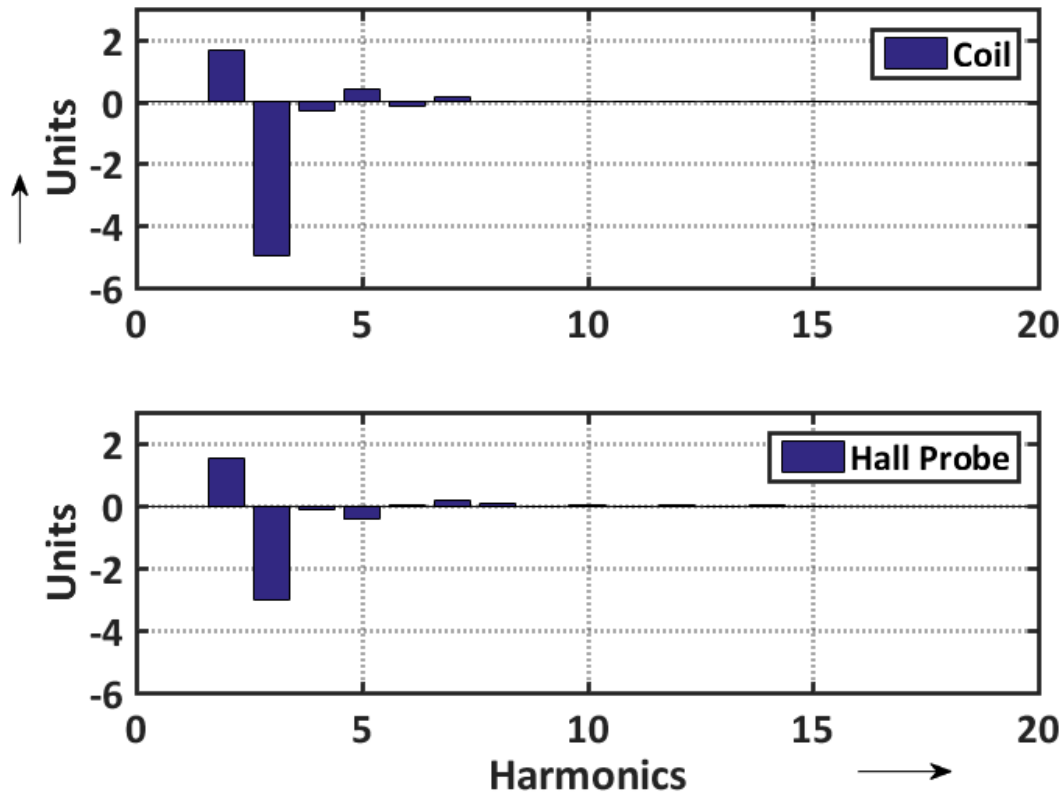


Fig. 8.11 Harmonics in unit measured in the magnet center by using the iso-perimetric coil and the Hall probe.

To separate the two sources of error would be enough to perform a calibration in the reference dipole and in the reference quadrupole at different field levels (current levels) to find the Hall probe calibration vector for each harmonics order. For Hall probes, it is important to obtain a calibration vector for each harmonic and not only a calibration factor. Since the purpose of this dissertation is not to perform measurements using Hall probes but, use them to have a qualitative behaviour of the field profile, the Hall probe calibration was performed in-situ, in the magnet center, powering the magnet at the nominal current (150 A). The calibration vector is defined as:

$$K_n^H = \frac{B_n^C}{B_n^H} \quad (8.1)$$

where B_n^C are the harmonics measured by the rotating coil and the B_n^H are the harmonics measured by using the Hall-probe. The vector K_H has been calculated for the normal components from the main harmonic (B_1) to the 15th harmonic order (B_{15}). Applying the

Validation and field measurements

calibration factor, is possible to measure the longitudinal field profile using the Hall probe. All the performed measurements were scaled to the radial coil radius.

The first two charts in Figure 8.12a and 8.12b show the B_1 measured performing a longitudinal scan in two different positions: in the center of the magnet aperture and off center. Three different profiles are plotted: in blue the profile measured by using the radial coil, in red the iso-perimetric coil and in orange the Hall probe.

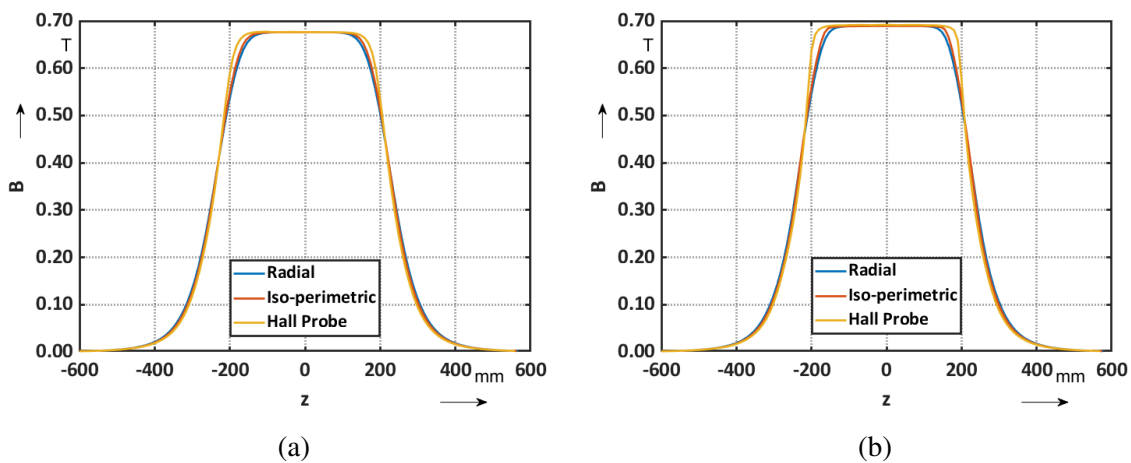


Fig. 8.12 Measured B_1 in the magnet's aperture center (a) and off center (b).

The measurements on each position z are averaged on 20 turns for each position. The 3σ (standard deviation) for the measured main field profile is shown in Fig. 8.13.

8.2 Measurements on a bending corrector dipole

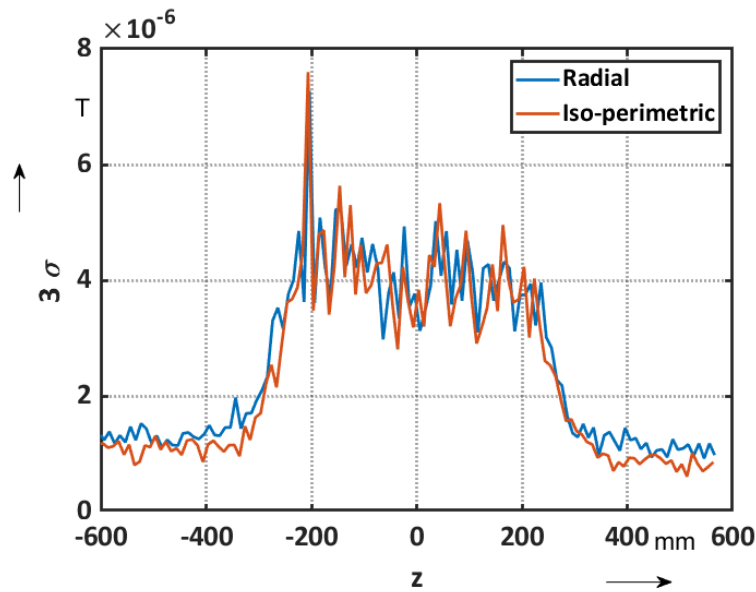


Fig. 8.13 Standard deviation, 3σ , for B_1 . In blue for the radial coil and in orange for the iso-perimetric coil.

The standard deviation for the main field profile measured off center is consistent with the standard deviation in the center. Instead, the standard deviation of the Hall probe has been not plotted since the result is one order bigger than the rotating coil and constant along all the scan ($6 \cdot 10^{-5}$) T. In Fig. 8.12a and Fig. 8.12b, is clear the effect of the coil length (convolution) on the measured field profile. To emphasize the effect of the coil length and show what is the effect of the convolution, in Fig. 8.14 is plotted the B_3 profile measured by the radial coil, the iso-perimetric coil and the Hall probe. It is important to highlight that, even using the shortest possible rotating coil, it will apply a convolution that will average (smooth) the field profile.

Validation and field measurements

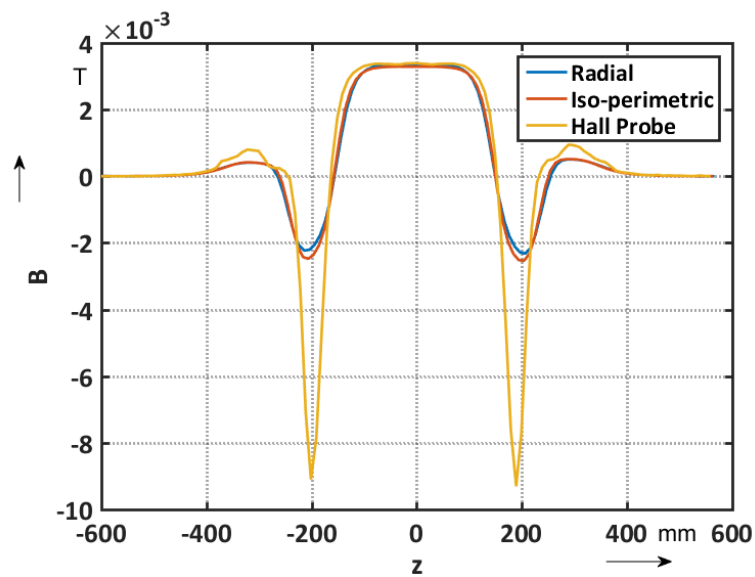


Fig. 8.14 B3 field component along the magnet length. Measured by radial coil in blue, iso-perimetric coil in red and by Hall probe in orange.

Another important parameter to consider is the bucking ratio. The bucking ratio is the ratio between the main harmonic component measured by the main coil and compensation coil. Ideally this ratio should be infinite, but due to mechanical tolerances, misalignment, and differences in the coil surface, usually, is in the range of 100 - 3000. In Fig. 8.15a and Fig. 8.15b the bucking ratio for iso-perimetric and radial coil is plotted at two different position in the magnet aperture (center and off center).

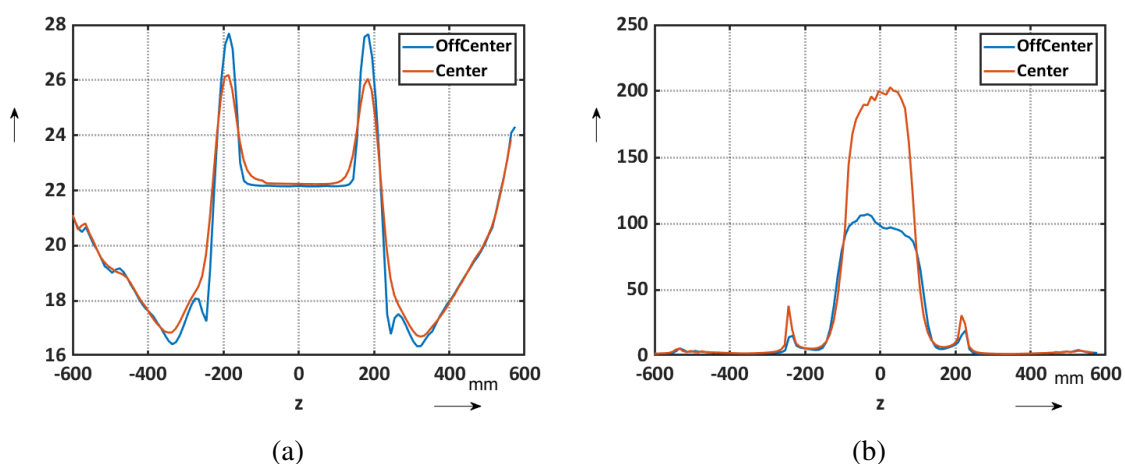


Fig. 8.15 Bucking ratio in the aperture center (red) and off center (blue) for iso-perimetric coil (a) and radial coil (b).

8.2 Measurements on a bending corrector dipole

The bucking ratio for the iso-perimetric coil is much lower than the bucking ratio for the radial coil, this is due to the mechanical tolerances on the cylindrical shaft.

Even if the absolute value of the bucking ratio for the iso-perimetric coil is not high, the variations between the magnet center and the fringe field area is considerable smaller than the variation for the bucking ratio of the radial coil. This is because of the z -field component. Indeed, the z -component does not only introduce differences since it introduces electromotive force in the coil, but even for the fact that the main field component B_y , in the fringe field, becomes function of the radius. This is another important reason for which the scaling laws are not applicable anymore in the fringe field. Indeed, looking at the main field component profile in Fig. 8.12a and Fig. 8.12b, it is clear that the B_1 roll off is different measuring at two different radius. In this case radius means the distance from the center of the magnet aperture to the rotational axis of the coil. The straight region, plateau in the plot, is longer for the measurements close to the pole.

The iso-perimetric coil compensation, should not be influenced by this difference because the two coils (main and compensation) measure the main field component on the same radius. But, since by construction the length of the two coils is different (main coil shorter than the compensation coil) the integrated measured flux is different while measuring in the fringe field region.

The variations in the bucking ratio for the iso-perimetric coil is correlated to the difference in term of length between main and compensation coil.

For the radial coil transducer, compensation and main coil have the same length, but the variation of the bucking ratio is much bigger. This is because the measuring radius of the two coil is different and the z -field component itself induces electromotive force in the coil. For this reason, future developments on the iso-perimetric coil transducer must foresee both the coils with the same measuring length. The idea would be to build a sensor with some layers only for the main coil tracks and some others only for the compensation coil tracks. Furthermore, the compensation coil, in case of dipole compensated coil, should be built having the same measuring radius of the main coil and not only turns on the same radius.

Since the production of such transducer is not easy, a possible option would be to build only a main coil with considerable high resolution for field harmonics. This could be a possible solution thanks to the fact that usually, in the fringe field regions, the absolute value of the harmonics is considerably high and thanks to the fact that a higher standard deviation is accepted. Figure 8.16 shows the absolute 3σ for the measured B_3 component by using only the main coil.

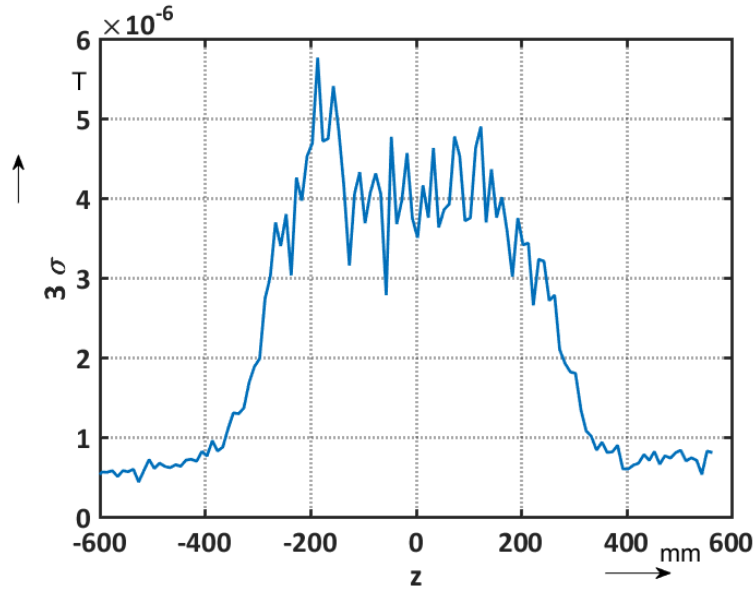


Fig. 8.16 3σ standard deviation for the B_3 component measured by the main coil of the iso-perimetric transducer.

Since the bucking ratio of the first prototype is not enough to obtain advantages from the bucking, the standard deviation of the main coil is comparable with the STD of the compensation coil. Ultimately, we could expect a standard deviation of 0.1 units by using only the main coil. This value could be decreased to 0.01 units improving the mechanics of the measurement system.

As claimed previously, the measured profile obtained by using short rotating coils is a convolution between the field profile and the test functions of the sensing coil. To find out the “real” field profile there are two possible ways:

- solve the deconvolution problem,
- use the FEM analysis by solving a reverse engineering problem.

8.2.1 Measurement data deconvolution

The measured harmonic field profiles are affected by the convolution due to the measurements step size while performing the longitudinal scan. The scope is to obtain the deconvoluted field profile to apply, then, the pseudo-multipoles theory for reconstructing the all field map. The challenge is to compute the $C_{n,n}(z)$ in equation 2.56. The $\tilde{B}_n(r_0, z)$ denote the measured,

8.2 Measurements on a bending corrector dipole

transversal field component of order n , sampled at positions z along the magnet axis and it is affected by noise $n(z)$. The noisy, convoluted signal is given by

$$\tilde{B}_n(r_0, z) = \left(s_n(z) * B_n(r_0, z) \right) + n(z) , \quad (8.2)$$

where s_n is the sensitivity function of the coil. The convolution in frequency domain becomes

$$\mathcal{F}\{\tilde{B}_n(r_0, z)\} = \mathcal{F}\{s_n(z)\}\mathcal{F}\{B_n(r_0, z)\} + \mathcal{F}\{n(z)\} , \quad (8.3)$$

To obtain the reconstructed multipole-field distribution we apply a discrete filter, $\mathcal{F}\{f_w(z)\}$, that is the inverse of the coil sensitivity. We call $\hat{B}_n(r_0, z)$, the reconstructed distribution given by

$$\mathcal{F}\{\hat{B}_n(r_0, z)\} = \frac{\mathcal{F}\{\tilde{B}_n(r_0, z)\}}{\mathcal{F}\{s_n(z)\}} , \quad (8.4)$$

Obviously, this approach will amplify the noise $\mathcal{F}\{n(z)\}$ for all the frequencies where the spectrum of the sensitivity function has small values.

To solve this issue the Wiener-Kolmogorov filter could be used ($\mathcal{F}\{W(z)\}$) instead of $\mathcal{F}\{f_w(z)\}$.

$$\mathcal{F}\{W(z)\} = \frac{1}{\mathcal{F}\{s_n(z)\}} \frac{|\mathcal{F}\{s_n(z)\}|^2}{|\mathcal{F}\{s_n(z)\}|^2 + \frac{\mathbb{E}[\mathcal{F}\{n(z)\}]^2}{\mathbb{E}[\mathcal{F}\{B_n(r_0, z)\}]^2}} , \quad (8.5)$$

In this case the filter will minimize the expected mean-square error in the frequency domain that is defined as

$$\mathbb{E}[e^2] = \mathbb{E} \left[|\mathcal{F}\{B_n(r_0, z)\} - \mathcal{F}\{\hat{B}_n(r_0, z)\}|^2 \right] . \quad (8.6)$$

The denominator $\frac{\mathbb{E}[\mathcal{F}\{n(z)\}]^2}{\mathbb{E}[\mathcal{F}\{B_n(r_0, z)\}]^2}$ is the inverse of the expected signal-to-noise ratio SNR . Applying this filter, the noise will be equally distributed on all the harmonics.

Unfortunately, in this case the result of the deconvolution will be strongly depended of the expected signal to noise ratio, that is not always well known a priori.

For the performed measurements campaign some FEM simulations were performed on the magnet and the field distribution as well as the SNR were approximately known. The computed SNR was applied in the filtering to compute the deconvoluted field distributions. In Fig. 8.17 the deconvolution of the main field component is plotted.

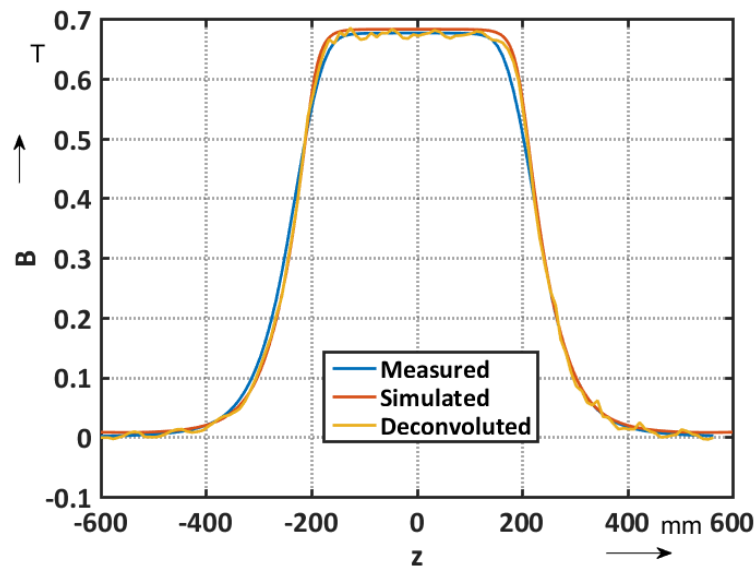


Fig. 8.17 B_1 field distributions. In blue the measured, in red the simulated and in orange the deconvoluted distribution.

The effect of the noise on the data is visible already on the B_1 distribution. It could be possible to smooth the reconstructed field distribution since the main field profile is quite smooth by itself. We could not expect the same noise and the same possibility of smoothing on the high harmonic order. Usually the SNR of high harmonic order is lower and the distributions are not smooth. Fig. 8.18a and Fig. 8.18b show the measured, the simulated and the deconvoluted B_3 and B_5 field profile.

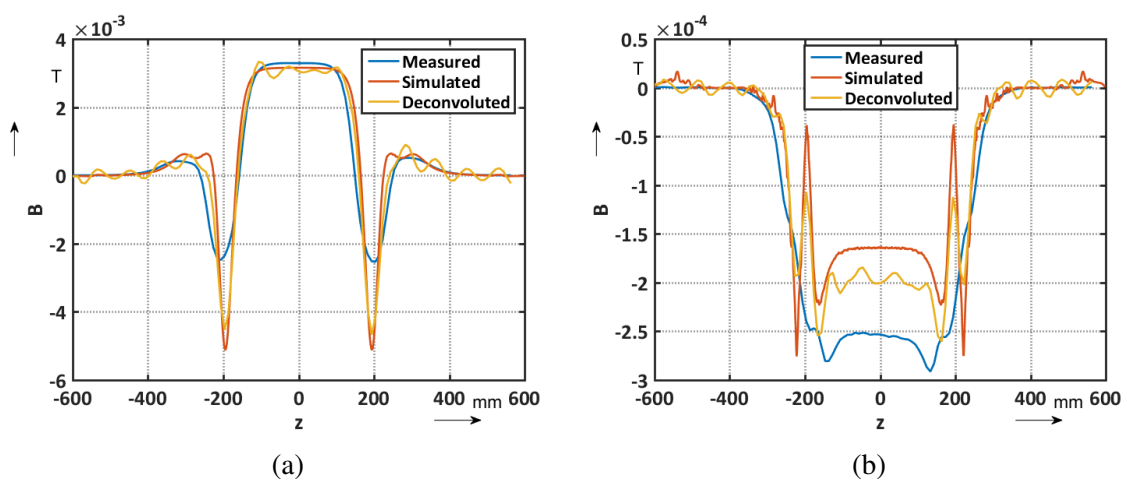


Fig. 8.18 B_3 (a) and B_5 (b) field distributions. In blue the measured, in red the simulated and in orange the deconvoluted distribution.

8.2 Measurements on a bending corrector dipole

As expected the noise level increase increasing the harmonic order. The harmonic profile of this particular magnet, becomes more edgy when the harmonic order increases. To obtain the results plotted in the previous figures, the *SNS* applied in the Wiener filter for the deconvolution was adjusted knowing the simulated field distribution. As expected the deconvoluted signal results to be noisy, but definitely better than the deconvolution performed using Eq. 8.4. The measured normal field distribution components were deconvoluted and used to compute the all field distribution applying the pseudo multipole analysis. Some results are plotted in the next figure. The field was computed for some radii $r = [0, 2, 4, 6, 11, 18, 19]$ mm and for some angles $\varphi = [0, 30, 45, 60, 90, 120, 135, 150, 180, 210, 225, 240, 270, 300, 315, 330, 360]$ °.

Using the equations

$$B_r(r, \varphi, z) = -\mu_0 \sum_{n=1}^{\infty} r^{n-1} (\bar{C}_n(r, z) \sin(n\varphi) + \bar{D}_n(r, z) \cos(n\varphi)) , \quad (8.7)$$

$$B_\varphi(r, \varphi, z) = -\mu_0 \sum_{n=1}^{\infty} nr^{n-1} (\tilde{C}_n(r, z) \cos(n\varphi) + \tilde{D}_n(r, z) \sin(n\varphi)) , \quad (8.8)$$

$$B_z(r, \varphi, z) = -\mu_0 \sum_{n=1}^{\infty} r^n \left(\frac{\partial \tilde{C}_n(r, z)}{\partial z} \sin(n\varphi) + \frac{\partial \tilde{D}_n(r, z)}{\partial z} \cos(n\varphi) \right) , \quad (8.9)$$

is possible to compute the field in the desired position inside the magnet aperture. For example in Fig. 8.19 the z -field component was computed using the measured data for $r = 0$ mm, $r = 4$ mm, $r = 11$ mm and $r = 19$ mm, imposing $\varphi = 90^\circ$.

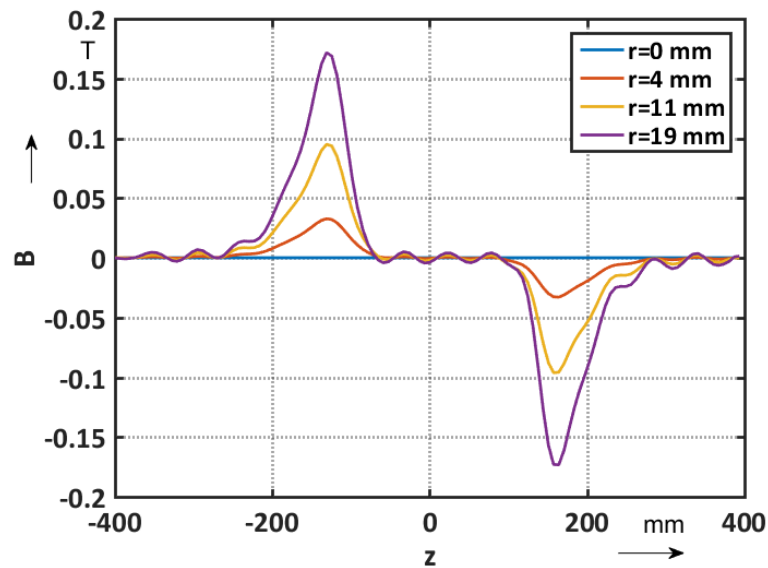


Fig. 8.19 Computed z-field component using measured data for different radius at $\varphi = 90^\circ$.

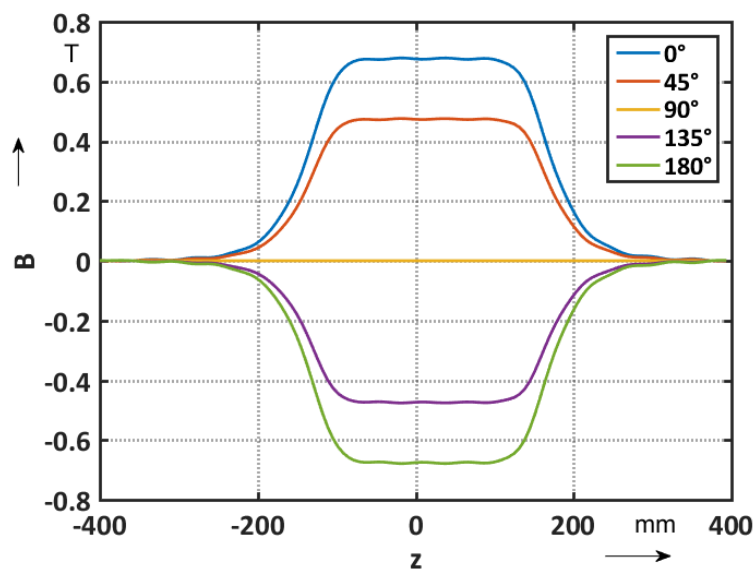


Fig. 8.20 Computed B_φ component at $r = 19$ mm.

8.2.2 Reverse engineering solution

FEM analysis are a powerful tool to obtain good qualitative and quantitative information of the integrated field of accelerator magnets. Unfortunately, the accuracy of the analysis cannot

8.2 Measurements on a bending corrector dipole

better than few % in comparison with measurements (due to uncertainty in the measurements of the BH curve, mechanical tolerances in the magnet production and assembly, deformation in the coil position, saturation effects, etc.). For this reason, is not impossible to rely on simulation for the computation of the harmonics field profiles.

A valid alternative could be to measure the integrated field harmonics of the magnet under test using a long rotating coil, adjust the FEM model in a way that the computed integral harmonics match the measured values, and then base all the optical studies only on the FEM results. In this case, deformation or differences in the symmetry of the magnet would not be taken into consideration. This is the reason why a different approach was considered.

Since the sensitivity function of the coil is well known, as well as, the step size of the measurements, it is possible to apply the convolution between the simulated harmonics profile and the sensitivity factors of the coil, and then compare the obtained results with the measured field profile. When the differences (in term of integrated harmonics) between the convoluted simulation results and measurements are lower than the standard difference between measurements and simulations (%) is possible to use the FEM results for the beam dynamics studies. The Fig. 8.21 shows the convolution between the computed B_1 and the measured B_1 (iso-perimetric coil).

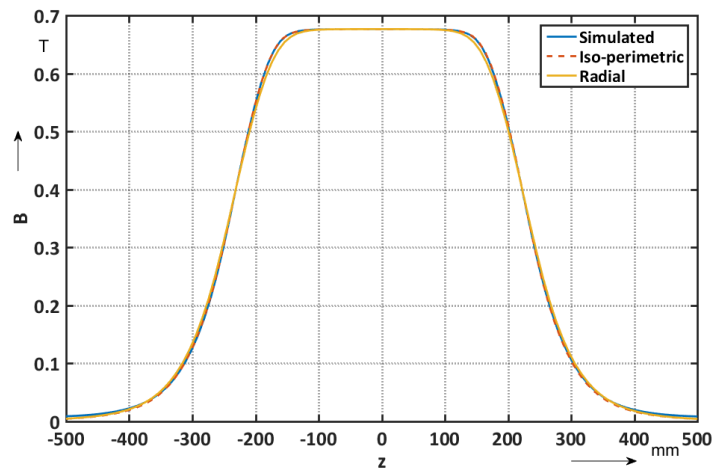


Fig. 8.21 B_1 simulated and convoluted (blue), B_1 measured by the iso-perimetric (red) and standard (orange) coil.

The integrated field (B_1) of the convoluted signal (simulation result with test function) is 0.3385 Tm, the integrated field given by the measurements using the iso-perimetric coil is 0.3360 Tm, while the measurements performed by the standard (radial) coil in the same

Validation and field measurements

position is 0.3361 Tm. The differences in units are: 74 units in the first case and 71 units in the second case. Considering the integrated field, we would conclude that the measurements performed with the radial coil give a better result. But, looking in detail Fig. 8.22a, is possible to notice the effect of the z -field component on the measurements performed by the radial coil on the end regions of the magnet. In particular, the z -field component is higher on the connection side (red dotted curve in the plot at $z = [-300, -200]$ mm). To highlight the influence of the z -field component, the same analysis was performed in a position off center (close to the magnetic pole of the magnet). In this latest case, is clear that the effect is higher. The blue curve in the plot represents the difference between the convoluted signal (simulations and test functions) and the measured B_1 by using the iso-perimetric coil.

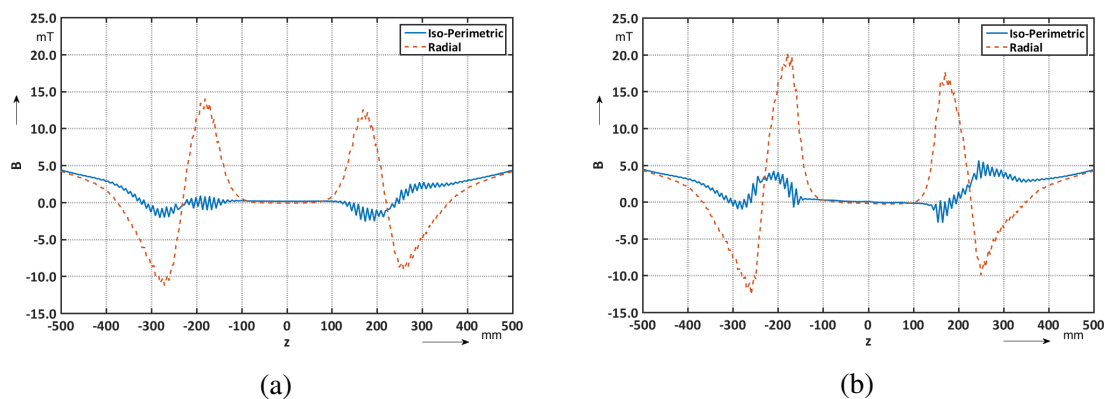


Fig. 8.22 Difference between the convoluted signal and the measured B_1 . Iso-perimetric (blue) and radial coil (red). In the magnet center (a) and off center (b).

The next two figures show the simulated B_1 and B_3 (Fig. 8.23) and the coil sensitivity functions s_1 and s_3 (Fig. 8.24).

8.2 Measurements on a bending corrector dipole

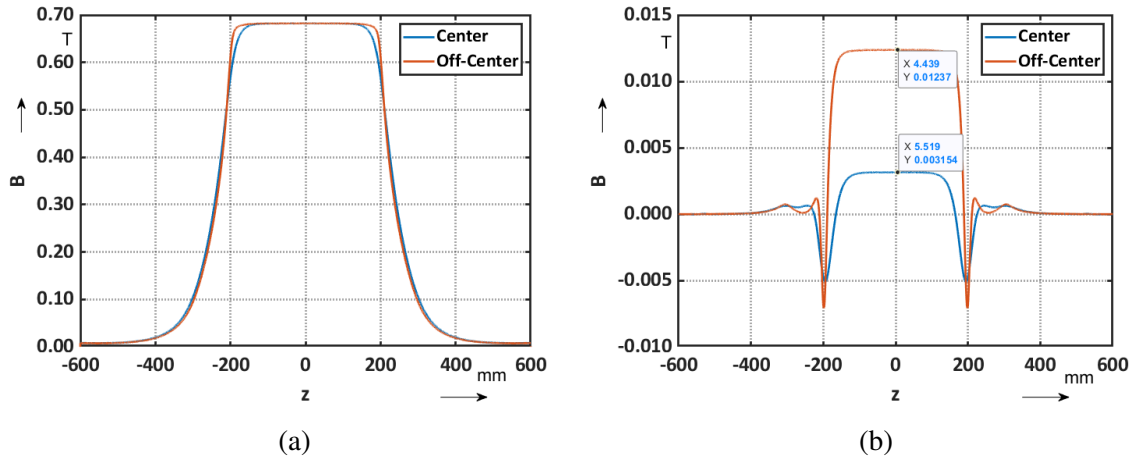


Fig. 8.23 Simulated B_1 field profile (a) and B_3 field profile (b).

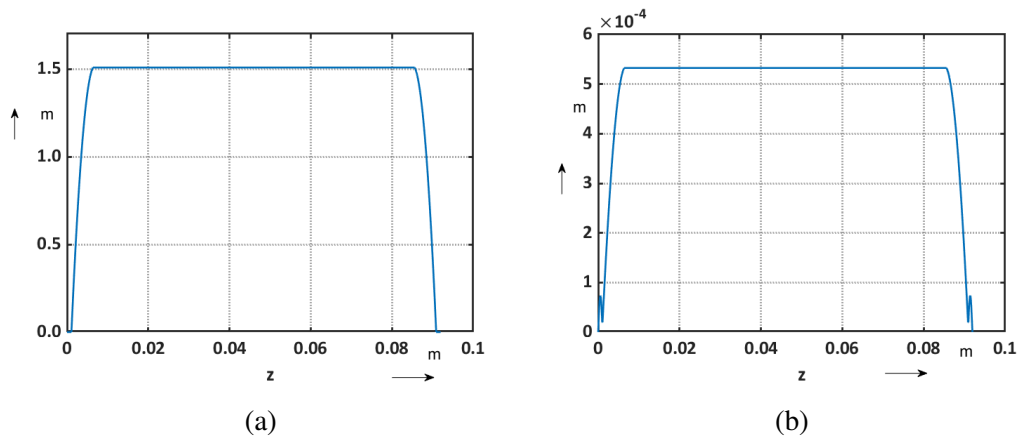


Fig. 8.24 Coil sensitivity functions: s_1 (a) and s_3 (b).

For example, the measured B_2 and B_5 profile are plotted in the following charts. The difference in amplitude is because the computed sensitivity functions of the iso-perimetric coil are affected by the mechanical tolerances of the shaft. Besides, the roll-off of the odd harmonic, measured with the two different sensors does not have a significant difference, while for the even harmonics the differences are bigger.

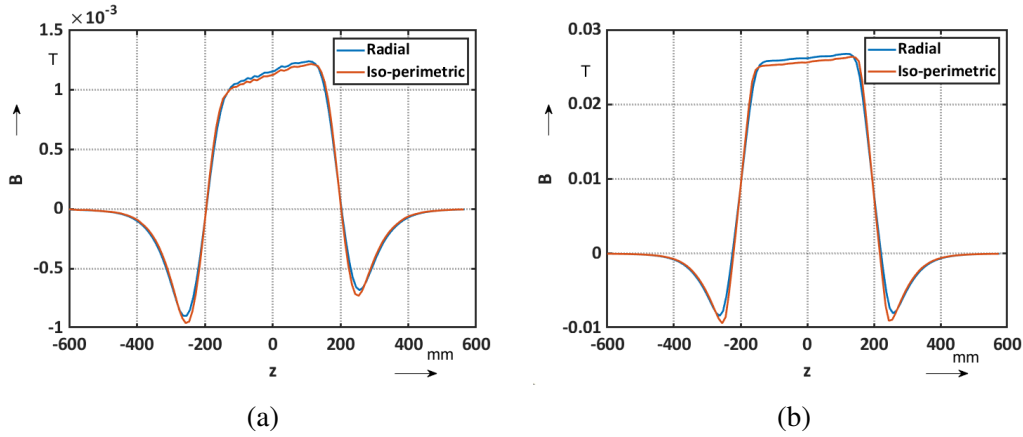


Fig. 8.25 B_2 field profile measured in the magnet center (a) and off center (b).

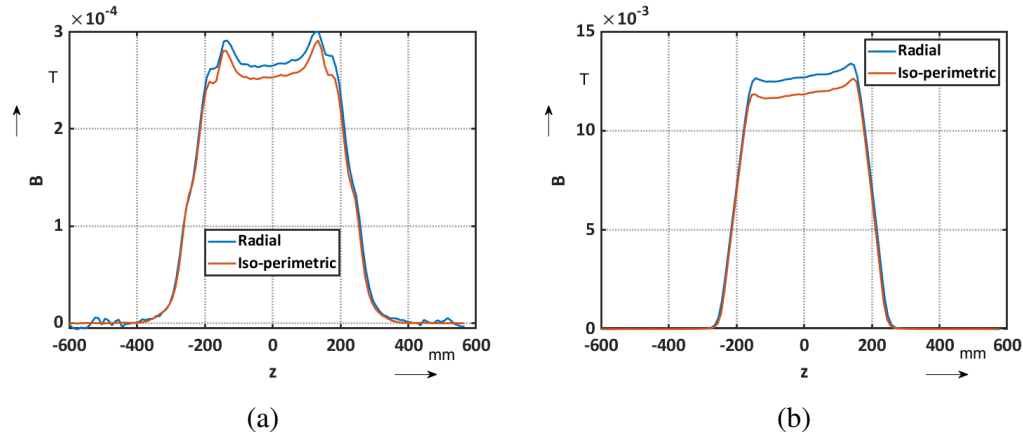


Fig. 8.26 B_5 field profile measured in the magnet center (a) and off center (b).

8.3 Magnetic measurements on a Canted-Cosine-Theta magnet

In the frame on the measurements campaign for Hi-Lumi project, some measurements were requested on the on a twin-aperture orbit corrector. It is a superconductor canted-cosine-theta (CCT) dipole. This is a novel design for one of the CERN LHC Hi-Lumi upgrade magnets. The idea is to have a magnet with integrated field of 5 Tm and multipoles < 10 units at all operational fields and configurations. The goal of Hi-Lumi LHC is to increase the Luminosity by factor 10 in CMS and ATLAS installation due 2024 – 2026.

The measured short model has a coil length of 0.5 m coils and presents two apertures of 105

8.3 Magnetic measurements on a Canted-Cosine-Theta magnet

mm in diameter.

The measurement system was composed of: one bench with transversal motorized slider system, one MRU, one measurement rack and the new transducer. In addition, some measurements were performed with a 1200 mm long shaft to have a complete set of measured data.

The measurements have been performed at room temperature with current 1 A.

The scope of the measurements is to provide the field harmonic distributions as well as the roll off of the harmonics in the fringe field regions. The following list represents the performed measurements:

1. Integral measurement (Shaft $L = 1200$ mm , $R = 35$ mm),
2. Iso-Perimetric coil measurements (Shaft $L = 84.5$ mm $R = 19$ mm) .

Since measurements were performed at different radii and considering that the scaling law are not applicable for short rotating coil measurements, the integrated multipoles measured by using the long coil ($L = 1200$ mm) are the only quantities that could be scaled down to the iso-perimetric coil radius.

The next tables show the measurement results in units. Tab. 8.2, shows the normal and skew multipoles expressed measured by the 1200 mm long shaft at $R = 35$ mm, $B_1 = 0.0017$ T.

Order	bn @ 35 mm	an @ 35 mm
2	3,2211	4,1811
3	-7,6379	2,1809
4	-1,0830	1,4831
5	-0,8195	-0,1407
6	-0,4184	0,4739
7	0,3320	-0,1535

Table 8.2 Integrated normal and skew multipoles in units measured by using the tangential coil $L = 1200$ mm @ $R = 35$ mm.

In Table 8.3, are shown the normal multipoles measured by using the iso-perimetric coil, $B_1 = 0.0017$ T.

Validation and field measurements

Order	b_n @ 19 mm	a_n @ 19 mm
2	2,3516	1,4804
3	-2,8174	0,2051
4	-0,1607	0,2107
5	-0,0391	-0,0027
6	-0,0257	0,0722
7	0,0533	-0,0379

Table 8.3 Integrated normal and skew multipoles measured by using the iso-perimetric coil.

The aim of the measurements was to provide the field distribution along the magnet length. In the next figures the field distributions in Tesla (B_1 , B_2 , B_3 and B_5) are plotted.

In Figure 8.27 is plotted the main field component.

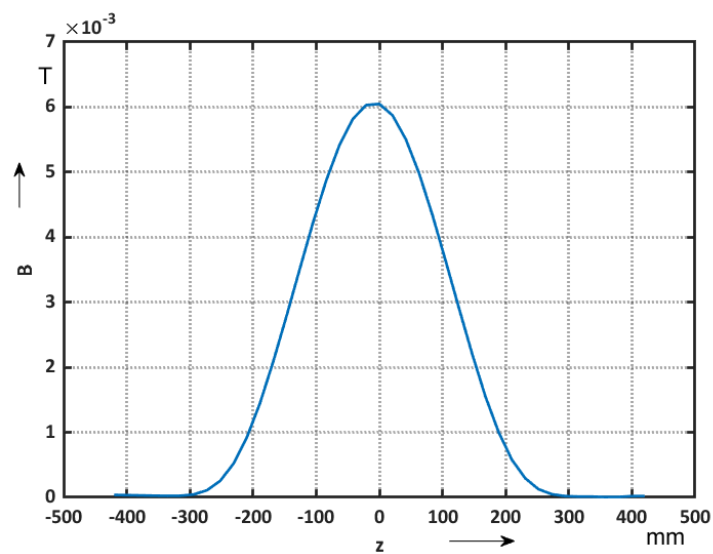


Fig. 8.27 B_1 field component on the CCT magnet.

Fig. 8.28, shows the B_2 field distribution, Fig. 8.29 the B_3 and Fig. 8.30 the B_5 .

8.3 Magnetic measurements on a Canted-Cosine-Theta magnet

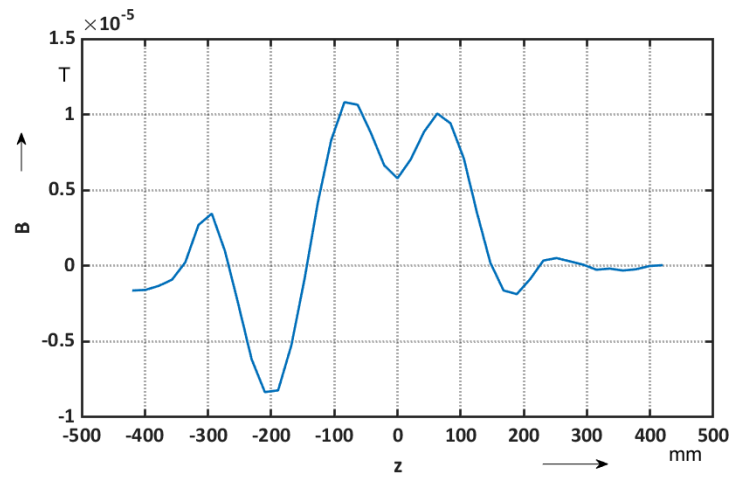


Fig. 8.28 B_2 field component on the *CCT* magnet.

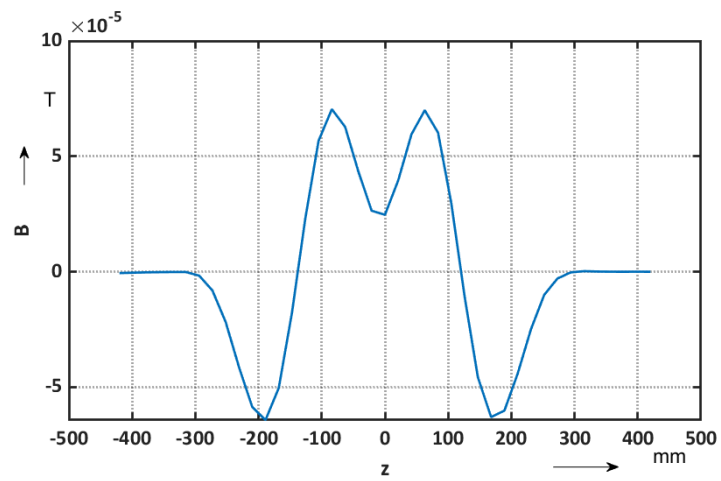


Fig. 8.29 B_3 field component on the *CCT* magnet.

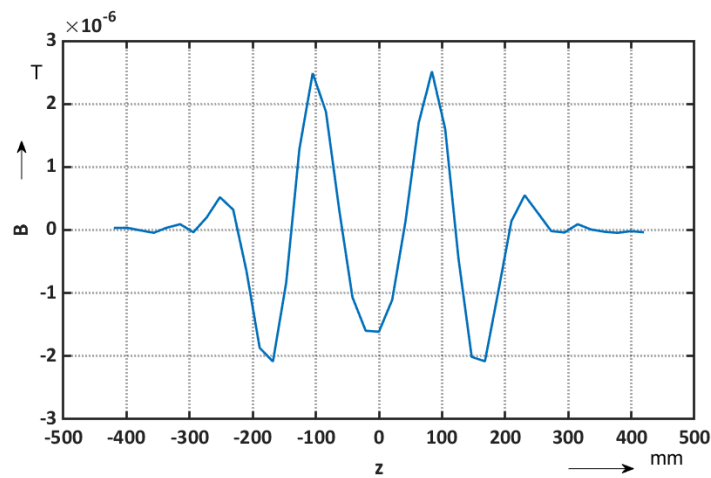


Fig. 8.30 B_5 field component on the *CCT* magnet.

Performing the same procedure described in the previous section, the performed measurements were compared with the simulation data and the FEM model was adjusted.

8.4 Medical applications

The designed saddle shaped iso-perimetric coil, applied for measuring the magnetic field profile of accelerator magnets, could have application in the medical field.

In fact, saddle shape coils are applied in **E**lectro**M**agnetic **A**ctuation (*EMA*) for 3D locomotion of microrobot. Nowadays, minimally invasive surgery is becoming more and more important to reduce the recovery time and reduce at the minimum the scar. Microrobots could be moved in the blood vessel for coronary arterial treatment. Microrobots use magnetic forces and torques to move inside the blood vessel. In [10] a 3D locomotion *EMA* system based on a pair of stationary Helmholtz-Maxwell coils and a pair of rotating uniform and gradient saddle coils is presented. The uniform saddle coil is used to generate a uniform magnetic flux in the region of interest, while the gradient saddle coil is used to generate a uniform gradient in the region.

Some other applications are correlated to the magnetic resonance imaging (*MRI*), that is a method to visualize the inside of a human body from nuclear magnetic resonance (*NMR*) signal. There are some studies that aim to measure the *MRI* images during surgery for safe and reliable operation or to have the intraoperative *MRI*. In fact, by using *MRI* endoscopically early detection of tumours that occur in deep luminal tissue is expected. But, unfortunately, only the surface tissues are observed in the endoscopic imaging. For this reason, a combination of *MRI* and endoscope could help in acquiring the depth of the

tumours in addition to detecting the tumours in deep luminal tissues. To achieve this scope, it is important to improve the signal-to-noise ratio (*SNR*) of the *MRI* signal.

In fact, improving the *SNR* of the *MRI* signal it is possible to improve the *MRI* resolution. This is because the desired high-resolution *MRI* imaging reduces drastically the *NMR* signal. In this case becomes difficult to have imagines of small luminal tissues such as the oesophagus. The *SNR* of *MRI* signal is proportional to the number of turns of the *MRI* signal receiving coil, and inverse proportion to the diameter of the coil and the 0.5 power of the resistance of the coil [18]. In [14] a micro saddle shape coil with switchable sensitivity is presented. The switchable sensitivity is achieved by modifying the coil geometry, it means from a saddle shape coil to a planar coil. The difficulties of building such coil are highlighted in [14] were the diameter and the length of the fabricated coil are 20 and 30 mm, respectively. The number of turns of the coil is 10, the gap of the wiring is 600 μm . The width and the thickness of the coil wiring are 500 and 50 μm .

The designed saddle-shape coil for magnetic measurements could be a valid alternative for building such a medical sensor device.

8.5 Conclusions

In this chapter, the validation and the on-field measurements were discussed.

In particular, the transducers validation was performed in the reference dipole measuring the harmonic content. The functional tests have shown that the coil satisfy the requirement of standard deviation < 0.01 units.

After having validated the transducers, two measurements on field were performed.

The first application of the iso-perimetric coil transducer was to measure the magnetic field profile of a bending corrector dipole. The improvement due to this geometry gave the possibility to perform measurements in the fringe field regions achieving the same precision of standard rotating coil in the magnet's straight sections. The measured field profiles are convoluted by the coil test functions. The extraction of the pseudo-multipoles from the measured signal requires a sophisticated post-processing step based on the regularity conditions of the magnetic field. In fact, the measurand is a voltage signal that yields a convolution of the transversal field distribution with the sensitivity function of the induction-coil. To apply the pseudo-multipole theory, a deconvolution is therefore needed on the (noisy) measured data. For the deconvolution were evaluated two approaches: (i) solve the deconvolution problem with a Wiener filter, and (ii) measure the magnet-to-magnet reproducibility and gauge the numerical model of the magnet as built.

Validation and field measurements

The second application was to measure the behavior of the fringe field in the superconductor Canted-Cosine-Theta (CCT) dipole for the Hi-Lumi upgrade.

Conclusions

In this thesis, a magnetic field mapper based on rotating coil is presented. The mathematical model validation, the conceptual design, the systems architecture, the prototype manufacture, the validation measurements and calibration is shown. The new transducer has been used for the mapping of the fringing fields of two accelerator dipole magnets.

The proposed magnetic field mapper is based on an iso-perimetric transducer, produced with a flexible printed circuit (FPC) coil. The iso-perimetric coil transducer has been conceived to allow measurements of the field distribution along the magnet axis and to apply the pseudo-multipole theory for 3D field reconstruction. The transducer allows to perform measurements in the fringe field regions dominated by a strong axial field component.

The theory of pseudo-multipoles is known from the literature. The extraction of the leading term in the Fourier-Bessel series requires the solution of a differential equation by means of a discrete Fourier transform. Point-like measurements with Hall sensor stacks show limited accuracy due to non-linearities and planar effect. This motivated the measurement technique using induction-coil sensors. These require a novel design implying saddle-shaped, iso-perimetric coils in order to avoid interception of the axial field component.

Moreover, the compensation of the main voltage signal cannot be accomplished with the classical arrangement of tangential (or radial) induction coils at different radii, because no easy scaling law exists in the fringe field region.

It has been demonstrated experimentally that the axial field component intercepted by the standard coils, influences the traditional rotating coil measurements and therefore results in a systematic error in fringe-field measurements.

Conclusions

Validation tests on the iso-perimetric sensor have led to an optimization of the production technique for the flexible circuit board to be used as a rotating coil sensor.

Functional tests have shown that the transducer satisfies the requirement of being not sensitive to the axial field component, and the measurement standard deviation satisfies the requirements of being below one unit in 10000. However, the compensation ratio and the signal-to-noise ratio for the iso-perimetric coil are lower than for traditional coils. This is due to the mechanical tolerances on the sensor production and because the main and compensation coils have different lengths in order to be able to lie on the same measurement radius.

The extraction of the pseudo-multipoles from the measured signal requires a sophisticated post-processing step based on the regularity conditions of the magnetic field. In fact, the measurand is a voltage signal that yields a convolution of the transversal field distribution with the sensitivity function of the induction-coil. To apply the pseudo-multipole theory, a deconvolution is therefore needed on the (noisy) measured data. Measurement results and tests have shown that to solve this deconvolution problem with a Wiener filter, the spatial harmonics of the field distribution must be studied in advance.

Fortunately, this is possible using numerical field computation programs for accelerator magnet design yielding an a priori knowledge on the measurand. This allows a design of experiment based on the optimal number of coefficients, the required highest derivative of the longitudinal field distribution, and the maximum step size in the scanning process. It must be guaranteed that the spectrum of the test function is sufficiently wide to include the highest order spatial frequency of the magnetic field distribution in the accelerator magnet.

For the first time, it is possible to extract the transversal field components from measurements in the coil-end regions. If the transducer is sufficiently sensitive (which depends on the aperture of the magnet and the measurement radius of the transducer) the deconvolution process yields the entire field distribution, not only on the measurement radius but everywhere inside the sampled domain.

Another approach is to measure the magnet-to-magnet reproducibility and gauge the numerical model of the magnet as built. If the model, the magnet production and the measurement are coherent, the simulations can be used for beam-tracking studies. In this case a

deconvolution of the measured field distribution is not needed.

With the presented methodology and hardware it will also be possible to better characterize fast-ramping magnets and magnets with strong hysteresis effects, where 10^{-4} predictive numerical models do not exist.

The next variant of the transducer shall be designed with the same lengths of the main and compensation coils. This can be accomplished easily for induction coils of larger radii, as required for the HL-LHC project. The metrological characterization of the transducer has shown that it is limited by the stability of the bearings and the longitudinal positioning system. The mechanical design of the next version shall, therefore, be compatible with a newly procured 3-axis displacement stage and active vibration reduction on the measuring shaft.

List of figures

1.1	Rotating coil: (a) tangential and (b) radial coil scheme.	7
3.1	Simulated air-coil magnet.	26
3.2	Air-coil field harmonics (B_1, \dots, B_9).	27
3.3	B_1 reconstruction by using 2 nd , 4 th and 6 th derivative order.	28
3.4	Method for assessing the design parameters: harmonic order n and derivative order m	29
3.5	Numerical results of the field reconstruction residual R_B versus derivative m and harmonic order n . $n=[1, \dots, 15]$ and $m=[6, \dots, 14]$	30
3.6	B_y field component and reconstruction error (in percent) along z using $n=15$ and $m=14$	31
3.7	Numerical results of the field reconstruction residual R_B adding random noise on the field harmonics.	32
4.1	Sensor geometry of tangential coil.	34
4.2	Cross-sectional view of a radial coil turn displaced between two angular positions of arc lengths s_1 and s_2	35
4.3	Sensor geometry saddle-shaped, iso-perimetric coil.	36
4.4	Cross-section of the Flexible Printed Circuit (FPC) induction coil, with main and compensation coils (a) top view (b).	36
4.5	Optimized design of the dipole compensated coil with a magnified view of the inner coil (insert).	38
4.6	Sensitivity factors S_n at $R_{ref} = 19.065$ mm for the main and compensation coils (a) and for the compensated scheme (b)	38
4.7	3D rendering of the coil design (connection view).	39
4.8	3D rendering of the coil design.	40
4.9	Schematic of the sensitivity factor analysis.	41
4.10	Compensated coil sensitivity along the induction coil ($R_{ref} = 19.065$ mm).	42

List of figures

4.11	Sensitivity functions $s_n(z_i)$ along the extremities of the main induction coil and hard-edge model (geometric mean length).	43
4.12	Differences between the geometric mean and magnetic lengths as a function of the multipole order n	43
4.13	(a) Sensitivity factor at 11.4 mm from standard k_n formula (red) and proposed procedure (blue), (b) difference in percentage	44
4.14	Compensation ratio of a dipole-compensated coil with systematic error in PCB width (a) and compensation ratio of a dipole-compensated coil at varying the tolerance on the shaft radius (b).	46
4.15	Radial PCB coil layout for the second transducer prototype.	48
4.16	Tangential PCB coil layout.	49
5.1	Rotating-coil transducer assembly for proof of principle.	52
5.2	Measurement system for measuring the transversal field harmonics along z.	53
5.3	Concept design of a 2D mapper for rotating coil scanner.	54
5.4	Bench set-up for validation measurements.	55
5.5	Second prototype transducer's assembly.	56
5.6	Radial coil transducer assembly.	57
5.7	Tangential coil transducer assembly.	57
5.8	Rendering of the shaft assembly in series configuration (shaft chain).	58
5.9	Maximum total displacement of the single shaft in G11 subjected to the lower eigenfrequency.	59
5.10	Concept design of a 3D mapper for rotating coil scanner.	60
6.1	Layer jumps and connections in a two-layer PCB, with two turns per layer.	66
6.2	Layer jumps and connections, 3D view.	66
6.3	Additional tracks on the compensation coil in order to avoid a concentration of acid during the edging process. Copper points were left on the substrate in order to increase the rigidity of the board.	68
6.4	First iso-perimetric sensor produced.	69
6.5	Iso-perimetric coil sensor magnification on the connection side.	70
6.6	Measured thickness of the sensor no. 1 (red) and sensor no. 2 (blue).	71
6.7	Nominal track position (blue dots) and error (orange bars) for FCB no. 1.	72
6.8	Nominal track position (blue dots) and error (orange bars) for FCB no. 2.	73
6.9	Sensitivity factor main coil from design.	74
6.10	Percentage error on the sensitivity factors due to the positioning errors on the tracks.	74

6.11	Radial coil installed in the first prototype transducer.	77
7.1	Assembly view, radial coil and Hall probe inside the cylindrical shaft. . . .	81
7.2	Assembly of the iso-perimetric coil wrapped around the external diameter of the shaft.	82
7.3	Assembly of the iso-perimetric coil on the cylindrical shaft made in G11. . .	83
7.4	Assembly of the radial coil transducer in G11.	84
8.1	Normal field components (a) and skew field components (b) expressed in units measured in the reference dipole no. 2 at 316 A by the iso-perimetric coil transducer.	94
8.2	Harmonic content in units ($B_2 - B_6$) measured by iso-perimetric coil (a) and radial coil (b).	95
8.3	Standard deviation in units for the harmonic content in the reference dipole center measured by the iso-perimetric, radial, and tangential coil.	96
8.4	Harmonic content (a) and standard deviation (b) in units measured by iso- perimetric, radial, and tangential coil in the dipole center inserting additional distortion.	96
8.5	Harmonic content (a) and standard deviation (b) in units measured by iso- perimetric coil, radial coil, and tangential coil in the dipole edge.	97
8.6	Measurements set-up on dipolar magnet (long tangential coil shaft installed).	98
8.7	Degaussing and pre-cycle applied on the bending corrector dipole.	98
8.8	Integrated harmonics at 11.36 mm. In blue the harmonics measured by the radial coil, in orange by the iso-perimetric coil and in grey measured by the long tangential coil.	100
8.9	Integrated harmonics off center measured by radial (blue) and iso-perimetric (orange) coil.	101
8.10	Differences in units between radial and iso-perimetric integrated harmonics.	102
8.11	Harmonics in unit measured in the magnet center by using the iso-perimetric coil and the Hall probe.	103
8.12	Measured B_1 in the magnet's aperture center (a) and off center (b).	104
8.13	Standard deviation, 3σ , for B_1 . In blue for the radial coil and in orange for the iso-perimetric coil.	105
8.14	B_3 field component along the magnet length. Measured by radial coil in blue, iso-perimetric coil in red and by Hall probe in orange.	106
8.15	Bucking ratio in the aperture center (red) and off center (blue) for iso- perimetric coil (a) and radial coil (b).	106

List of figures

8.16	3σ standard deviation for the B_3 component measured by the main coil of the iso-perimetric transducer.	108
8.17	B_1 field distributions. In blue the measured, in red the simulated and in orange the deconvoluted distribution.	110
8.18	B_3 (a) and B_5 (b) field distributions. In blue the measured, in red the simulated and in orange the deconvoluted distribution.	110
8.19	Computed z-field component using measured data for different radius at $\varphi = 90^\circ$	112
8.20	Computed B_φ component at $r = 19$ mm.	112
8.21	B_1 simulated and convoluted (blue), B_1 measured by the iso-perimetric (red) and standard (orange) coil.	113
8.22	Difference between the convoluted signal and the measured B_1 . Iso-perimetric (blue) and radial coil (red). In the magnet center (a) and off center (b).	114
8.23	Simulated B_1 field profile (a) and B_3 field profile (b).	115
8.24	Coil sensitivity functions: s_1 (a) and s_3 (b).	115
8.25	B_2 field profile measured in the magnet center (a) and off center (b).	116
8.26	B_5 field profile measured in the magnet center (a) and off center (b).	116
8.27	B_1 field component on the CCT magnet.	118
8.28	B_2 field component on the CCT magnet.	119
8.29	B_3 field component on the CCT magnet.	119
8.30	B_5 field component on the CCT magnet.	120
A.1	Technical drawing for the first prototype shaft production.	138
A.2	Technical drawing for the second prototype of the iso-perimetric coil transducer.	139
A.3	Technical drawing of the radial coil transducer.	140
A.4	Technical drawing of the tangential coil transducer.	141

List of tables

4.1	Compensation ratios for different track-positioning errors.	45
4.2	Main dimensions of the radial PCB coil.	48
6.1	Main sensor dimension.	67
6.2	Thickness of the two produced sensors.	71
6.3	Dipole calibration results for the iso-perimetric coil.	75
6.4	Ideal design area (D), curved configuration area estimated from the flat configuration calibration (E), curved calibrated area (C), and the corresponding percentage differences, for the main and compensation coil.	76
6.5	Dipole calibration results for the radial PCB coil installed in the first prototype.	77
6.6	Dipole calibration results for the iso-perimetric sensor (second prototype) in both configuration.	77
6.7	Dipole calibration results of the radial PCB coil no. 2 (second prototype).	78
6.8	Dipole calibration results of the tangential PCBs coils.	78
7.1	Quadrupole calibration for the radial PCB coil of the first prototype.	86
7.2	Results of the quadrupole calibration for the iso-perimetric coil.	87
7.3	Theoretical radii of the iso-perimetric coil from the reverse engineering study.	87
7.4	Difference in term of radius measuring the gradient with the iso-perimetric coil.	88
7.5	Results of the dipole and quadrupole calibration for the second prototype of the iso-perimetric coil transducer.	88
7.6	Results of the dipole and quadrupole calibration for the second prototype of the iso-perimetric coil transducer.	88
7.7	Results of the dipole and quadrupole calibration of the tangential coil transducer.	89
8.1	FDIs calibration factors.	99
8.2	Integrated normal and skew multipoles in units measured by using the tangential coil $L = 1200$ mm @ $R = 35$ mm.	117

List of tables

8.3	Integrated normal and skew multipoles measured by using the iso-perimetric coil.	118
-----	--	-----

References

- [1] Abramowitz, M. and Stegun, I. A. (1965). *Handbook of mathematical functions: with formulas, graphs, and mathematical tables*, volume 55. Courier Corporation.
- [2] Aiba, M., Goddard, B., Oide, K., Papaphilippou, Y., Hernández, Á. S., Shwartz, D., White, S., and Zimmermann, F. (2018). Top-up injection schemes for future circular lepton collider. *Nuclear Instruments and Methods in Physics Research Section A: Accelerators, Spectrometers, Detectors and Associated Equipment*, 880:98–106.
- [3] Arpaia, P., Buzio, M., De Matteis, E., and Russenschuck, S. (2015). A rotating coil transducer for magnetic field mapping. *Journal of Instrumentation*, 10(06):P06006.
- [4] Berz, M., Erdélyi, B., and Makino, K. (2000). Fringe field effects in small rings of large acceptance. *Physical Review Special Topics-Accelerators and Beams*, 3(12):124001.
- [5] Bolshakova, I., Holyaka, R., Erashok, V., and Kumada, M. (2004). High precision mapper for cyclotron magnet. *IEEE transactions on applied superconductivity*, 14(2):1818–1821.
- [6] Brown, K. (1982). *SLAC Report 75 (1970)*. PhD thesis.
- [7] Buzio, M. (2011). Fabrication and calibration of search coils. *arXiv preprint arXiv:1104.0803*.
- [8] Carey, D., Brown, K., and Iselin, C. (1982). Decay turtle. *SLAC-246, UC-28 (I/A)*.
- [9] Caspi, S., Helm, M., Laslett, L., and Brady, V. (1992). An approach to 3d magnetic field calculation using numerical and differential algebra methods. Technical report, Lawrence Berkeley Lab., CA (United States).
- [10] Choi, H., Cha, K., Choi, J., Jeong, S., Jeon, S., Jang, G., Park, J.-o., and Park, S. (2010). Ema system with gradient and uniform saddle coils for 3d locomotion of microrobot. *Sensors and Actuators A: Physical*, 163(1):410–417.
- [11] Davies, W. (1992). The theory of the measurement of magnetic multipole fields with rotating coil magnetometers. *Nuclear Instruments and Methods in Physics Research Section A: Accelerators, Spectrometers, Detectors and Associated Equipment*, 311(3):399–436.
- [12] De Matteis, E. (2016). *Magnetic field mapper based on rotating coils*. PhD thesis, CERN.

References

- [13] Dixiang, C., Mengchun, P., and Feilu, L. (2007). Study on accurate 3d magnetic field measurement system. In *Electronic Measurement and Instruments, 2007. ICEMI'07. 8th International Conference on*, pages 2–680. IEEE.
- [14] Dohi, T. and Murashige, K. (2016). A micro saddle coil with switchable sensitivity for local high-resolution imaging of luminal tissue. *Micromachines*, 7(4):67.
- [15] Erdelyi, B., Lindemann, M., and Berz, M. (2000). Differential algebra based magnetic field computations and accurate fringe field maps. In *APS Meeting Abstracts*.
- [16] Hetzel, J. H., Böker, J., Bechstedt, U., Quilitzsch, S., Engin, I., Ehrlich, C., Bationo, B., Tripathi, P., Soltner, H., Keller, P., et al. (2018). Development of a field mapper for the determination of the multipole components of the curved hesr dipole magnets. *IEEE Transactions on Applied Superconductivity*, 28(3):1–4.
- [17] Hirose, E., Tanaka, K. H., Takahashi, T., Sato, Y., Agari, K., Ieiri, M., Kato, Y., Minakawa, M., Noumi, H., Suzuki, Y., et al. (2004). A new 3-axis magnetic field measurement system based on hall elements. *IEEE transactions on applied superconductivity*, 14(2):1814–1817.
- [18] Hoult, D. I. and Richards, R. (2011). The signal-to-noise ratio of the nuclear magnetic resonance experiment. *Journal of magnetic resonance*, 213(2):329–343.
- [19] Ishikawa, T., Fujimura, H., Hashimoto, R., Ishida, T., Kasagi, J., Kinoshita, T., Kuwasaki, S., Miyahara, F., Miyamoto, A., Mochizuki, K., et al. (2010). The second gev tagged photon beamline at elph. *Nuclear Instruments and Methods in Physics Research Section A: Accelerators, Spectrometers, Detectors and Associated Equipment*, 622(1):1–10.
- [20] Iwashita, Y., Ichikawa, M., Tajima, Y., Fujisawa, H., Kuroda, S., Okugi, T., Tauchi, T., Kumada, M., and Spencer, C. M. (2007). Modification and measurement of the adjustable permanent magnet quadrupole for the final focus in a linear collider. In *Particle Accelerator Conference, 2007. PAC. IEEE*, pages 2719–2721. IEEE.
- [21] Jain, A. K. (2001). Measurements of field quality using harmonic coils. *US Particle Accelerator School on Superconducting Accelerator Magnets*.
- [22] Joseph, D. M. (2003). Harmonics measurements with radially bucked tangential probes. Technical report.
- [23] Kato, S. (2005). An improved description of magnetic fringing field. *Nuclear Instruments and Methods in Physics Research Section A: Accelerators, Spectrometers, Detectors and Associated Equipment*, 540(1):1–13.
- [24] Kirby, G. A., Rysti, J., Gentini, L., Van Nugteren, J., Murtomäki, J., De Rijk, G., Todesco, E., Scibor, K., Mazet, J., and Perez, J. C. (2017). Hi-lumi lhc twin-aperture orbit correctors magnet system optimisation. *IEEE Transactions on Applied Superconductivity*, 27(4):1–5.

- [25] Manikonda, S. and Berz, M. (2006). Multipole expansion solution of the laplace equation using surface data. *Nuclear Instruments and Methods in Physics Research Section A: Accelerators, Spectrometers, Detectors and Associated Equipment*, 558(1):175–183.
- [26] Mitchell, C., O’Shea, F., and Ryne, R. (2018). Accurate modeling of fringe field effects on nonlinear integrable optics in iota. In *9th Int. Particle Accelerator Conf.(IPAC’18), Vancouver, BC, Canada, April 29-May 4, 2018*, pages 3294–3297. JACOW Publishing, Geneva, Switzerland.
- [PT2025] PT2025, N. P. T. Metrolab. URL: <http://www.metrolab.com/index.php>.
- [28] Russenschuck, S. (1999). Roxie: A computer code for the integrated design of accelerator magnets. Technical report.
- [29] Russenschuck, S. (2011). *Field computation for accelerator magnets: analytical and numerical methods for electromagnetic design and optimization*. John Wiley & Sons.
- [30] Russenschuck, S. (2017). Rotating-and translating-coil magnetometers for extracting pseudo-multipoles in accelerator magnets. *COMPEL-The international journal for computation and mathematics in electrical and electronic engineering*, 36(5):1552–1567.
- [31] Sammut, N., Bottura, L., Deferne, G., and Delsolaro, W. V. (2009). Mathematical formulation to predict the harmonics of the superconducting large hadron collider magnets: Iii. precycle ramp rate effects and magnet characterization. *Physical Review Special Topics-Accelerators and Beams*, 12(10):102401.
- [32] Schnizer, P., Fischer, E., Kiesewetter, H. R., Mierau, A., and Schnizer, B. (2011). Field measurements on curved superconducting magnets. *IEEE transactions on applied superconductivity*, 21(3):1799–1803.
- [33] Speer, T., Adam, W., Frühwirth, R., Strandlie, A., Todorov, T., and Winkler, M. (2006). Track reconstruction in the cms tracker. *Nuclear Instruments and Methods in Physics Research Section A: Accelerators, Spectrometers, Detectors and Associated Equipment*, 559(1):143–147.
- [34] Takeda, H., Kubo, T., Kusaka, K., Suzuki, H., Inabe, N., and Nolen, J. A. (2013). Extraction of 3d field maps of magnetic multipoles from 2d surface measurements with applications to the optics calculations of the large-acceptance superconducting fragment separator bigrips. *Nuclear Instruments and Methods in Physics Research Section B: Beam Interactions with Materials and Atoms*, 317:798–809.
- [35] Venturini, M. and Dragt, A. J. (1999). Accurate computation of transfer maps from magnetic field data. *Nuclear Instruments and Methods in Physics Research Section A: Accelerators, Spectrometers, Detectors and Associated Equipment*, 427(1-2):387–392.
- [36] Xu, Q., Nakamoto, T., Iio, M., Ogitsu, T., Sasaki, K., Yamamoto, A., Todesco, E., and Auchmann, B. (2014). Design optimization of the new d1 dipole for hl-lhc upgrade. *IEEE Transactions on Applied Superconductivity*, 24(3):1–4.

References

- [37] Yanagisawa, Y., Kusaka, K., Kubo, T., Haseyama, T., Yano, Y., Suzuki, H., and Mizoi, Y. (2008). Magnetic field-map measurement of a superconducting triplet quadrupole and a dipole magnet for bigrips separator at riken. *IEEE Transactions on Applied Superconductivity*, 18(2):150–154.
- [38] Ying-Shun, Z., Mei, Y., Zhuo, Z., Wan, C., Bao-Gui, Y., Cai-Tu, S., and Wen, K. (2011). Design and end chamfer simulation of pefp beam line curved dipole magnets. *Chinese Physics C*, 35(7):684.
- [39] Zhu, Y., Chen, F., Kang, W., Chen, W., Yang, M., and Wu, X. (2018). Accurate calculation of field quality in conventional straight dipole magnets. *Radiation Detection Technology and Methods*, 2(1):14.

Appendix A

Technical drawings

Technical drawings

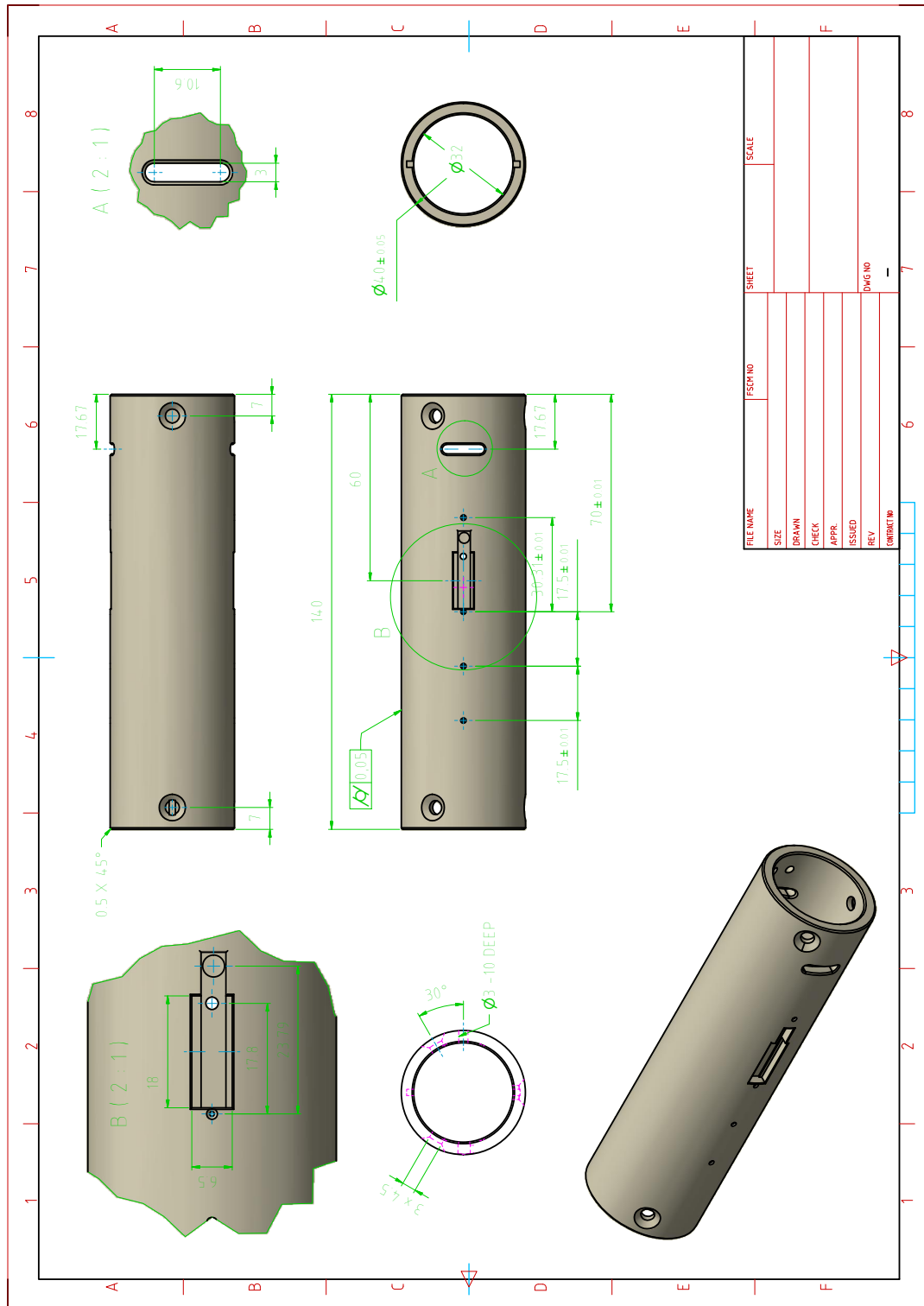


Fig. A.1 Technical drawing for the first prototype shaft production.

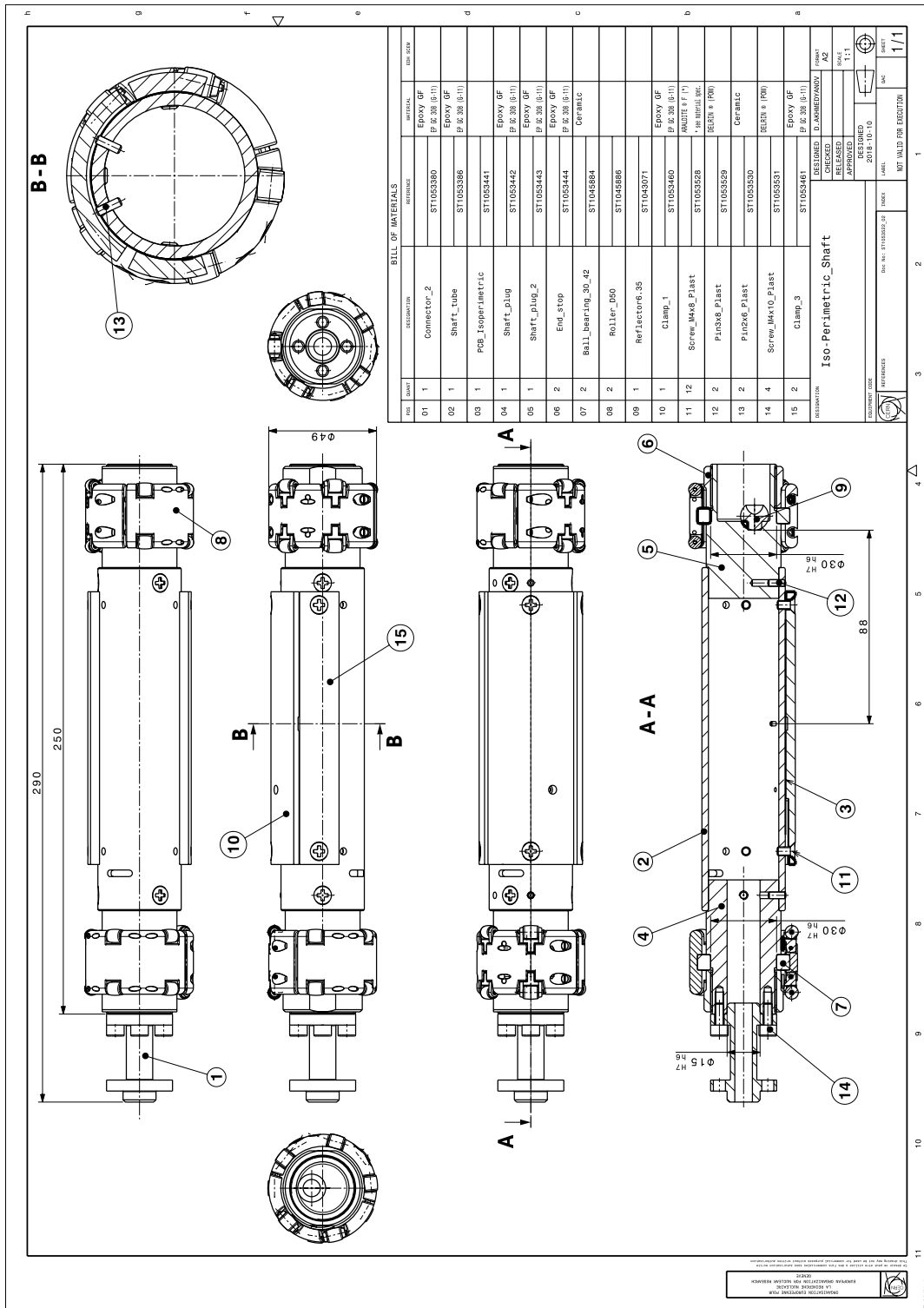


Fig. A.2 Technical drawing for the second prototype of the iso-perimetric coil transducer.

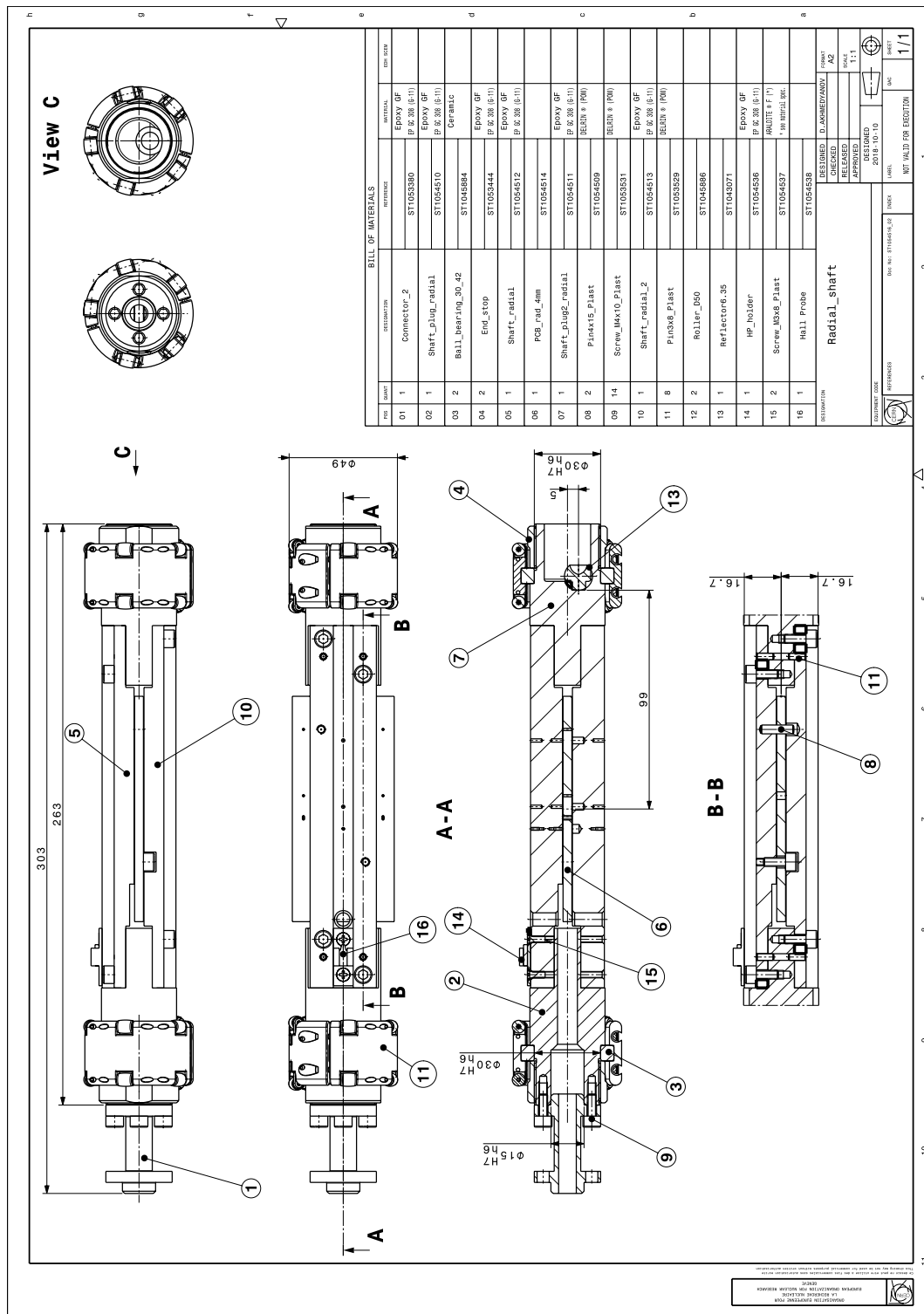


Fig. A.3 Technical drawing of the radial coil transducer.

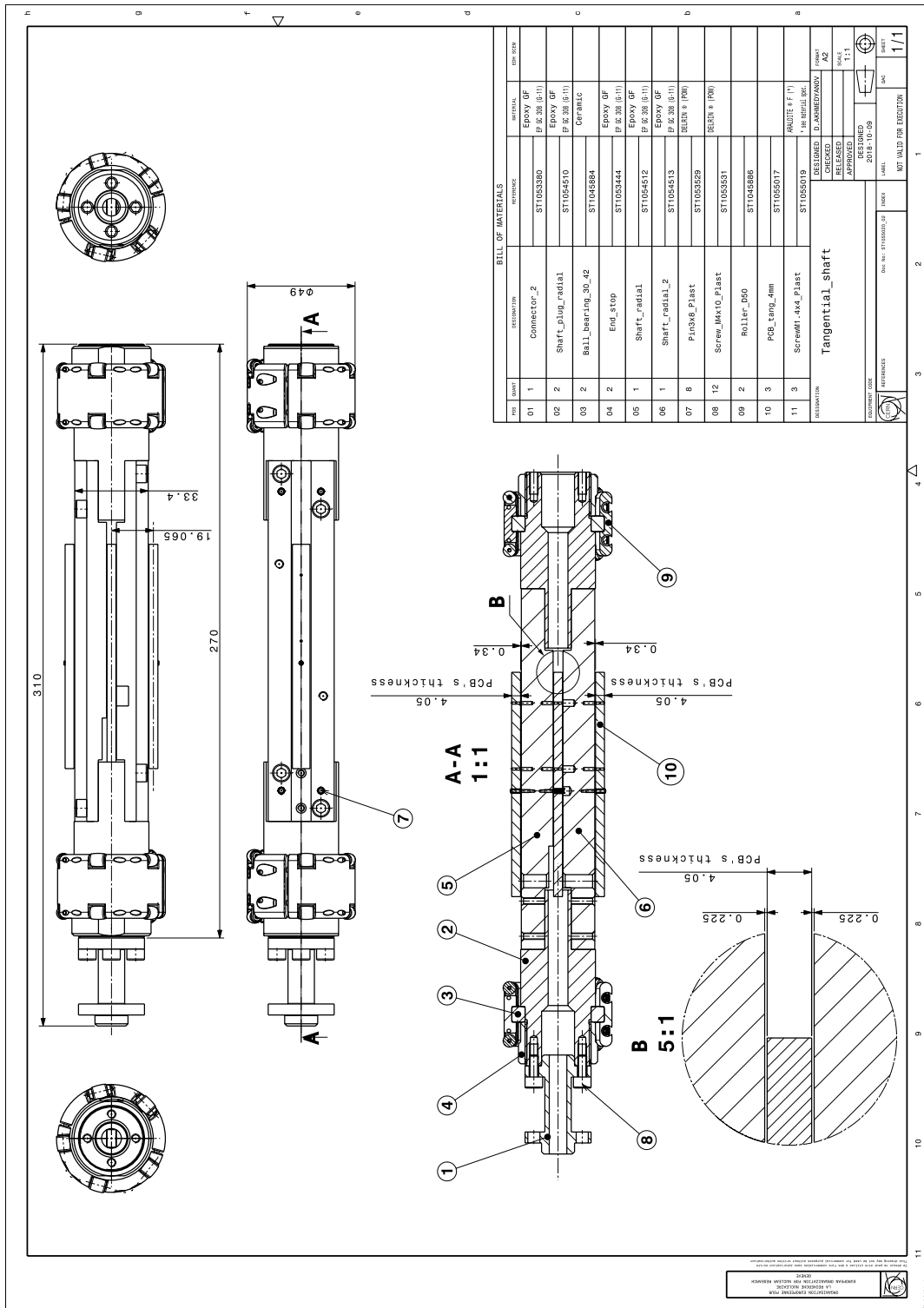


Fig. A.4 Technical drawing of the tangential coil transducer.

